Bond Behavior of Cement-based Repair Materials Under Freeze-thaw and Cyclic Loading Conditions

by

Boyu Wang
Master of Applied Science, University of Victoria, 2018
Bachelor of Engineering, Northwestern Polytechnical University, 2015

A Dissertation Submitted in Partial Fulfillment
of the Requirements for the Degree of

DOCTOR OF PHILOSOPHY

in the Department of Civil Engineering

University of Victoria

We acknowledge and respect the lək̓ʷəŋən peoples on whose traditional territory the university stands and the Songhees, Esquimalt and W̱SÁNEĆ peoples whose historical relationships with the land continue to this day.

Supervisory Committee

Bond Behavior of Cement-based Repair Materials Under Freeze-thaw and Cyclic Loading Conditions

by

Boyu Wang
Master of Applied Science, University of Victoria, 2018
Bachelor of Engineering, Northwestern Polytechnical University, 2015

Supervisory Committee
Dr. Rishi Gupta, Supervisor
Department of Civil Engineering

Dr. Min Sun, Departmental Member
Department of Civil Engineering

Dr. Keivan Ahmadi, Outside Member
Department of Mechanical Engineering

Abstract

According to the 2019 Canadian infrastructure report card, a concerning amount of municipal infrastructure is in poor or very poor condition. The infrastructure in this condition requires immediate action for rehabilitation or replacement. For concrete infrastructure, an effective repair can extend its service life and ensure that the services it provides continue to meet the community expectations. However, unfavorable environmental factors such as repeated/cyclic loads and freezing and thawing cycles adversely affect the bond between substrate concrete and repair materials, which lowers the structural capacity of repaired structures. So far, researchers have found that bond strength of repair can be affected by surface roughness, surface moisture, chemical adhesion or cohesion, curing regime, properties of substrate and repair materials, use of bond agent, and curing regimes. These findings are mostly based on the studies that focused on cold-jointed cylinders or beams, but in real-life repair situations, repairs of beams or slabs are located at either tension or compression side of the structure. Currently, there is no comprehensive study that investigates the bond of concrete repair under a combination of freezing and thawing and repeated/cyclic loading conditions. In addition, it is challenging to provide a rapid and non-destructive evaluation of the bond deterioration of repair materials.

To address these issues systematically, this dissertation breaks the task into four phases. **Phase (I)** focuses on the development of an engineered “crack-free” repair mix that contains polypropylene (PP) fiber. A novel method is used to surface treat the PP fibers with supplementary cementitious materials. The effectiveness of surface-treating fibers for improved bond strength and reduced cracking is investigated. The compressive, tensile, and flexural strength of this engineered repair mix are determined and compared with two commercially available repair materials.

The results from Phase I show that by adding 0.2% (by weight) Metakaolin-treated fibers into concrete mix, the compressive strength improves by up to 15.7% compared to mixes with untreated fibers. This study achieved a strength increase of 13.5% as compared to the

reported 3.3% in other studies that use 25 times the amount of metakaolin used in this study. The experimental results confirm that at 0.2% dosage level, the use of novel surface treating technique is a cost-effective way to improve the strength of repair materials.

Phase (II) focuses on characterizing the bond strength of various repair systems after freezing-thawing (FT) damage using both non-destructive and destructive methods. Two innovative sounding methods, which overcome the subjectivity of the traditional chain drag method, are used to evaluate FT damage non-destructively. In the experimental study, beams with a U-shaped cut are made to simulate conditions experienced by a concrete structure during a typical repair project. Three types of repair materials are used including cementitious repair concrete, cementitious repair mortar, and polymer-modified cementitious mortar. After up to 300 cycles of freeze-thaw exposure, resonant frequency and bond flexural strength of the prismatic specimens are determined. The empirical equations relating Non-destructive test (NDT) measurements and flexural bond strength of the repaired structures after freeze-thaw (FT) exposure are proposed.

The results from Phase II show that the change in dynamic modulus of elasticity (E_{dyn}) determined from NDTs agrees well with the change in other measurements including flexural bond strength (f_r'), interfacial crack width, and mass loss after freeze-thaw exposure. In this study, linear relationships are established between E_{dyn} and f_r' for both cementitious and polymer-modified cementitious repair mortar with a coefficient of determination ranging between 0.87 and 0.95. The proposed empirical models can be used to predict bond flexural strength of repaired structures based on NDT measurement. Also, it was found that the samples repaired with polymer-modified cementitious mortar (Mix P) have superior FT resistance compared to other repaired samples.

Phase (III) focuses on investigating the structural capacity and bond performance of repaired beams after cyclic/repeated loading. To accelerate the test process, a novel modified loading regime consisting of cycle groups of increasing cyclic/repeated stress amplitude is proposed. The models proposed by literature and current codes and standards are used to validate the results. **Phase (IV)** focuses on the development of the damage models for both individual and combined FT and cyclic loading exposure on repaired concrete structures.

The results in phase III show the feasibility of using the Palmgren-Miner rule and Goodman linear model to estimate the fatigue life of repaired structures. This was confirmed within the context of this study. This study established the usefulness of using groups of increasing cyclic stress amplitude to accelerate the fatigue test process. The two-million cycle fatigue endurance limit estimated using cycle groups of Mix S (70.8%) was very similar to what was reported in the literature (71%) using the traditional time-consuming cyclic loading method. This study found that the formulas proposed by CSA 23.3 can effectively predict the moment resistance of both intact (control) and repaired RC beams. The ratio of experimental moment resistance values to its predictions ranges from 0.91 to 1.04. Based on the experimental results of previous three phases, an empirical model that predicted the fatigue service life of FT-damaged concrete structures is proposed.

Future research requires a more comprehensive study on the FT performance of various polymer-modified cementitious mortars of different mix designs in repairing concrete structures. By increasing the number of tested specimens, a better relationship could be established between destructive and NDT methods. Future research is also required to explore the combined effect of FT and cyclic loading on repaired RC structures experimentally.

Table of Contents

Supervisory Committee i

Abstract iii

Table of Contents vi

List of Tables ix

List of Figures x

List of Acronyms xiii

Acknowledgments xiv

Dedication xv

Chapter 1 Introduction 1

- 1.1 Research Background and Motivation 1
- 1.2 Dissertation Objectives 4
- 1.3 Research Outline 4
- 1.4 Research Contributions 6

Chapter 2 Characterization of Enhanced ITZ in Engineered Polypropylene Fibers for Bond Improvement 8

- 2.1 Abstract 8
- 2.2 Introduction 9
- 2.3 Materials and Methods 12
  - 2.3.1 Materials 12
  - 2.3.2 Mixture Proportioning 14
  - 2.3.3. Specimen Preparation 16
  - 2.3.4 Experimental Investigation 17
- 2.4 Results and Discussions 22
  - 2.4.1 Strength in Compression 22
  - 2.4.2 Strength in Direct Tension 25
  - 2.4.3. Flexural Strength 28
  - 2.4.4 Optical Microscopy 31
  - 2.4.5 Scanning Electron Microscopy 32
- 2.5 Conclusions and Recommendations 34

Chapter 3 Analyzing Bond-deterioration During Freeze-thaw Exposure in Cement-based Repairs Using Non-destructive Methods 36
3.1 Abstract 37
3.2 Introduction 37
3.3 Experimental Investigation 41
3.3.1 Materials 41
3.3.2 Specimens 44
3.4 Methods Implemented and Equipment Used 46
3.4.1 Freeze and Thaw (FT) Test 46
3.4.2 Non-destructive Test (NDT) Methods 47
3.4.3 Flexural Strength Test 50
3.4.4 Statistical Analysis 50
3.5 Experimental Results and Discussion 51
3.5.1 Surface Scaling and Mass Loss 51
3.5.2 Dynamic Modulus of Elasticity 53
3.5.3 Bond Quality of the Repairs 60
3.5.4 Relationships Between Destructive and NDT Methods 66
3.6 Conclusions 71
Chapter 4 Performance of Repaired Concrete Under Cyclic Flexural Loading 73
4.1 Abstract 73
4.2 Introduction 74
4.3 Materials and Methods 77
4.3.1 Specimens 79
4.3.2 Flexural Strength & Cyclic Loading Test 82
4.3.3 Non-destructive Test (NDT) Method 86
4.3.4 Bond Test Methods 87
4.4 Results and Discussions 88
4.4.1 Bond Strength 88
4.4.2 Hysteretic Force-displacement Response 90
4.4.3 Loss in E_{dyn} After Cyclic Loading 93
4.4.4 S-N Curve of Repaired Beams 95

        4.4.5 Discussion of Results and Recommendations 97
    4.5 Conclusions 98
Chapter 5 Evaluating Flexural Performance of Repaired Reinforced Concrete Under Static and Repeated Loading Using Non-destructive Methods 101
    5.1 Abstract 101
    5.2 Introduction 102
    5.3 Experimental Program 105
        5.3.1 Materials 105
        5.3.2 Test Specimens 106
        5.3.3 Specimen Preparation Procedure 110
        5.3.4 Test Setup and Instrumentation 111
    5.4 Experimental Results and Discussion 115
        5.4.1 Failure mode and crack pattern 115
        5.4.2 Load-deflection Behavior 119
        5.4.3 NDT Results 122
        5.4.4 Load-strain Relationship 124
    5.5 Theoretical Analysis of Load-bearing Capacity 126
    5.6 Conclusion 128
    5.7 Future work 129
Chapter 6 Modeling the Freeze-thaw and Cyclic Loading-induced damage 131
    6.1 Introduction 131
    6.2 Damage Model of FT Exposure 132
    6.3 Damage Model of Cyclic Loading 137
    6.4 Service Life Model of FT-damaged Concrete Under Cyclic Load 138
    6.5 Model Validation 139
Chapter 7 Conclusions and Future Work 144
    7.1 Concluding Remarks and Key Findings 144
    7.2 Recommendations for Future Work 146
Bibliography 148
Appendix A 177

List of Tables

Table 1 Different mix designs and the number of samples cast 16

Table 2 Mix proportions of Mix S (kg/m^3) 43

Table 3 Fresh and hardened properties of concrete and repair mixes.............................. 43

Table 4 Characteristics of interfacial cracks 66

Table 5 Relationships between destructive and NDT methods proposed by codes and standards 67

Table 6 Relationships between the results from destructive and NDT methods 69

Table 7 Mix design details of the parent material (kg/m^3) (data from [195]) 78

Table 8 Details of fresh and hardened properties of substrate and repair materials (data from [195]).. 79

Table 9 Loading force groups for different samples.. 85

Table 10 Fatigue lives and permanent deformation before failure of different mixes 92

Table 11 S-N curves reported in literature.. 96

Table 12 Mix proportions of the parent material receiving the repair (kg/m^3) 106

Table 13 Fresh and hardened properties of parent and repair mixes 106

Table 14 Description of test specimens 107

Table 15 Summary of damage levels at which vertical and horizontal bond failure started 118

Table 16 Summary of crack length after repeated loading 119

Table 17 Yield strength, bending stiffness, and NDT results 121

Table 18 Yield strength of the RC beams post repeated loading.................................... 122

Table 19 Experimental and theoretical moment resistance and first cracking moment . 128

Table 20 Summary of FT damage models in the literature 134

Table 21 Damage models for repair and control mixes 136

Table 22 S-N curves of repaired and intact beams in this study (from Chapter 3)......... 138

Table 23 Summary of service life prediction curves 139

Table 24 Input parameters to the model (data adopted from [275]) 141

List of Figures

Figure 1 Scanning electron microscope (SEM) image showing polypropylene fiber, ITZ, and mortar 10
Figure 2 Schematic diagram of the proposed method of improvement of ITZ 12
Figure 3 Chart showing the process of fiber preparation 14
Figure 4 Different mix designs with Mix M as the base material 15
Figure 5 Specimens cast for testing: (a) mortar cube; (b) beam; (c) dog-bone/ coupon .. 17
Figure 6 Details of the direct tensile strength test in progress 18
Figure 7 Details of the flexure strength test in progress 20
Figure 8 Arrangement of the displacement measuring set up for beams 21
Figure 9 Compressive Strength of different mixes at 14 days and 28 days 23
Figure 10 Tensile Strength of different mixes with 14 days and 28 days strength 25
Figure 11 Load vs displacement curves comparing MFU, MFM, MFS 27
Figure 12 Brittle failure of unreinforced mortar mix, MC (left) and ductile cup and cone fracture for reinforced mortar, MFS (right) 28
Figure 13 Schematic diagram of three-point bending test on mortar beam specimen 29
Figure 14 Flexural Strength of different mixes with 14-days and 28-days (red) strength 30
Figure 15 Images showing various fibers used in the study: (a) untreated polypropylene (10x magnification) fiber; (b) polypropylene fiber coated with metakaolin (45x magnification); (c) silica fume coated polypropylene fiber (45x magnification) 31
Figure 16 SEM images of metakaolin coated fibers (clockwise from top left): (a) image showing coating at 200x magnification; (b) spectrum showing the constituent peaks; (c) elemental map of oxygen and silicon; (d) elemental map of silicon only; (e) elemental map showing oxygen only 34
Figure 17 Gradation curves of aggregates of Mix S (a) Fine aggregate (b) Coarse aggregate 43
Figure 18 Procedure for preparing repaired specimens (a) #6 CSP chip (b) 3D printed chip (c) concrete mold (d) specimens with a simulated cavity (e) repaired specimens 45
Figure 19 Schematic of flexural testing on repaired prisms (all dimensions are in mm) . 46

Figure 20 NDT test configurations (a) Hammer percussion test configuration (b) Modified chain drag test configuration (c) Accelerometer configuration for hammer impact test on specimens 48
Figure 21 Surface scaling of different mixes due to FT 52
Figure 22 Mass loss of all mixes vs. FT cycles 53
Figure 23 Example of frequency analysis (a) Vibration signal of hammer percussion method (b) Corresponding frequency spectrum (c) Vibration signal of modified chain drag method(d) corresponding frequency spectrum 55
Figure 24 (a) Transverse vibration using RFT method (b) Transverse vibration using hammer percussion method (c) Transverse vibration using modified chain-drag method56
Figure 25 Probability P that the null hypothesis is true for each pair of different NDTs. 59
Figure 26 Flexural strength of repaired beams at 0 and 300 FT cycles 61
Figure 27 Bond failure modes of repaired beams before and after FT exposure 62
Figure 28 E_{dyn} measured from the transverse vibration of cylinders 63
Figure 29 Horizontal interfacial cracks in Mix F after the flexural test 64
Figure 30 Image analysis using ImageJ software 64
Figure 31 Comparison of experimental results based on RFT method and building code predictions 70
Figure 32 Gradation curves of aggregates used in this study (Redrawn from [195]) 78
Figure 33 Prismatic specimens under four-point loading (all dimensions are in mm) 80
Figure 34 Mold preparations (a) 3D printed block and #6 CSP chip (b) 3D printed blocks in molds 81
Figure 35 Bond test sketches (a) Splitting tensile test (b) Slant shear test (all dimensions in mm) 82
Figure 36 Test setup for cyclic loading 83
Figure 37 Cyclic Loading Regime 85
Figure 38 Resonant frequency test setup 87
Figure 39 Bond stresses at failure for different repair materials (a) slant shear bond (b) Splitting tensile bond 89
Figure 40 Failure patterns of bond test (a) Splitting tensile test (b) Slant shear test 90

Figure 41 Hysteretic force-displacement curves of representative specimens for (a) Mix S (b) Mix F (c) Mix M (d) Mix P 91

Figure 42 Failure mode under cyclic loading of (a) Mix M repaired specimen (b) Mix F repaired specimen (c) Mix P repaired specimen (d) Control Mix S specimen................. 93

Figure 43 Example of extracting resonant frequency (a) Vibration signal generated by hammer impact (b) Frequency spectrum obtained via FFT... 94

Figure 44 Change in dynamic elastic modulus as a result of flexural cyclic loading....... 95

Figure 45 S-N curve for different samples 96

Figure 46 Steel reinforcement details for (a) RC beam with 1/3-span repair (b) RC beam with full-length repair (c) Intact beam without repair (all dimensions in mm) 109

Figure 47 Sample preparation procedures (a) Inserting foam for full-length repaired beams (b) Inserting foam for 1/3-span repaired beams (c) demolded samples (d) Samples with foams removed (e) Full-length repaired beams (f) 1/3-span repaired beams 111

Figure 48 Loading-unloading regime of the repeated loading....................................... 113

Figure 49 Experimental setup of (a) Hammer percussion test (b) Modified chain drag test (c) Ultrasonic pulse velocity test... 114

Figure 50 Crack pattern of beams with (a) 1/3-span repaired with Mix M (b) 1/3-span repaired with Mix F (c) full-length repair with Mix F (d) full-length repair with Mix M (e) no repair 118

Figure 51 Load-center point deflection curve of beams with (a) 1/3 span repair (b) full-length repair (c) no repair 120

Figure 52 Resonant frequency for beams at different damage degree D_i (i = 1,…,6) measured using (a) hammer percussion method (b) modified chain-drag method......... 123

Figure 53 UPV of beams at different damage degree D_i (i = 1,…,6)........................... 124

Figure 54 Load vs. strain of steel reinforcements... 125

Figure 55 Predicted and experimental number of cycles to failure after (a) 50 FT cycles (b) 100 FT cycles (c) 150 FT cycles... 142

List of Acronyms

Abbreviation or symbol	Definition
PP	Polypropylene
FT	Freezing and Thawing
RFT	Resonant Frequency Test
E_{dyn}	Dynamic Modulus of Elasticity
E_c	Static Modulus of Elasticity
f_r'	Modulus of Rupture
UPV	Ultrasonic Pulse Velocity
IE	Impact Echo
RC	Reinforced Concrete
ITZ	Interfacial Transition Zone
SCM	Supplementary Cementitious Materials
EDS	Energy-Dispersive X-Ray Spectroscopy (EDS)
FRC	Fiber Reinforced Concrete
ESTF	Engineered Surface Treated Fibers
LVDT	Linear Variable Differential Transformer
ANOVA	Analysis of Variance
p	Probability
P	Peak load
f_c'	Compressive strength
HWRA	High-range Water Reducing Agent
CSP	Concrete Surface Profile
FFT	Fast Fourier Transform
COV	Coefficient of Variant
UHPC	Ultra-high-performance Concrete
RMSE	Root means square error

Acknowledgments

First and foremost, I would like to sincerely thank my mentor and supervisor, Dr. Rishi Gupta, for his guidance throughout my PhD journey. I am grateful for his continuous support, encouragement, and mentorship during my studies. I also want to express my gratitude to my supervisory committee members: Dr. Min Sun and Dr. Keivan Ahmadi for their support for my research study.

I would like to thank our industry partners, Terry Bergen and Peter Dias from Read Jones Christoffersen Ltd for their involvement and guidance.

I am very thankful for the financial support provided by the Natural Sciences and Engineering Research Council of Canada (NSERC).

I would like to acknowledge our Civil Engineering Technical staff, Dr. Armando Tura, Bastien Lanusse, Geoff Burton, Arielle Garrett, and co-op students, Liam Sprangers, and colleagues, Maryam Monazami, and Perla Rodulfo for their assistance in the experimental work.

Dedication

To my beloved parents and wife.

Chapter 1 Introduction

1.1 Research Background and Motivation

Concrete is the most widely used material in the world because of its strength, durability, and versatility. Concrete structures can deteriorate with time and the severity of the deteriorations is largely dependent on the environmental conditions. In Canada, 16.4% of the roads, bridges, and tunnels are in poor or very poor condition [1]. The structures in poor conditions represent that the asset is approaching the end of its service life, which requires immediate action such as rehabilitation or replacement. Concrete repair materials have been used for nearly 100 years to extend the service life of concrete structures such as pavements, buildings, and bridge decks [2]. However, due to the proprietary nature of repair materials, manufacturers are understandably reluctant to provide complete details of their materials and thus there is limited information offered to the users. Among different types of repair materials, cement-based and polymer-based materials are most widely used [3]. Compared to the conventional concrete mix, repair materials possess superior durability performance, high early strength, and fast setting characteristics, which reduce the downtime of structures and expedite return to service. After the repair work, the bond strength, which features the effectiveness of the repair, is often measured. In practice, bond strength is determined by coring and pull-off tests [2]. Failure stress can be obtained by dividing the maximum force applied by the cross-sectional area and this can be used to quantify the bonding strength. It is important to know the factors that lead to concrete cracking and destructive failure. It is widely believed that debonding can result from the external mechanical loading, and from the effect of different length changes between new and old concrete as a consequence of freezing and thawing (FT), temperature variations, etc [4].

Cyclic loading is one of the conditions that results in fatigue failure. The failure of the materials is caused by the repeated application of the load even though this load is not large enough to cause failure at the beginning. The fundamental mechanism behind this is that concrete fails based on the concepts of stress concentration and fracture mechanics theories [5]. When the concrete is subjected to cyclic loading, there will be residual strain accumulating after each cycle, which indicates the internal progressive permanent structural change in the concrete. In the case of repaired structures, it is important to ensure sufficient fatigue life for the bond between the parent concrete and repair materials. Currently, two repair techniques are commonly used. One of them is using externally bonded layers to strengthen damaged beams. The externally bonded layers are mostly carbon fiber reinforced polymer sheets [6]–[8] and are attached to the damaged surface through epoxy adhesive. Most studies [6]–[8] have shown that externally bonded layers can effectively improve the load-bearing capacity of the beams under both static and cyclic/repeated loading conditions. The other repair technique involves removing the deteriorated concrete and rebars and replacing them with repair materials. Many researchers focused on the static loading performance of the reinforced concrete (RC) beams repaired with strain hardening cement-based materials [9], polymer-modified mortar, alkaline-activated mortar [10], and ultra-high-performance fiber-reinforced concrete [11]. However, scarce work reported the effect of cyclic or repeated loading on beams repaired with commercially available products that are widely used such as polymer-modified cementitious mortar and cementitious concrete.

Apart from the effect of cyclic loading, FT of concrete can also degrade the bond strength. Generally, FT cycles refer to the condition where concrete is exposed to extremely low temperatures and is then thawed at room temperature. Concrete can undergo large, irreversible losses in strength especially for water-saturated samples after FT exposure [12]. One of the major causes of this damage is due to the 9% expansion of water phase to ice phase [13]. When the pores are critically saturated, the freezing of the water exsert pressure on the pore walls or on the surrounding unfrozen water in the smaller pores. If the pressure exceeds the strength of the materials, microcracking is formed. This is the well-known hydraulic pressure theory. Another major cause is the water vapour pressure difference between large and small size pores. Larger pores, which have higher water vapour pressure tend to force water into smaller pores, which have lower water vapour pressure, through osmosis. The osmosis pressure can exceed the tensile strength of the pore walls and cause microcracking. This is called the osmotic theory. Both hydraulic and osmotic theories are found to have some limitations in explaining some test observations [14], [15]. The recent advancements in poromechanics were found to have a better explanation of FT in concrete. Many researchers [16]–[18] have reported the FT performance of repair materials but the bond performance of various types of repairs has not been well understood.

So far, shear and tension tests are the most commonly used methods for evaluating bond strength of the repair work because cracks will mostly formulate and propagate under a combined influence of tension and shear forces.

Many destructive test methods have been developed to quantify the bond strength between concrete substrate and repair materials. They are designed to evaluate the tension and shear bond strength at the concrete-repair interface. Tension bond methods include pull-off test, dog-bone tension test, splitting cylinder test, and patch flexural test. The torsion bond methods include torsion shear test and slant shear test. However, the destructive methods are time-consuming, and conducting such tests induces further damage to the structures [19], [20]. As a result, non-destructive test (NDT) methods are introduced to address these issues. Several NDT methods have been studied and are reported to have the potential to detect bond strength of the repair. They include three-dimensional (3D) laser scanning method [21], [22], impulse response [23], impact-echo (IE) [24], and ultrasonic pulse velocity (UPV) test [25].

In summary, the author could not find any reported studies on the applicability of NDT methods on FT-damaged structures. Also, there are limited studies that assessed the effect of a combination of FT cycles and cyclic loading test on bond characteristics of polymer-modified cement-based materials and other types of repairs. There have been exhaustive studies [26]–[31] that used Palmgren-Miner’s rule and its modified forms on concrete materials, but insufficient studies reported the applicability of Palmgren-Miner’s rule on predicting the fatigue life of repaired structures. Additionally, there is a knowledge gap about understanding the static and cyclic loading performance of beams where deteriorated materials are replaced by repair patches though most previous studies focused on RC beams with externally bonded layers.

Note that a more comprehensive literature review about the repair materials, FT test, cyclic/repeated loading test, and NDT methods are integrated within each chapter that follows.

1.2 Dissertation Objectives

The main objective of this dissertation is to study the freeze-thaw and cyclic loading performance of repair materials as well as the bond strength. The sub-objectives are succinctly summarized below.

- Determine the effectiveness of using engineered fibers treated with supplementary cementitious materials (SCM) to improve the fiber-matrix bond in repair materials.
- Determine the freeze-thaw and cyclic loading performance of repaired structures using various types of commercially available repair mixes.
- Determine the performance of several sounding-based NDT methods in detecting and quantifying bond deterioration and materials damage due to FT and cyclic loading
- Determine the effect of rebar presence, repair length, and repair material type on repeated loading performance of repair reinforced concrete structures.
- Develop a service life model that predicts the cyclic fatigue life of repaired structures after freeze-thaw damage.

1.3 Research Outline

Chapter 1 provides the context of this study and introduces the motivation that led to this research.

Chapter 2 is presented in the form of a peer-reviewed published journal paper. In this chapter, the use of novel surface-treated fibers to improve the crack resistance and mechanical performance of the commercially available repairs used is presented. Under the scanning electron microscope, the interfacial transition zone was observed in one of the commercial products that contain polypropylene fibers. By surface treating the fibers, the high tensile strength of the fibers can be exploited, which potentially led to improvements in material strength.

Chapter 3 is presented in the form of a peer-reviewed published journal paper. In this chapter, the use of both destructive and non-destructive approaches to evaluate the bond performance of the repairs and the load-bearing capacity of the repaired structures after FT exposure are presented. The vibration-based NDT methods are used including resonant frequency, hammer percussion, and modified chain drag methods. These methods have a faster testing speed and potentially better detectability compared to IE and impulse response methods that were used in the literature.

Chapter 4 is presented in the form of a peer-reviewed published journal paper. In this chapter, the cyclic loading performance of concrete repaired with various repair systems is studied. To accelerate the test process, a modified loading regime consisting of cycle groups of increasing cyclic stress amplitude is used. The applicability of Palmgren-Miner's rule on predicting the fatigue life of repaired structures is studied. A method based on fatigue stress to flexural strength ratios is also proposed to derive the S-N curve. The estimated fatigue life in this study is compared with the results in previous literature to determine its liability.

Chapter 5 is presented in the form of a journal manuscript that is currently under review. In this chapter, the mechanical properties of the repaired RC beams under static and repeated loading performance are studied. In chapter 4, it was found that interfacial cracks between concrete and repairs could lead to as high as 50% loss in flexural strength for unreinforced concrete. As a result, chapter 5 focuses on studying the effect of rebar presence on the repaired concrete under both static and repeated loading conditions.

Chapter 6 presents the proposed damage models for concrete that experience both Freeze-thaw and cyclic loading.

Chapter 7 summarizes the main results and presents the concluding remarks and future scope of work that can be undertaken.

1.4 Research Contributions

There is a need to repair the deteriorated structures and extend their service life. However, there is a lack of information about the performance of concrete repair especially under harsh environments such as FT and cyclic/repeated loading conditions. There is also a strong need for using testing techniques to give rapid, reliable, and non-destructive evaluations of post-repair structures. Also, due to the porous interfacial transition zone, fiber-reinforced repair materials cannot fully exploit the benefit of the high tensile strength of the fibers. In this dissertation, the author has attempted to address these issues. The contributions made by the author include:

1. This research was instrumental in confirming that all three NDT methods are applicable for detecting FT damages of repaired structures based on the test results of 12 specimens. The NDT methods include resonant frequency, hammer percussion, and modified chain drag tests. Other test observations such as surface scaling, mass loss, and interfacial crack width validate this finding.
2. This research proposed a model that relates dynamic elastic modulus to flexural bond strength of repaired samples after FT exposure. The proposed linear regression models have a coefficient of determination value ranging between 0.87 and 0.95. The model could be useful to estimate the residual bond flexural strength of repaired samples.
3. This research confirmed the feasibility of using the Palmgren-Miner rule and Goodman linear model [32] to estimate the fatigue life of repaired concrete structures within the context of this study.
4. This research found that model formulas proposed by code CSA 23.3 can effectively predict the moment resistance of both intact (control) and repaired RC beams based on the test

results of 12 repaired RC beams. The ratio of experimental moment resistance values to its predictions ranges from 0.91 to 1.04.

5. This research confirmed that the use of the novel surface treating technique is a cost-effective way to improve the strength of repair materials. Based on the test results of 36 samples, adding 0.2% (by weight) of Metakaolin-treated fibers into concrete mix achieved a strength increase of 13.5% as compared to the reported 3.3% in other studies that use 25 times the amount of metakaolin used in this study.
6. This research proposed an empirical model that predicted the fatigue service life of FT-damaged concrete structures. The model was validated using the data provided by previous literature.

Chapter 2 Characterization of Enhanced ITZ in Engineered Polypropylene Fibers for Bond Improvement

Rishabh Bajaj[a], Boyu Wang[b], Rishi Gupta[c]*

Article Link: https://www.mdpi.com/2504-477X/4/2/53

[a]Undergraduate Student, Department of Civil Engineering, National Institute of Technology Rourkela, Odisha, 769008, INDIA; rishabhbajajnitr@gmail.com
[b]Graduate Student, Department of Civil Engineering, University of Victoria, 3800 Finnerty Road, Victoria, B.C., V8W 2Y2, CANADA; boyuwang@uvic.ca
[c] Associate Professor, Department of Civil Engineering, University of Victoria, 3800 Finnerty Road, Victoria, B.C., V8W 2Y2, CANADA; guptar@uvic.ca
*****Correspondence: email guptar@uvic.ca; Tel +1 (250)721-7033

Note: This chapter is adapted from the paper that has been published in Journal of Composites Science (MDPI), with permission where appropriate. This chapter highlights the development of a novel method to surface treat the polypropylene fibers with supplementary cementitious materials. The surface-treated fibers are added to repair mixes and the compression, tensile, flexural, and microscopical characteristics are evaluated.

2.1 Abstract

The interfacial transition zone (ITZ) is well known to be a zone of high porosity, lesser strength, and is the weak zone in the fiber-reinforced matrix. This study aims to evaluate the improvement in the bonding between engineered polypropylene fibers and the surrounding mortar matrix. The improvement was implemented by modifying the ITZ which develops between the fibers and the cementitious matrix. Two commercially available repair materials have been used in this study, Mix M and Mix P. Mix M served as the base material for the prepared fibers; while Mix P is a fiber-reinforced repair mortar and provides a comparison. A total of six types of mixes have been investigated. The improved bonding is tested by coating the polypropylene fibers with

supplementary cementitious materials (SCM) using an innovative patented concept. In this study, silica fume and metakaolin are used as the SCM because of their fine size and pozzolanic capacity. The study involves multiple items of investigation including mechanical tests: compressive strength, direct tensile strength, and three-point bending tests. Energy-Dispersive X-Ray Spectroscopy (EDS) of the different mixes helped in evaluating and analyzing the ITZ between the fiber and matrix.

2.2 Introduction

Fiber Reinforced Concrete (FRC) is increasingly being used in the field due to its high toughness and energy absorption capacity. Early application of FRC can be traced back to the 1960s when randomly dispersing steel fiber was employed in analogy with traditional steel reinforcing bars [33]. Cement composites exhibited the general brittle characteristics under failure loads allowing the steel fibers to bridge the propagating cracks. Steel FRC possesses a long history of successful application [34], whereas recent research shows a growing interest in synthetic fibers. Synthetic fibers, such as polypropylene (PP), polyethylene, polyvinyl chloride, and many others [35] have some substantial advantages over metallic ones. The typical characteristics of synthetic fibers include chemical stability in aggressive environments, exemption from oxidation, lightness, easy stocking and handling, and electromagnetic transparency. As a result, they have been used in a variety of places including road pavements [36], storm sewers, water drains [37], etc.

A major issue associated with using synthetic fibers is caused by their lack of hydrophilicity. They react very little with the concrete matrix and consequently, loading is hardly transferred from the matrix to the fibers [33]. Another major challenge is the interfacial transition zone (ITZ). Owing to the “wall effect”, the matrix around macroscopic particles such as aggregates and fibers does not pack as efficiently as in the rest of the matrix [38], [39], as shown in Fig. 1. Poor bonding between the aggregates/fibers and the cement matrix generates a weak ITZ [40] that hinders full exploitation of the fiber strength [38]. To address these shortcomings, many approaches have been investigated. These are described below.

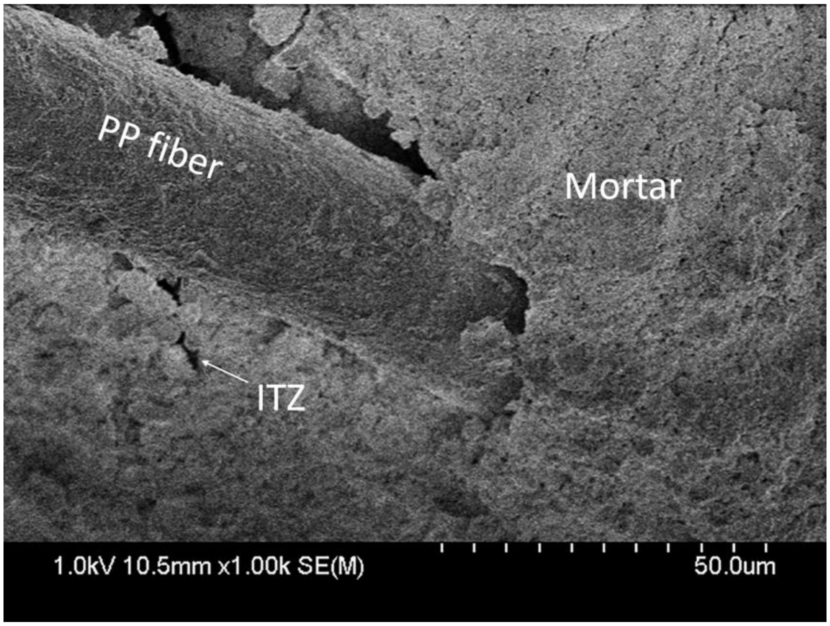

Figure 1 Scanning electron microscope (SEM) image showing polypropylene fiber, ITZ, and mortar

Surface treatment has been considered one of the viable techniques to improve ITZ. Some treatment methods previously reported in the literature include cold plasma treatment [41], mechanical micro-pitting treatment [42], flame treatment [43], wet chemical treatment [44], and nano-silica treatment [33]. Mechanical micro-pitting treatment involves creating indentations on the fiber surface by pressing the fibers between two hardened steel surfaces. This method may cause cross-section loss and is hard to be applied on short fibers with small diameters. Wet chemical treatment method requires the use of the acid or any other solution etching the fiber surface such that the frictional properties of fibers are improved. This method can result in degradation of the mechanical performance of the fiber if excessive etching takes place. Also, disposal of etching chemicals causes environmental issues. The problem with flame or heat treatment is the increase in brittleness of the fiber materials after the treatment. Compared to these methods, cold plasma treatment is relatively eco-friendly, fast, and does not exhibit excessive brittleness. Cold plasma treatment can reduce the surface energy of the polymer surface and thus convert the hydrophobic structure of PP surfaces to hydrophilic, which increases chemical bonding with the cementitious matrix [45]. However, the cold plasma method can still produce detrimental waste unless some specific gas composition is selected [41]. Some researchers [46] have previously used nano-silica as the coating to improve the bonding between the matrix and the PP fibers. The silica nanoparticles are deposited on PP-fibers via the rapid acid-catalyzed sol-gel technique [47]. The use of nanoparticles is associated with an increase in the cost which could potentially limit the application of this technique.

Based on the literature review, there exists a need to surface treat the fibers with a material that is relatively eco-friendly and low-cost. SCMs such as silica fume and metakaolin are sustainable and environmental-friendly materials because there are limited CO_2 emissions during metakaolin production [48], [49] and silica fume is a waste material from the industrial process [50]. Over the years, SCMs have been used to deal with the porous ITZ [51], [52]. Pozzolans, including metakaolin, silica fume, and fly ash are chemically reactive with calcium hydroxide in the concrete to form cementitious materials, which results in a denser ITZ. Physically, using micro fillers such as metakaolin and silica fume can also fill up the voids between the reinforcement and matrix. As an example, most researchers have concluded that silica fume is indeed instrumental in enhancing concrete properties by improving the ITZ [53]–[55]. However, SCM, which is normally used to replace cement content by up to 20% volume [56]–[58], does not clearly target the ITZ. Previous studies have proved that the densification of ITZ is possible by coating coarse aggregates with silica fume [53]. Other researchers [59] have shown that the addition of pozzolans such as silica fume and fly ash does help in the densification of the ITZ which in turn improves the mechanical strength and durability [59], [60].

In this study, a novel method to surface treat the PP fibers with SCMs is proposed. The core of this method is based on an invention by Gupta titled “Surface Treatment for Concrete Reinforcement” [61]. The focus of this research was to investigate the effectiveness of surface treating fibers for improved bond strength. The proposed method utilizes pozzolans including silica fume and metakaolin. The presence of such pozzolans is usually expected to improve the strength of the matrix. Instead of adding to the entire mix, these pozzolans targeted the regions requiring their use in ITZs surrounding the fibers [61]. To achieve this, a new method is developed which disperses the PP fibers, applies adhesive to every fiber, and adheres pozzolans to the fibers, as shown in Fig.

2. In addition, one commercially available repair material is used as the base material where the surface-treated fibers are added. Repair materials are now widely used to extend the lifetime of structures and thus have a greater need for maintaining safety and serviceability [62]. Most of these repair materials comprise a component of cement, polymer, and at times, both [62]–[64]. The base material in this study is classified as cementitious repair mortar.

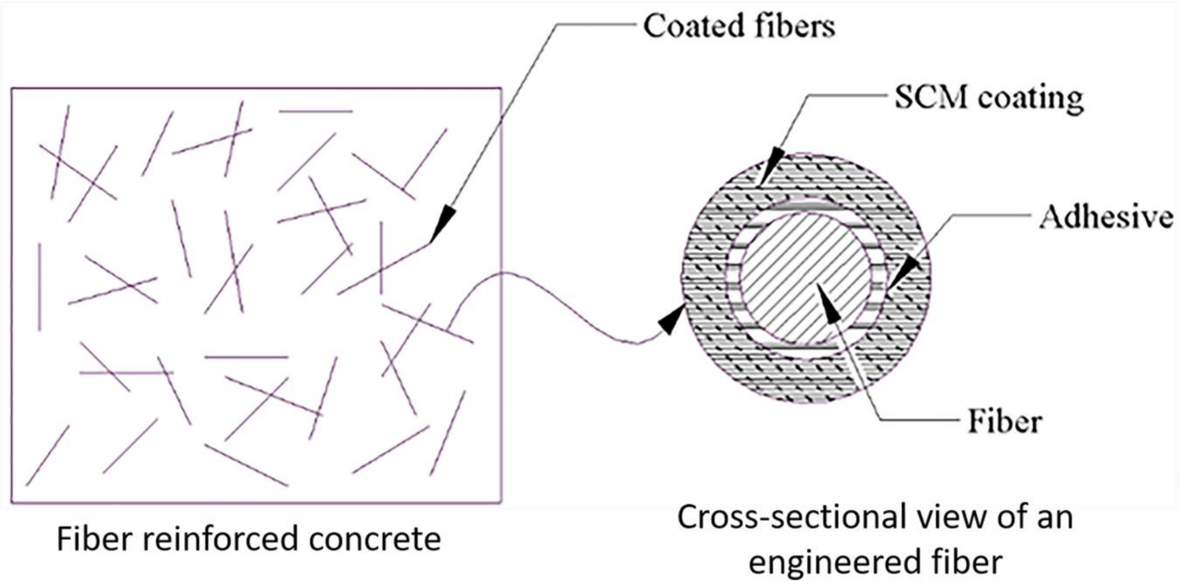

Figure 2 Schematic diagram of the proposed method of improvement of ITZ

2.3 Materials and Methods

2.3.1 Materials

In this study, polypropylene fibers are treated with two SCMs to produce engineered surface treated fibers (ESTF) of two kinds: silica fume coated and metakaolin coated. Since silica fume has a finer grain size and greater surface area to volume ratio, it is expected to improve the ITZ more than metakaolin, however, in this study both materials are used to provide an insight into their relative performance. The cementitious mortars used are repair mortars namely Mix M and Mix P, as described later in this section. Fibers are added to Mix M and a comparison is made to unmodified Mix M and Mix P.

2.3.1.1. Polypropylene Fibers

In this study, a 100% virgin polypropylene microfiber was used. The mechanical properties of the fiber as stated in the material safety data sheet [65] are listed in Table A1 available in Appendix A.

2.3.1.2. Repair Mortars

In this study, commercially available Mix M and Mix P were used which can be described as cementitious mortar, and polymer-modified cementitious mortar respectively. For the preparation of samples, only potable water was added to make the mix workable. As per the data sheets, Mix M is especially suited for cold weather installations and the repair of freezer floors. It is available in 25 kgs polyethylene-lined bags. Mix P is suited for vertical and overhead concrete repairs, including precast/prestressed, tilt-up, post-tensioned, and cast-in-place concrete. It is available in bags of 22.7 kgs. The chemical composition of Mix M and Mix P are listed in Table A2 and Table A3 respectively available in the supplementary materials section. The information was provided by the supplier.

2.3.1.3 Fiber Coating Materials

(a) Metakaolin: Highly reactive class N pozzolan metakaolin was used in this study. Chemically, it contained 100% calcined kaolin. The properties of the metakaolin used, as extracted from the safety data sheet [66] are listed in Table A4 available in the supplementary materials section. (b) Silica Fume: Properties of the silica fume used in this study are listed in Table A5 available in the supplementary materials section as per the information from the material safety data sheet [67].

2.3.1.4 Adhesive

A multi-purpose adhesive with a compatible spray applicator is used. The adhesive is used to assist the coating of fibers with metakaolin and silica fume. A spray adhesive ensures even distribution and minimizes irregularities. Chemical composition extracted from the material safety data sheet [68] is listed in Table A6 available in Appendix A.

2.3.2 Mixture Proportioning

A total of six mixes were prepared including control samples, with and without fibers. The fibers were coated with the help of an enclosed chamber. The chamber had a small opening fitted with a nozzle. Through the opening, the air was blown using an air compressor to keep fibers agitated. Using the air compressor, the fibers were first dispersed inside the chamber, next the multipurpose adhesive was sprayed, and the air compressor was used to coat the fibers as evenly as possible. Coated fibers were obtained by dusting the SCM over the fibers coated with adhesive. The air compressor was used again to distribute the SCM throughout the fibers inside the chamber. The basic procedure is illustrated in Fig. 3. To separate the fibers from the adhered mesh-like formations, the fibers were chopped to obtain filaments. Some samples were taken from the chopped fibers, and the length was measured to be ranging from 3 to 6 mm maintaining an aspect ratio between 100 and 200. It should be noted that this lab-based procedure does not guarantee the complete coating of all fibers. The unevenness of the coating might prove to be better in terms of binding with the mortar, however, this aspect requires further detailed investigation. The SCM content was estimated to be about 19.96% by weight as the percentage of the original untreated fibers taken for the coating procedure.

Figure 3 Chart showing the process of fiber preparation

The water content was used as prescribed in the technical sheet of the repair mixes used. In the case where Mix M was used as the base material, the water content was slightly increased from the prescribed to take into account the water adsorption and the expected reduction in workability due to the PP fibers and was kept consistent throughout the mixes, including control mixes without fibers. On analysis of Mix P, the amount of fiber was found to be about 0.2% by weight. To simulate the same reinforcement in mix M, the total amount of the treated fiber was also kept at 0.2% for all specimens.

The various mixes were prepared to capture the effect of incrementally adding layers of coating on the virgin fiber. The first mix contains uncoated virgin PP fibers, the next mix contained the adhesive layer only, the succeeding mixes contained metakaolin coated over the adhesive and the final mix contained silica fume coated over the adhesive, as shown in Fig. 4. As discussed in earlier sections, the commercially available repair mix P already contains fibers. Hence, no additional mixes were prepared with mix P. Instead, the mix was used as is to serve as a comparative mix to this study. The mix designs and the number of samples cast for each mix are listed in Table 1.

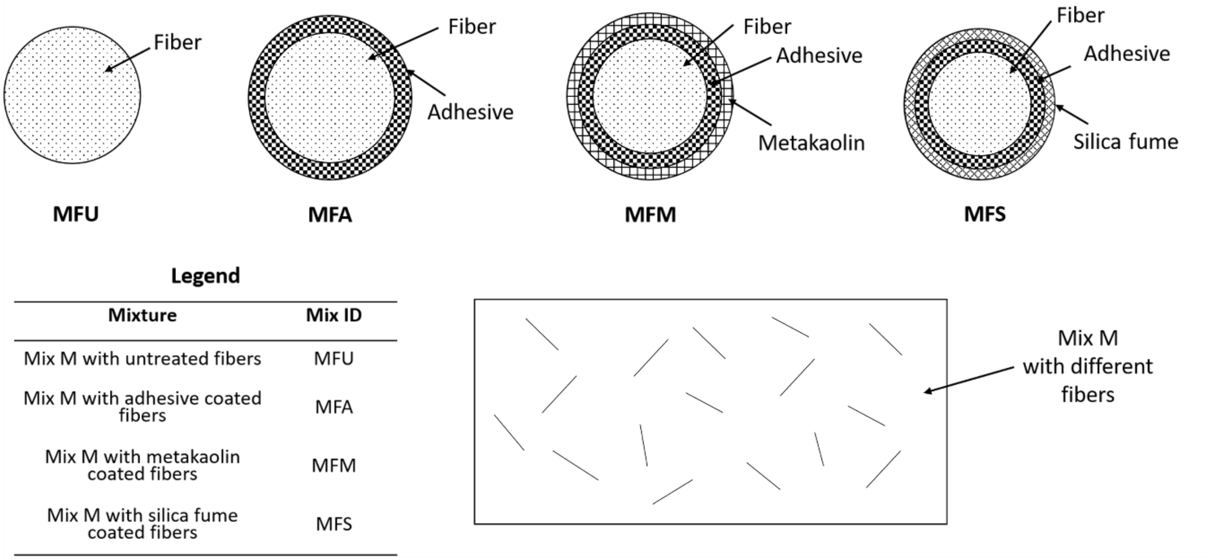

Legend

Mixture	Mix ID
Mix M with untreated fibers	MFU
Mix M with adhesive coated fibers	MFA
Mix M with metakaolin coated fibers	MFM
Mix M with silica fume coated fibers	MFS

Figure 4 Different mix designs with Mix M as the base material

Table 1 Different mix designs and the number of samples cast

SI No	Mixture	Mix ID	Water Content (% by weight of the repair mortar)	Working Time (mins)	Fiber Type	Number of Samples Cast		
						Cubes	Coupons	Beams
1	Mix P (commercial mix with fibers)	PF	17	5	Commercial fiber-reinforced repair mortar	6	6	6
2	Mix M (Control mix M without fibers)	MC	10	45	No fiber added	6	6	6
3	Mix M with untreated fibers	MFU	10	45	Micro polypropylene fibers with no coating	6	6	6
4	Mix M with adhesive coated fibers	MFA	10	45	Micro polypropylene fibers coated with spray adhesive only	6	6	6
5	Mix M with metakaolin coated fibers	MFM	10	45	Micro polypropylene fibers coated with spray adhesive and dusted with metakaolin	6	6	6
6	Mix M with silica fume coated fibers	MFS	10	45	Micro polypropylene fibers coated with spray adhesive and dusted with silica fume	6	6	8

2.3.3. Specimen Preparation

Mortar cubes were cast in accordance with ASTM C109 [69]. Each of the cubes (50 mm in size) was cast in two layers with a hand tamping technique used for consolidation. A total of 6 cubes for each mix were cast for determination of compressive strength. Briquette samples prepared were cast and tested to determine the tensile strength of the mixes. The briquettes had a cross-section of 645.16 mm^2 at the neck. Briquette moulds used were in accordance with ASTM C307 [70]. Both the width of the neck and thickness was 25.4 mm as per the provisions of ASTM. A total of 6 specimens for each mix were prepared to test the tensile strength. In addition to the ASTM standard tests on mortars as stated above, beams of size (30 x 30 x 100 mm) were cast. The cast specimens of each type are shown in Fig. 5. These specimens were prepared to determine the modulus of rupture in flexure for each of the mixes. A total of 6 beams were prepared for each mixture type. Immediately after moulding, specimens were sealed in plastic sheets to minimize the evaporation of moisture from the fresh mix. Specimens were stored at 23 ± 2 °C for 24 hours before demoulding. Demoulded samples were stored in water at a temperature of 23 ± 2 °C. All the mixes were immersed in separate water containers to avoid cross-contamination from the effect of leaching of free lime or constituents of SCMs.

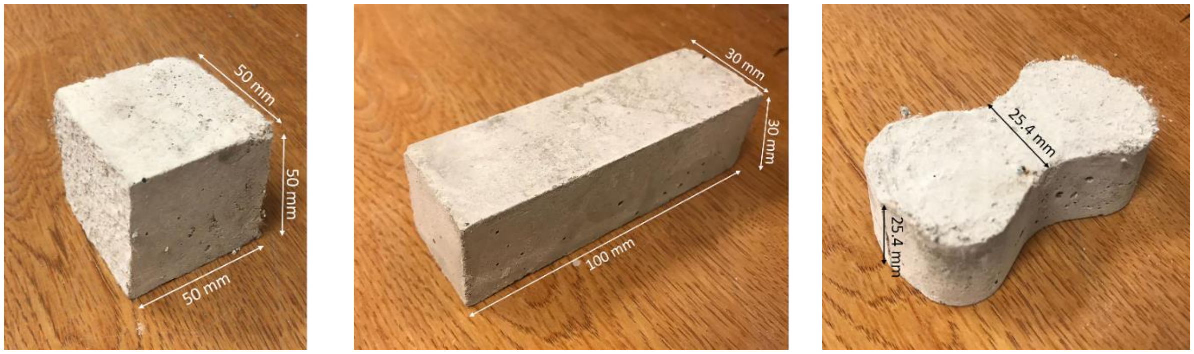

(a) (b) (c)

Figure 5 Specimens cast for testing: (a) mortar cube; (b) beam; (c) dog-bone/ coupon

2.3.4 Experimental Investigation

2.3.4.1 Compressive Strength Test

Sides of the mortar cubes were evened out using sandpaper to ensure even load distribution from the testing machine to the specimen face. Specimens were taken out of the curing water and allowed to attain saturated surface dry condition before carrying out tests. Tests were performed in accordance with ASTM C109 [69]. FORNEY compression testing machine F-650 was used in conjunction with FORNEY Test Pilot digital indicator for this test. The machine has a load capacity of 2891 kN. The load was applied at a rate of 0.6 MPa/s. Tests were conducted at 14 days and 28 days and three specimens were tested at each age.

2.3.4.2 Tensile Strength Test

Specimens were taken out of the curing tank and allowed to attain saturated surface dry condition before carrying out tests. A total of at least 6 specimens per mix were moulded. The test was performed in accordance with ASTM C307 [70]. The test was conducted using PASCO ®

Materials Testing Machine ME-8236 used in conjunction with briquette grips. The machine had a load cell capacity of 7100 N. In its original capacity, ME-8236 operates using a manual crankshaft, to regulate the process of controlling speed and load rate. The machine was modified by adding an electric motor BMUD60-A2 from Oriental Motors ®. The motor comprises a brushless DC Motor Driver compatible with a single-phase 100-120 VAC power supply. Using the motor, the speed was set to 50 rpm which translated to a displacement rate of 0.5 mm/min on the briquette sample. This automation in the machine resulted in a much more constant loading rate. The machine was coupled with the PASCO ® 550 Universal Interface to connect to the PASCO Capstone Software. The deflection of the coupon samples was determined by the software from the number of rotations made by the threads of the machine. The deflection and loads were recorded at a sampling frequency of 25 Hz. The direct tensile test was carried out at 14 and 28 days of curing and six specimens were tested for each age.

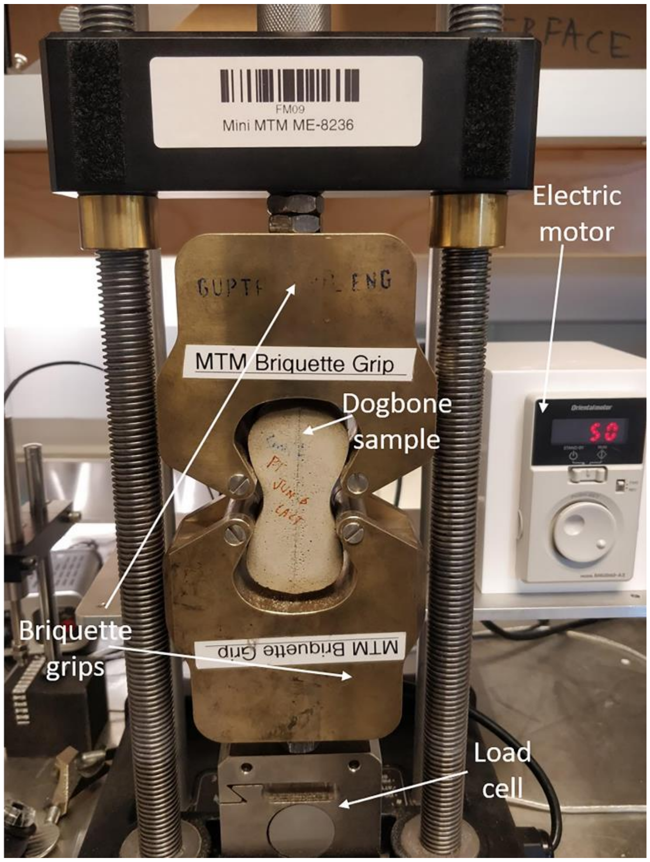

Figure 6 Details of the direct tensile strength test in progress

2.3.4.3 Three-point Flexural Test

Mortar beams were cast to determine the flexural strength (modulus of rupture). To carry out flexural strength tests using the three-point bending setup, the same PASCO ® ME-8236 equipment as described above was used. The briquette grips were replaced by the ME-8237 materials bending accessory provided by PASCO ®. The accessory included a plunger and adjustable support anvils. For this study, the span length between the anvils was kept constant at 88 mm, as shown in Fig. 7. Displacement measurements were recorded with the help of the LD620-25 linear variable differential transformer (LVDT) produced by OMEGA®. The LVDT had a range of 25 mm with an excitation voltage of 10 to 30 Vdc @ 25 mA and had an output of ± 5 Vdc with a bandwidth of 500 Hz. The LVDT was kept in contact at the mid-span of the beam with the help of stainless-steel L-brackets attached to the beams using fast-setting epoxy resin, as demonstrated in Fig. 8. A total of at least 6 specimens per mix were cast. Three-point bending tests were conducted at a strain rate of 0.5 mm/min at 14 and 28 days of curing. Three specimens were tested at each testing age.

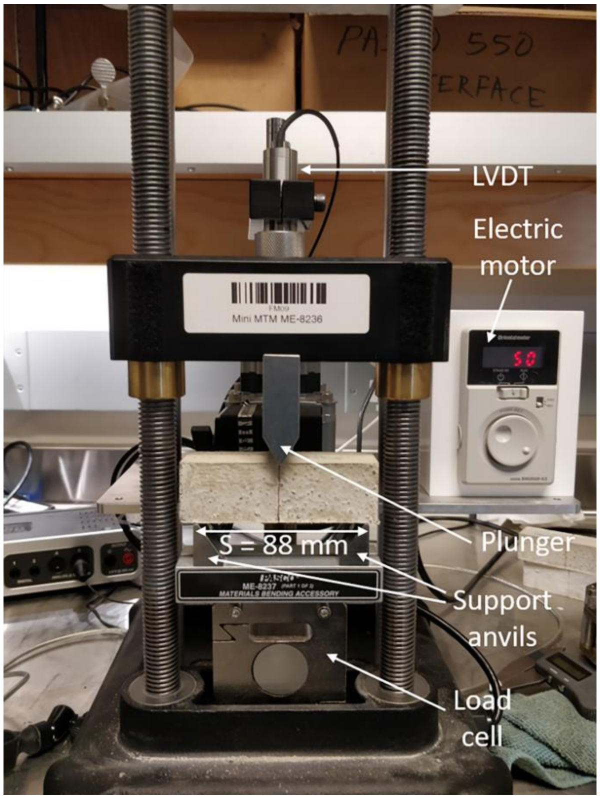

Figure 7 Details of the flexure strength test in progress

Figure 8 Arrangement of the displacement measuring set up for beams

2.3.4.4 Microscopic Analysis

The ESTF were observed under an optical microscope for a preliminary examination of the metakaolin and silica fume coating. A trinocular stereo zoom microscope produced by Amscope © was used for the examination. Specifications of the microscope include 7x-45x continuous zoom magnification power with a super widefield optical system and a 10 cm working distance. It is also enabled with a trinocular port that added photo capturing capability once interfaced with a computer system.

Specimens containing coated fiber samples (MFM and MFS) were analyzed under an SEM to check for the coating of fibers and bonding with the matrix. Elemental mapping on each fiber sample was done on fiber surfaces to evaluate the effectiveness of the coating method used. Additionally, the interface between fiber and matrix was analyzed to evaluate the effect on the interfacial transition zone. Scanning electron microscopy was done using Hitachi S-4800 FESEM, as shown in Figure A1 in the supplementary materials section. The equipment has a 1 nm resolution at 15 kV, 1.4 nm at 1 kV, and a magnification range from 30x to 800,000x. Slices from dog-bone samples were cut using a wet tile saw. The cut slices were kept in an airtight chamber attached to a vacuum pump immediately after the cutting process was over. This was done for a period of at least 3 days to retard the formation of any hydration product after the samples are cut. The samples were placed in a vacuum chamber immediately after being cut and surface dried for a period of at least 3 days. The sliced samples were further cleaned and vacuumed for a period of 24 hours using the Hitachi ZoneSEM desktop sample cleaner which uses UV light to remove contaminants. The Cressington 208C was used to carbon coat the samples to allow SEM imaging on the non-conductive samples. Carbon coating of samples is also recommended by the manufacturer in cases where EDX is to be done as carbon does not absorb and fluoresce as much as other coatings.

2.4 Results and Discussions

2.4.1 Strength in Compression

Fig. 9 shows the results of the compressive tests done for all the mixes measured at both 14-day and 28-day strength. Average compressive strength is presented for various mixes with error bars.

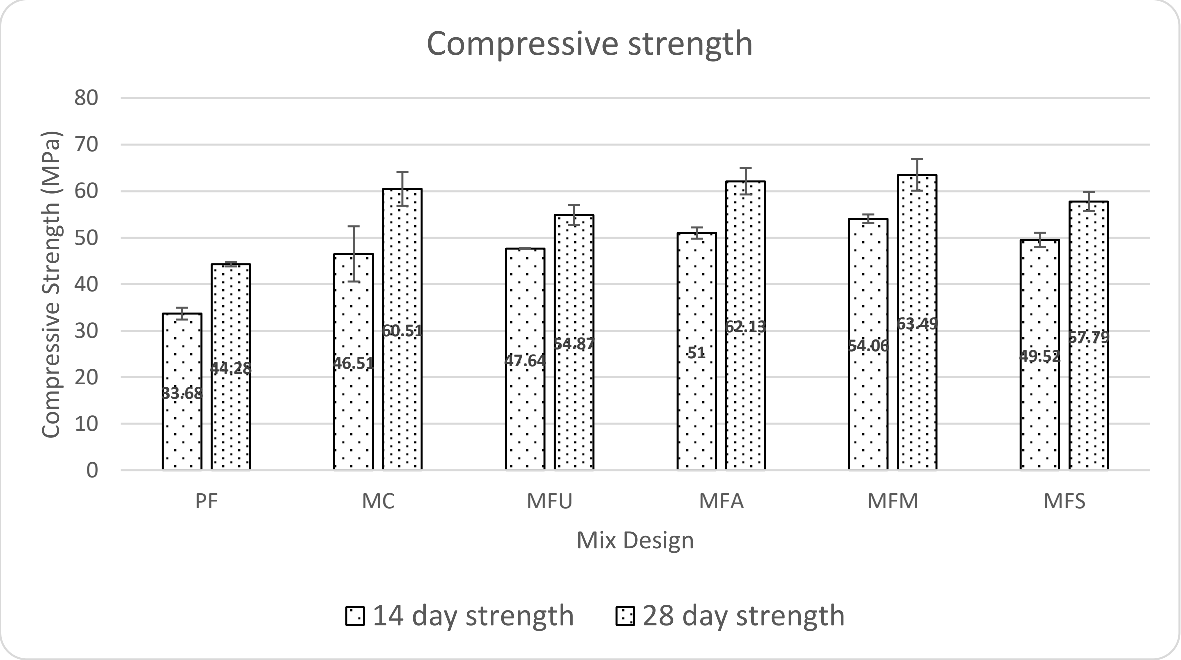

Figure 9 Compressive Strength of different mixes at 14 days and 28 days

Compared to the base material (MC), the mix reinforced with untreated polypropylene fiber (MFU) showed an increase in compressive strength by 2.43% at 14-day age and a drop by 9.32% at 28-day age. Whereas, when studying the effect of treatment of fibers, metakaolin treated fibers (MFM) showed an increase of 7.05% (14-day strength) and 15.71% (28-day strength) on average whereas silica fume coated fibers (MFS) showed an improvement of 3.94% (14-day strength) and 5.32% (28-day strength) from untreated polypropylene fibers (MFU) in the same matrix. On comparing the base material (MC) with the commercially available fiber-reinforced repair material, the increase in strength was 38.09% at 14 days and 36.65% at 28 days. The main reason is that the base material (MC) had lower water content in the mix than that of the fiber reinforced repair materials (PF).

The compressive strength due to metakaolin increased by 13.47% when comparing 14-day MFU and MFM samples. Other studies [71] showed an increase of 3.27% on replacing 5% cement with metakaolin. In this study, by using a much less amount of metakaolin, the strength has increased by 13.47% as compared to 3.27%.

On comparing the 28 days cured samples, the cube strength of MFM increased by 15.71% compared with MFU. A study [58] showed an increase of as high as 16.8% in compressive strength on the addition of 20% metakaolin which is 100 times the amount of metakaolin used in the present study. The same study [58] also showed an increase of 7.9% in compressive strength in the case of silica fume whereas the present study used 0.01 times the amount of silica fume to report a cube strength improvement of 5.32%. This further suggests that the position of the SCM in addition to the SCM properties itself plays an important role in the mechanical strength of the material. To better understand the effect of the treated fibers, two types of samples could be prepared in the future. This includes one with metakaolin without any adhesive to coat the fibers and the other one with SF. Researchers [72] have shown interest in metakaolin due to its micro filler and pozzolanic properties. Pozzolanic materials such as metakaolin and silica fume react with portlandite to produce additional cementitious gel [73]. In the case of metakaolin, the pozzolanic property is the ability to react with calcium hydroxide in the presence of water to form hydrated silicate gel products that possess cementitious properties [74], [75]. Although the calculations for the improvements were made using the averages, it is essential to keep in mind that these averages were found out within the limits of experimental error which have been quantified in terms of the standard deviation as included in Fig. 9.

Further, a statistical validation test was performed on the compressive strength results using the one-way Analysis of Variance (ANOVA) technique in MATLAB. The one-way ANOVA was conducted to compare the effect of coating on the compressive strength. A script was written in MATLAB software where the built-in 'anova1' function was used to perform the ANOVA. In the MATLAB script, the compressive strength data from using different mixes is saved in different columns/groups, and the ANOVA was performed by comparing all these groups at a time. The ANOVA technique has been previously used by researchers [76] to understand the statistical variation in tests done on mortars. The statistical confidence of the effect of the coating on the compressive strength was analyzed. The probability p that the null hypothesis is true was determined for the three critical mixes namely, MFU, MFM, and MFS. A threshold of $p = 0.05$ was considered and the comparisons were made. The p values greater than the threshold value of

0.05 were considered statistically insignificant. The analysis of variance showed that the effect of the coating on the compressive strength was significant, $p = 0.0033$ for 14-day strength. Similarly, the 28-day strength was also validated using the one-way ANOVA test, $p = 0.0295$. Since the probability p was less than the threshold in both cases, this shows that the comparisons are significant, and the coating does improve the compressive strength.

2.4.2 Strength in Direct Tension

Fig. 10 shows the results of the direct tension tests conducted on mortar briquettes (also referred to as dog-bones or coupons) for all the mixes measured at both 14-day and 28-day strength. Average tensile strength is presented for various mixes with error bars.

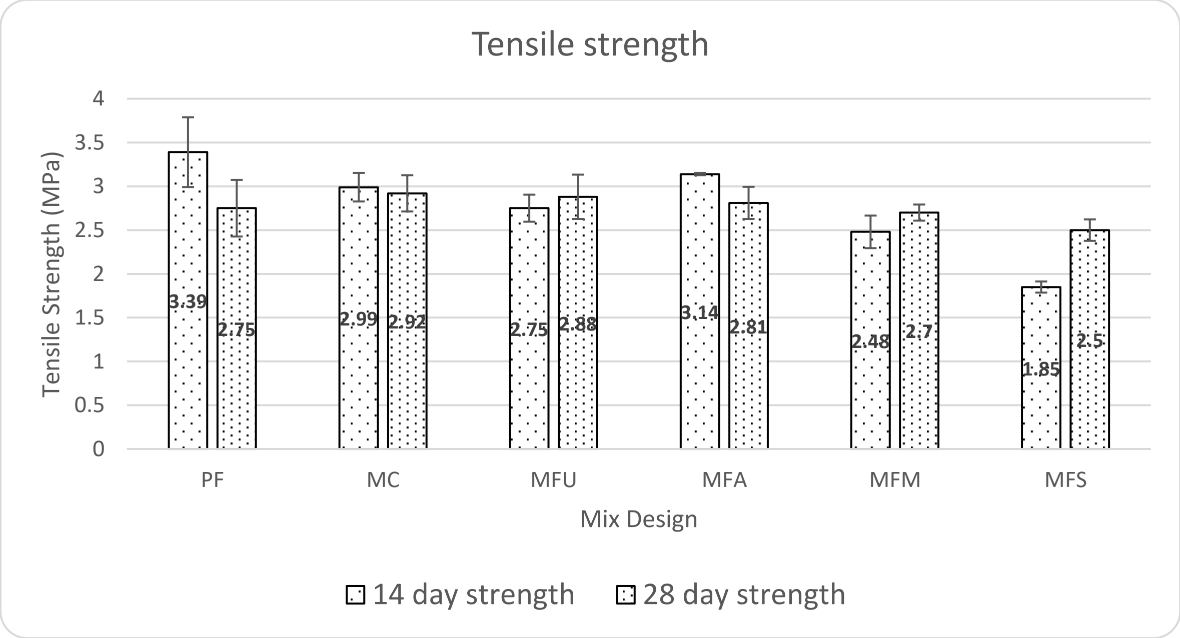

Figure 10 Tensile Strength of different mixes with 14 days and 28 days strength

The tensile strength was calculated by dividing the peak (maximum) load by the cross-sectional area of the failure plane which was calculated by determining the actual length and depth at the section of failure of the dog-bone specimens using digital calipers. The following is Eq. 1 used to calculate the tensile strength of the mixes:

$$Tensile\ Strength\ (MPa) = \frac{P}{b \times d} \tag{1}$$

where P is peak load in N, b is the width and d is the depth respectively of the coupon at failure surface in mm.

As shown in Fig. 10, given the relatively high standard deviations for mixes with fibers added, the tensile strength does not show any significant difference in the addition of fibers to the base material (MC). It should be noted that, for mix PF and MFA, the average tensile strength at 28 days of curing is lower than that at 14 days of curing. It is most likely due to the large standard deviation of test results of the repair materials because the errors bars for Mix PF and MFA are mostly overlapped as shown in Fig. 10. The high standard deviation could stem from fast setting characteristics of the repair materials. In the case of a large number of samples being cast at the same time, fast setting may cause inconsistency within the mix. PF mixture showed the highest strengths both at 14 days and 28 days of curing. The relatively high strength in mix PF possibly indicates the presence of an inclusive and compatible mix of fibers by the supplier, which leads to high tensile strength. For further investigation, fibers in mix P (PF mix) were studied under SEM and an optical microscope. This revealed a better dispersion of fibers in the commercial mix P. The diameter of fibers in the commercial mix P (PF) was found to be about 15 microns whereas the fibers used and modified in this study for other mixes were 30 microns in diameter.

The area under the tensile curve (Fig. 11) represents the toughness of the specimens. The toughness of MFU, MFM, and MFS samples was 766.06 N-mm, 790.03 N-mm, and 829.40 N-mm respectively. Samples reinforced with treated fiber (including MFM and MFS) showed ductile behaviour and the toughness value is slightly higher than that of untreated fibers coupons (MFU). Albeit, this is not a significant improvement and may not be representative of all the samples. This aspect needs to be studied in future studies.

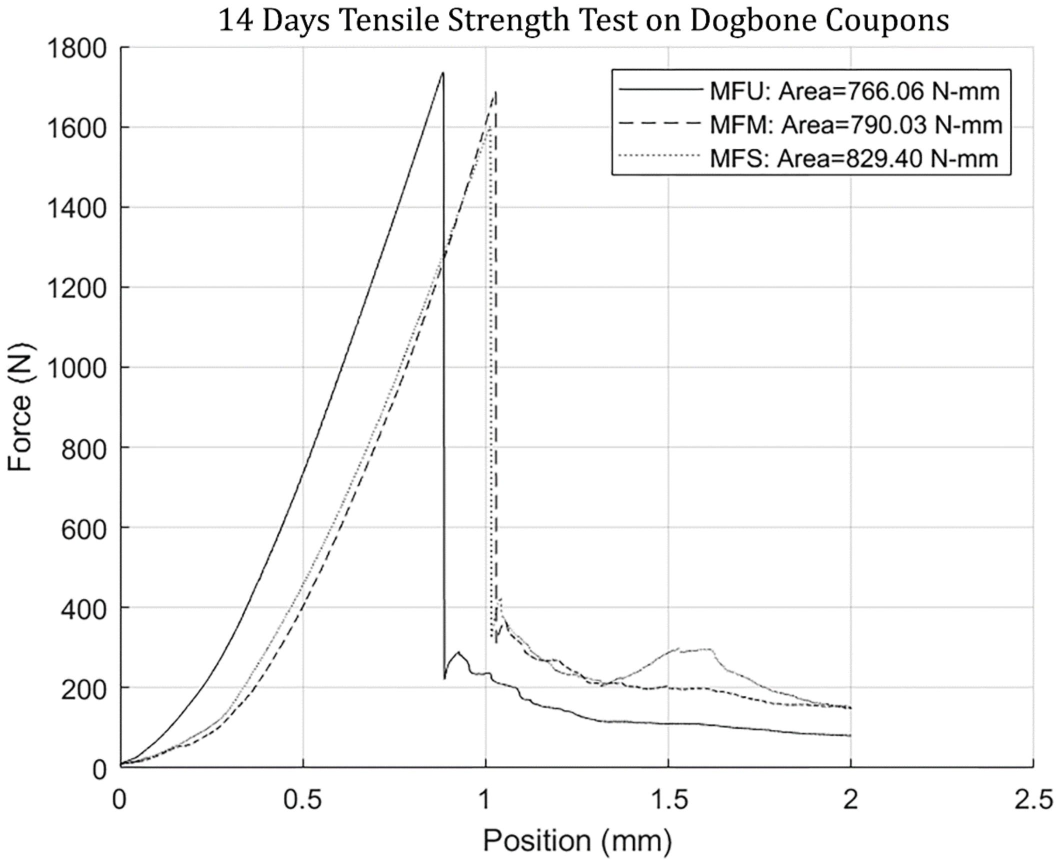

Figure 11 Load vs displacement curves comparing MFU, MFM, MFS

Fiber-reinforced samples using laboratory-prepared fibers (MFU, MFA, MFM, MFS) exhibited ductile fracture after reaching peak loads. The fracture planes resembled ductile fracture patterns observed in metals subjected to uniaxial tension. This is a possible indicator of the shift to plastic failure on adding fibers as opposed to a brittle failure in unreinforced samples (MC), as shown in Fig. 12. These results were typical for most of the fiber-reinforced samples tested under direct tension.

Figure 12 Brittle failure of unreinforced mortar mix, MC (left) and ductile cup and cone fracture for reinforced mortar, MFS (right)

2.4.3. Flexural Strength

A schematic diagram of the three-point bending test is shown in Fig. 13. The modulus of rupture was calculated using Eq. 2:

$$\sigma_{max} = \frac{3PS}{2bd^2} \tag{2}$$

where σ_{max} = modulus of rupture in MPa, P = peak load applied on the beam in N, S = support span in mm (kept constant at 88 mm for the study), b = width of the beam (30 mm), and d = depth of the beam (30 mm).

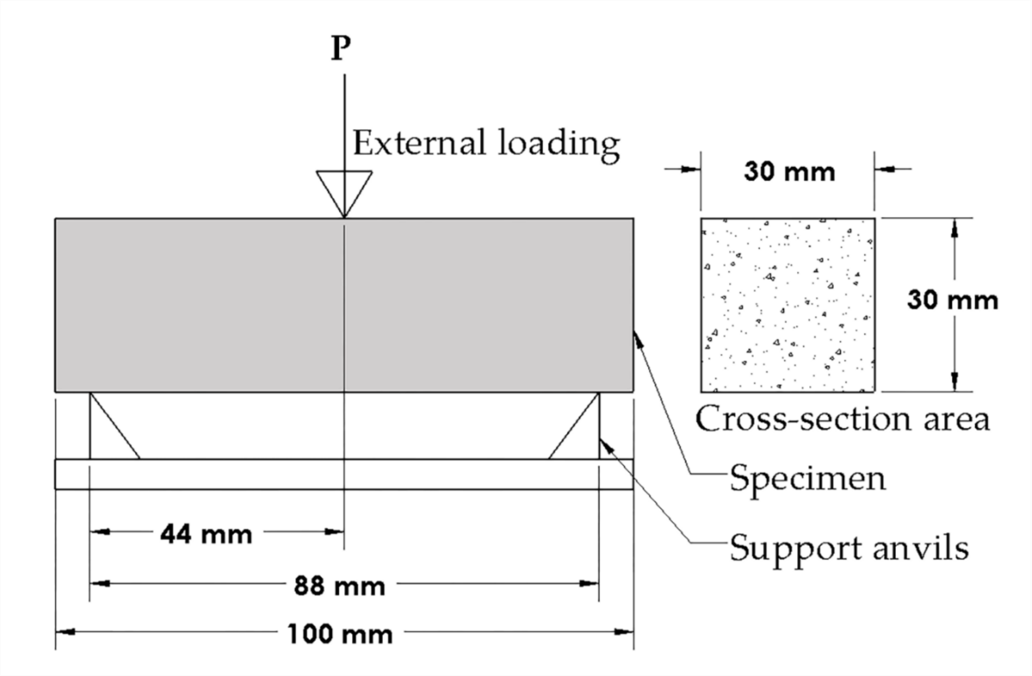

Figure 13 Schematic diagram of three-point bending test on mortar beam specimen

Fig. 14 shows the flexural strength results of the mortar beams for all the mixes measured at both 14-day and 28-day strength. Average flexural strength is presented for various mixes with error bars.

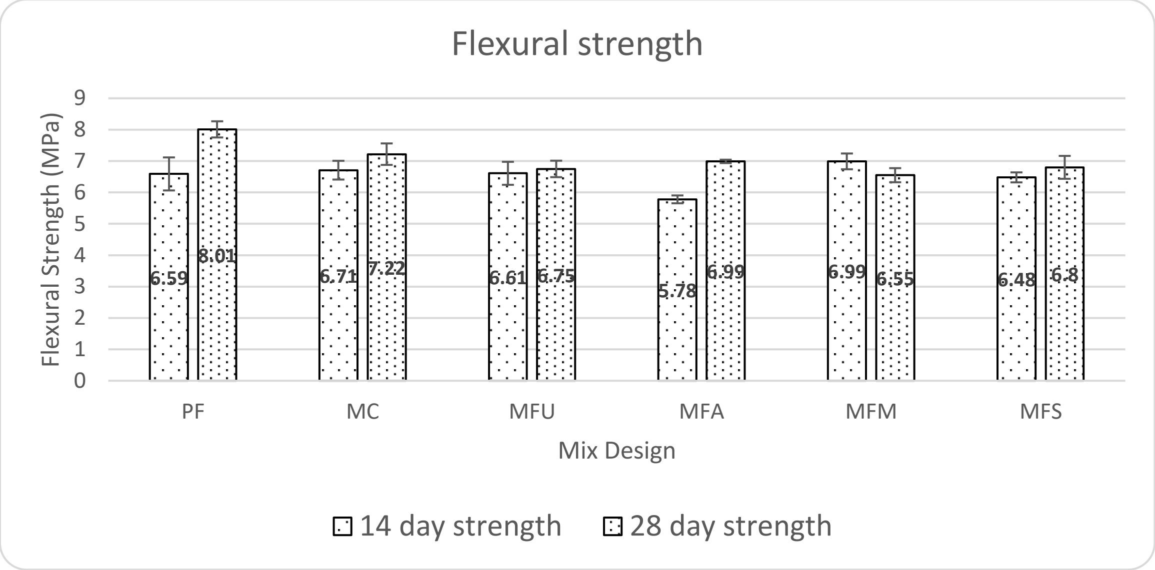

Figure 14 Flexural Strength of different mixes with 14-days and 28-days (red) strength

Considering the first peak behavior, the results do not indicate any significant change in the modulus of rupture after the addition of fibers. It should be noted that the average flexural strength at 14 days is slightly higher than that at 28 days for Mix MFM. It is most likely due to the high standard deviation of the mix as the errors bars for 14-day and 28-day flexural strength are mostly overlapped. This might be a consequence of the low dosage of fibers (0.2% by total weight) which in turn means that the surface area of fiber coated with the SCM is small. Other researchers [77] reported an improvement of as small as 1.94% when 5% metakaolin was replaced in OPC. This indicates that the addition of small amounts of metakaolin does not have a significant impact on the flexural strength of concrete.

One possible reason for the relatively neutral response of the flexural strength to the coating could be poor workability. In addition to polypropylene fibers, the workability of cementitious composites reduces with an increase in the dosage of fibers [78], [79]. The reduced workability is a likely factor that prevented proper compaction and placement of the mix in the small beam molds. This might have led to reduced strength when coated fibers were used in the mix.

2.4.4 Optical Microscopy

A preliminary investigation on the coated fiber samples was done using optical microscopy as shown in Fig. 15. A scale bar is also included in the images. Fig. 15(a) shows virgin untreated polypropylene fibers without any coating, Fig. 15(b) shows polypropylene fibers treated with metakaolin coating, and Fig. 15(c) shows silica fume coated polypropylene samples. Visually in Figs. 15(b) and 15(c), it appears that the fiber is uniformly coated either heavily or lightly with the SCM. Even distribution and uniformity of pozzolan material are further investigated under an SEM in section 2.4.5.

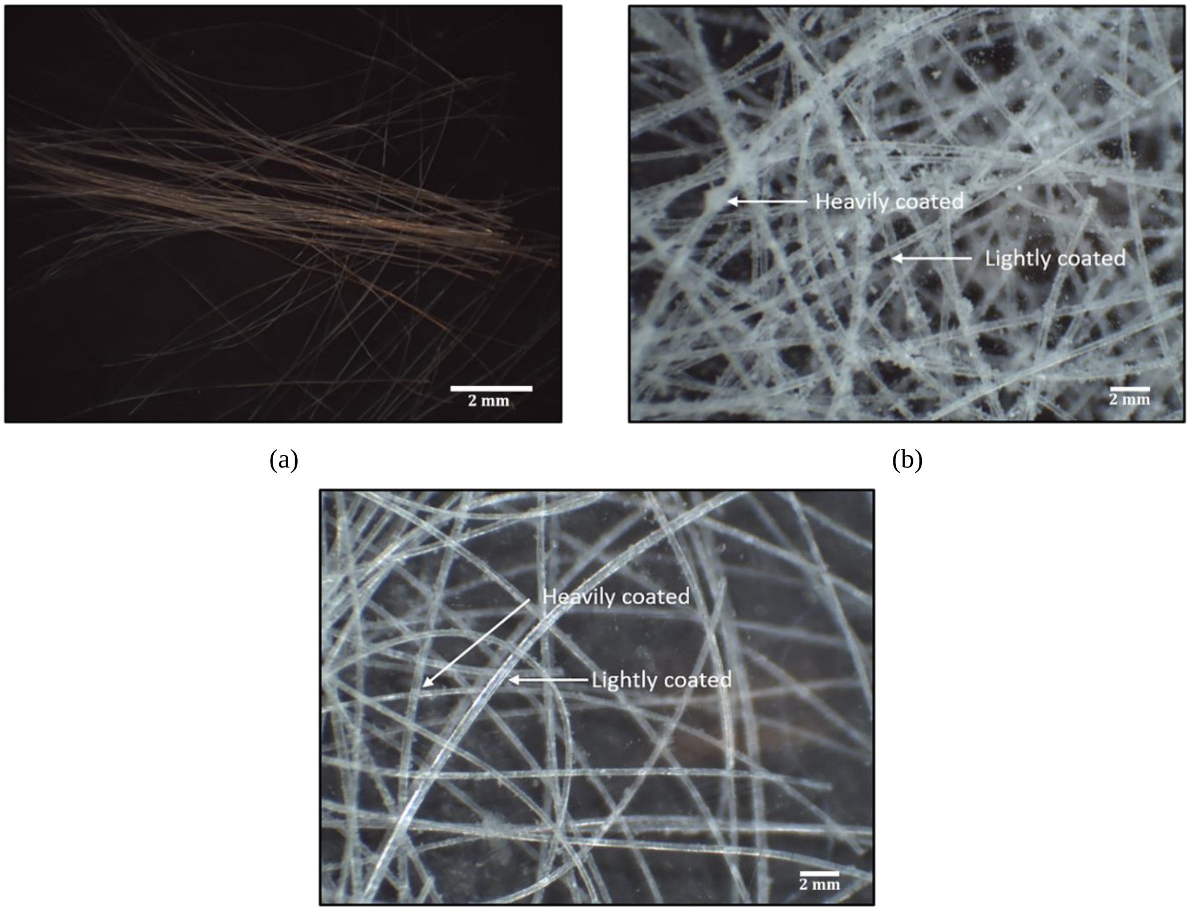

(a) (b)

(c)

Figure 15 Images showing various fibers used in the study: (a) untreated polypropylene (10x magnification) fiber; (b) polypropylene fiber coated with metakaolin (45x magnification); (c) silica fume coated polypropylene fiber (45x magnification)

2.4.5 Scanning Electron Microscopy

After the SCM coating procedure was carried out on fibers, they were analyzed under an SEM and energy dispersive X-Ray spectroscopy (EDS). The microscopy images revealed the presence of a varying concentration of SCM on the fiber surface. However, pozzolanic materials seem to be present throughout the surface. Since the effect of ITZ is progressive and is most significant in the first 15–20 µm closest to the reinforcement [38], even a small amount of coating can be sufficient to provide the desired results. The evenness of the coating was not visible using optical microscopy owing to the fine nature of the particles of the SCMs used; however, it was evident under the SEM. In Fig. 16 (a), the coating of metakaolin can be distinctly seen as brighter spots on the surface of the fiber. Bruker Quantax (EDS) System was used for X-ray spectroscopy to reveal the elements in the sample. The spectroscopy revealed peaks corresponding to elements such as silicon, oxygen, and calcium. The equipment demonstrates the ability to show the true spatial distribution of each element of interest in the given sample. The magnification level was set at 200x with an accelerating voltage of 15 kV and a working distance of 17.4 mm for the parent image. Using Fig. 16 (a) as the parent image, elemental mapping was done on it to reveal the positioning of the elements which showed spectrum peaks, as shown in Fig. 16 (b). The elemental mapping revealed the positioning of silicon (shown in Fig. 16 (d)) and oxygen (shown in Figure. 16 (e)) from the pozzolan (metakaolin) on the fiber surface. As indicated by the datasheet of metakaolin and other studies [80], it was inferred that the primary components in metakaolin were oxides of aluminum and silicon. Elements such as silicon and oxygen which corresponded to the peaks in Fig. 16 (b) were seen with their spatial distribution in Figs. 16 (d) and 16 (e), respectively. In Figs. 16 (d) and 16 (e), the distribution of the constituents of the SCM can be observed. Outline of the fibers in the parent image can be made out in the images showing elemental mapping, indicating the presence of SCM on the surface of the fiber.

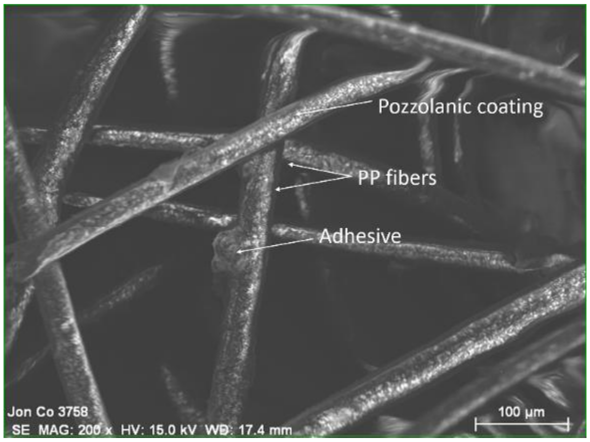
Pozzolanic coating
PP fibers
Adhesive
Jon Co 3758
SE MAG: 200 x HV: 15.0 kV WD: 17.4 mm
100 µm

(a)

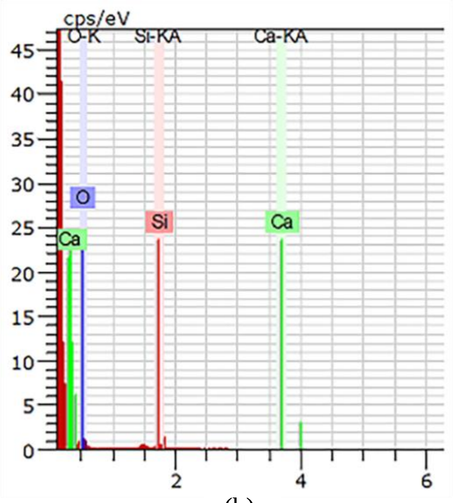
cps/eV
O-K
Si-KA
Ca-KA
O
Si
Ca
Ca
45
40
35
30
25
20
15
10
5
0
2
4
6

(b)

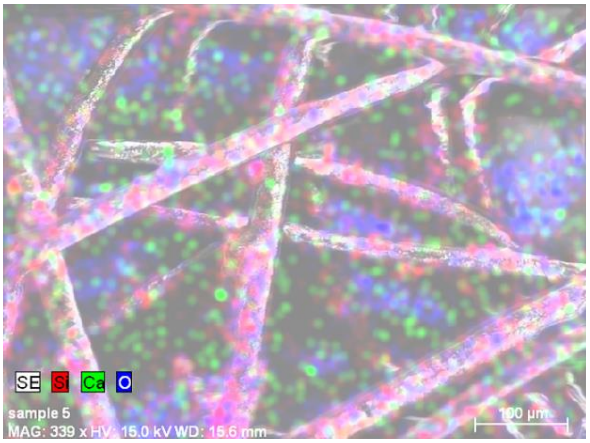
SE
Si
Ca
O
sample 5
MAG: 339 x HV: 15.0 kV WD: 15.6 mm
100 µm

(c)

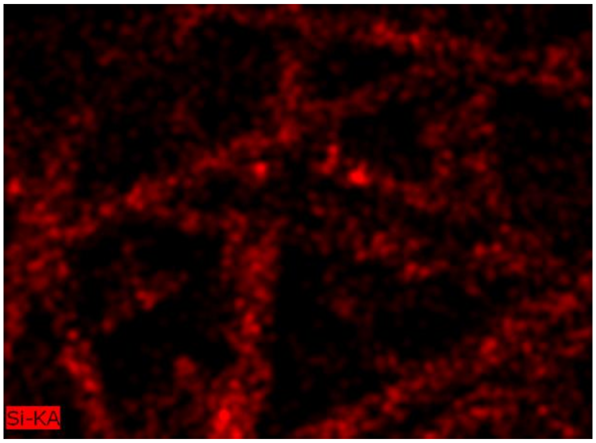
Si-KA

(d)

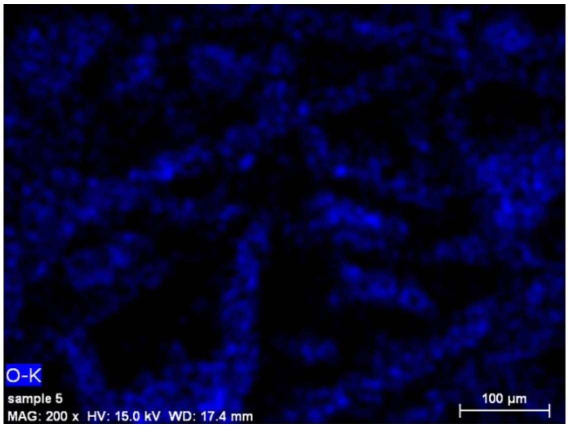
O-K
sample 5
MAG: 200 x HV: 15.0 kV WD: 17.4 mm
100 µm

(e)

Figure 16 SEM images of metakaolin coated fibers (clockwise from top left): (a) image showing coating at 200x magnification; (b) spectrum showing the constituent peaks; (c) elemental map of oxygen and silicon; (d) elemental map of silicon only; (e) elemental map showing oxygen only

2.5 Conclusions and Recommendations

Based on the study conducted, the following conclusions are drawn:

1. The compressive strength improved on the addition of metakaolin coated fibers when comparing MFU and MFM samples. In this study, by using 1/25th of the amount of metakaolin used in other studies, the strength increased by 13.47% as compared to the reported 3.27%.
2. The compressive strength of a cementitious composite is affected by not only the amount of SCM but also by the position they occupy in the matrix. By concentrating the SCM on the parts of the matrix where it is needed the most (boundaries of the reinforcement), an improvement of strength can be achieved by using a fraction of the SCM material.
3. PF mixture showed the highest tensile strength and flexural strength at 14 days and 28 days of curing respectively. The relatively high strength in mix PF indicates the presence of an inclusive and compatible mix of fibers by the supplier. This may be further confirmed with the microscopic investigation of Mix P. The material sample of PF mix studied under microscopy showed better dispersion and presence of finer fibers (~15 microns).
4. The bending strength tests did not show any significant improvement with the addition of fibers. This was attributed to the small dosage of fibers and low amounts of SCM.
5. Spectroscopy on the coated fibers indicated that the surface treatment procedure used in this study successfully coated the PP fibers with SCMs.
6. Recommendations for future work include using higher strength fibers at higher dosages to explicitly study the effectiveness of fiber coating. Additionally, developing and/or modifying existing methods to accurately quantify the improvement in fiber-matrix bond interactions such as using a fiber pullout method. Conducting 56-day tests to allow for

complete interaction between the coated fibers and released lime to take place may also be studied.

Acknowledgements: Financial support of Natural Sciences and Engineering Research Council of Canada (NSERC) is greatly appreciated. Involvement and guidance of Terry Bergen and Peter Dias from Read Jones Christoffersen Ltd. is also acknowledged. Assistance from technical staff Armando Tura and Geoff Burton is gratefully acknowledged. Assistance and inputs provided by Maryam Monazami is greatly appreciated. Assistance and guidance provided by Jonathan Rudge during SEM imaging is greatly acknowledged.

Author Contributions: Conceptualization, Rishi Gupta; Methodology, Rishabh Bajaj, Rishi Gupta, Boyu Wang; Software, Rishabh Bajaj; Validation, Rishabh Bajaj, Boyu Wang; Formal Analysis, Rishabh Bajaj, Boyu Wang; Investigation, Rishabh Bajaj; Resources, Rishabh Bajaj; Data Curation, Rishabh Bajaj ; Writing – Original Draft Preparation, Rishabh Bajaj; Writing – Review & Editing, Boyu Wang, Rishi Gupta; Visualization, Rishabh Bajaj, Boyu Wang; Supervision, Rishi Gupta; Project Administration, Rishi Gupta; Funding Acquisition, Rishi Gupta, Boyu Wang

Conflict of Interests: The authors declare no conflict of interest.

Chapter 3 Analyzing Bond-deterioration During Freeze-thaw Exposure in Cement-based Repairs Using Non-destructive Methods

Article Link: https://www.sciencedirect.com/science/article/pii/S0958946520303358

Boyu Wang[a], Rishi Gupta[b*]

[a] Graduate Student, Department of Civil Engineering, University of Victoria, 3800 Finnerty Road, Victoria, B.C., V8W 2Y2, CANADA; https://orcid.org/0000-0002-9983-7606

[b] Associate Professor, Department of Civil Engineering, University of Victoria, 3800 Finnerty Road, Victoria, B.C., V8W 2Y2, CANADA; https://orcid.org/0000-0002-3402-6095

* Corresponding author, Tel +1 (250)721-7033, email guptar@uvic.ca

Note: In the previous chapter (Chapter 2), the use of the SCM-coated fibers in the mix did not result in much improvement in the tensile and flexural performance of the mix. As a result, the author decided to not test the engineered mix with treated fibers under freeze-thaw and cyclic loading conditions until a better mix is found (perhaps with a higher fiber dosage). However, the experimental study in Chapter 2 advances the understanding of the mechanical (compressive, tensile and flexural) performance and microscopic behaviour of the commercially available repair mixes, which to some extent paves the way for the studies in this chapter.

This chapter (Chapter 3) is adapted from the paper that has been published in Journal of Cement and Concrete Composites (Elsevier), with permission where appropriate. This chapter highlights the use of three NDT techniques to determine the FT damage of repaired concrete structures. The destructive bond flexural test results are found well correlated with NDT results. The empirical models are proposed which can be used to predict the load-bearing capacity of beams after FT exposure based on NDT measurements.

3.1 Abstract

Cement-based repair materials are extensively used to rehabilitate damaged structures and extend their service life. However, these materials experience bond deterioration and strength loss during service. Traditional standardized test methods for bond determination are destructive and impose additional damage in parent structures. This paper presents findings of a unique study where a combination of force and acoustic sensors were used to determine the dynamic modulus of elasticity (E_{dyn}), which reflects the interfacial deterioration and material damage. Flexural bond test and image analysis were performed to validate the results. The experimental study shows that the change in E_{dyn} determined from non-destructive tests (NDTs) agree well with the change in other measurements including flexural bond strength (f_r'), interfacial crack width, and mass loss after freeze-thaw exposure. Linear relationships are established between E_{dyn} and f_r' for both cementitious and polymer-modified cementitious repair mortar with a coefficient of determination ranging from 0.87 to 0.95.

3.2 Introduction

Deterioration of cementitious materials due to weathering has become a major concern for many infrastructures such as high-rise buildings, bridges, airport pavements, etc [81]. Since replacing the entire deteriorated structure is not always feasible, cost-effective, or sustainable, repair work is a common practice to restore and extend the service life of these structures. To restore the concrete's structural capacity, the deteriorated concrete must be removed and replaced with a new layer of repair materials. Many new repair materials are developed each year for various purposes [82], but they can be mainly divided into three categories, i.e., cement-based materials, polymer modified cement-based materials, and polymer or resin materials [83]. The first two categories form the focus of this study. The conventional Portland cement-based repair materials have served the construction industry well for several decades, but its performance was reported to be less satisfactory in some instances, especially in aggressive exposure environments [84]. Thus, polymer modified cement-based mortar was introduced to overcome these shortcomings. The polymer modifiers for Portland cement ranges from primarily styrene butadiene, acrylic, and some vinyl co-polymers to pure polymers such as epoxy resins, polyesters, and some polyurethane-based systems [84], [85].

In Canada, concrete may be subjected to a wide range of exposure conditions, some of which severely tax concrete’s durability. One of the most aggressive exposure conditions is associated with freezing and thawing (FT) cycles [86]. Several theories have been proposed to explain the frost damage mechanism. Among them, the two theories that are most recognized by researchers include hydraulic pressure theory [87]–[92] and osmotic pressure theory [87], [93], [94]. However, these two models have several limitations. They cannot predict the mechanical response of the deformable porous cementitious paste due to the original assumption that considered the paste to be rigid [14]. Also, the hydraulic pressure model predicts the proportionality of the hydraulic pressure to the cooling rate, which is against the test observations [15]. To date, the mechanics of FT in concrete are best understood by poromechanical theory [95]–[97]. Poromechanics [98], [99] extends Powers hydraulic pressure theory such that the deformation of the cement matrix and the development of cryo-suction in air voids is accounted for. Based on the framework of poromechanics, recent advancements [100], [101] are made in the development of a more complete thermo-hydro-mechanical model that examines the FT behavior of concrete. The major outcome of the poromechanical model is the establishment of the microstructural features of concrete including critical spacing factor, matrix permeability, and degree of saturation [102]. The spacing factor was found to increase as a function of degree of saturation, which results in increased tensile strain and damage on the cementitious matrix. It was reported that the fully saturated (100% degree of saturation) mortar showed dramatic expansion during freezing as opposed to a slight contraction of partially saturated (17% degree of saturation) mortar [102]. In the context of this study, repaired concrete beams are immersed in the water during freezing to simulate the most severe conditions. It is imperative to ensure adequate FT resistance not only for repair material itself but for the bond between the substrate and repair materials.

Mirza et al. [16] investigated the FT performance of repair materials modified by two types of polymers, i.e., styrene butadiene rubber and acrylics. Results showed that 11 out of 13 polymer-modified cement-based mortar mixes outperformed plain cement-based mortars by having at least

50% less loss in mass after 300 FT cycles. Assaad et al [103] investigated the frost resistance of polymer-modified mortars as compared to normal air-entrained mortars. They found that during FT cycles, the addition of styrene-butadiene rubber can enhance the flexibility of the materials to better accommodate the deformations along the repair bonding interface. As a result, polymer-modified mortars can more efficiently control the bond strength drop as opposed to air-entrained mortars. Qian et al. [17] studied the adhesive tensile strength of Portland cement mortars and polymer-modified cement mortars under FT cycles. Results showed that polymer-modified cement mortars had less drop in dynamic elastic modulus and better bond performance, which agrees with the findings of Mirza et al. [16]. Li et al. [18] investigated the FT durability of several rapid-setting concrete repair materials including polypropylene fiber-reinforced concrete and Portland cement concrete. It was found that FT cycling had less effect on splitting tensile strength of fiber-reinforced concrete than plain concrete. Many studies have previously reported that the incorporation of polymers greatly improves the strength [104]–[106], adhesion [107], impermeability [106], and chemical resistance [105], [108] of mortars and concrete. However, authors found limited studies that assessed the effect of FT cycles on bond characteristics of polymer-modified cement-based materials and other types of repairs, which will be investigated in this study.

After FT exposure, it is important to ensure repair materials are well bonded to the parent structures. To determine interfacial bond strength between concrete substrate and overlay, many test methods have been developed. The existing destructive test methods can be divided into three categories [109]. The first category of tests include pull-off [110], direct tension [111], and splitting test [112], which measures the bond under tensile stresses. The second category of tests measures the bond under shear stresses and are called direct shear methods. Several tests such as L-shaped [2], mono-surface shear [2], and bi-surface shear test [111] fall into this category. The third category measures the bond strength under combined shear and compression stresses. The most commonly used test is the slant shear test [113], [114], which loads a composite cylinder made of two identical halves bonded at 30° under axial compression load. However, the aforementioned destructive methods are usually insufficient for interface quality evaluation in large areas [19], [20]. Further, the destructive methods are time-consuming, and the number of measurement points is limited due to the fact that damage arising in the course of conducting the tests needs to be repaired. To address these shortcomings, the non-destructive test (NDT) methods form a key focus of this study.

To date, NDT methods including three-dimensional (3D) laser scanning method [21], [22], impulse response [23], impact-echo (IE) [24], and ultrasonic pulse velocity (UPV) test [25] were used to assess the bond strength of the materials. The 3D laser scanning method uses a 3D laser scanner to evaluate the morphology of selected surfaces that will receive the repair. The pull-off adhesion of these surfaces can be assessed based on the empirical relationships established between the surface roughness parameters and the pull-off strength. The major issue of this method is that it is inaccurate to determine the pull-off adhesion on the sole basis of the surface roughness [21]. As compared to this, the UPV method measures the stress wave velocity passing through the specimen to assess the adhesion strength. The issue with this method is that the roughness of the surface can significantly distort the ultrasonic wave [24], [25]. IE and impulse response methods are less affected by the heterogeneity of concrete as opposed to the UPV method and thus are considered promising methods for adhesion assessment [23], [24]. The IE method uses a low energy impact of a steel ball to generate stress waves that pass through the structure. These waves are reflected by internal flaws or interfaces giving rise to a transient thickness resonance [115]. The thickness resonance produces one dominant peak in the frequency spectrum, which can be readily identified. Lin et al. [116], [117] observed noticeable peaks in frequency spectrums where the unbonded fraction of the repaired area increased to greater than 20%. However, they concluded that the variations in interfacial bond tensile strength do not affect impact-echo test results. Garbacz et al. [19] made further attempts to evaluate the relationship between pull-off bond strength and amplitudes of the bottom and interface frequency peaks. No statistical significance could be found between frequency amplitudes and the pull-off strength. Besides these limitations of the IE test, the speed of testing is considerably slow [23], [118]. The impulse response test, on the other hand, is a relatively faster screening method. The test involves striking an object with an instrumented hammer and measuring velocity response using a velocity transducer. The impact force and surface velocity response are used for condition assessment [119]. Numerous studies [23], [120]–[122] have reported that the impulse response method is able to capture debonding or delamination of concrete overlay and a variety of other defects [123].

In summary, past research showed that IE and impulse response methods are promising in terms of bond adhesion assessment, however, authors could not find any reported studies on the applicability of these NDT methods on FT-damaged structures. Additionally, most literature [20]–[25], [118] only focused on correlating pull-off strength with NDT measurements. However, a single pull-off test may not be the true representation of the load-bearing capacity of the repaired structures as the test results from using pull-off, splitting tensile, and other test setups scatter enormously [111].

This study introduces the use of several NDTs to evaluate the true load-bearing capacity of the repaired structures after FT exposure. These NDT methods include resonant frequency, hammer percussion, and modified chain drag methods, some of which have a faster testing speed and potentially better detectability compared to IE and impulse response method. The detectability of these methods for sub-surface delamination has been proven in a previous study by Blaney and Gupta [124], and the working mechanism of these NDT methods will be introduced in detail in the following section. This study proposes empirical equations relating NDT measurements and flexural bond strength of the repaired structures after FT exposure. In addition, interfacial crack width, crack tortuosity, and mass loss of the tested specimens are used to validate NDT measurements. The findings of this study will contribute to development of a faster evaluation method of bond and deterioration of repair materials after FT exposure.

3.3 Experimental Investigation

3.3.1 Materials

Four types of materials were used including one lab-prepared concrete mix and three types of commercially available cement-based repair materials. The intent of the lab-prepared concrete (Mix S) is to serve as the parent material that receives repair. The parent concrete had a target strength (f_c') of 50 MPa to minimize material degradation as a result of FT exposure such that the performance of the different repair materials could be distinguishable. Also, the target air content for Mix S was set as 5% - 8%, which would allow sufficient FT resistance in Mix S. The slump of

Mix S is adjusted such that it lies within the range between 25 mm (1 inch) and 100 mm (4 inches) as recommended by ACI 211.1 [125]. The mix design for the lab-prepared concrete is shown in Table 2, and the gradation curve of the aggregates of Mix S is shown in Fig. 17. According to ASTM C136 [126], the fineness modulus of fine and coarse aggregates are 2.85 and 6.48 respectively. Chemical admixtures including high-range water reducing agent (HWRA) and air entraining agent (AEA) are used to reduce water usage and increase the entrained air content, which improves the FT resistance of the parent concrete. According to the product data sheet, the HWRA meets ASTM C494/C494M [127] requirements for Type A, water-reducing, and Type F, high-range water-reducing admixtures. The AEA used in this study meets the requirements of ASTM C260 /260M [128].

The other three mixes are termed Mix F, M, and P in this study and were procured from suppliers in 25 kg (Mix F and Mix M) and 22.7 kg (Mix P) bags. The maximum aggregate size of Mix F, M, and P is 9.5 mm, 2.36 mm, and 1.18 mm respectively. As per the recommendations from the manufacturers, 2.5 kg, 2.37kg, and 4.26 kg of water were added to each bag of Mix F, M, and Mix P respectively. The corresponding water-to-material (w/m) ratio of various mixes by weight are summarized in Table 3. Mix F, M, and P can be classified as cementitious repair concrete, cementitious repair mortar, and polymer-modified cementitious mortar respectively. Mix P contains polypropylene fibers with an approximate dosage of 0.2% by weight of all the constituents in the mix [129]. By means of a scanning electron microscope, the diameter and length of a single polypropylene fiber was measured to be 36 microns and 6 mm respectively. Table 3 summarizes the fresh and hardened properties of the four mixes. Slump, air content, and compressive strength were determined as per ASTM C 143 [130], ASTM C231 [131], and ASTM C39 [132] respectively, and the setting time is provided by the material manufacturers. More in-depth information about the properties of the repairs used in this study can be found in Wang et al. [133], [134] and Bajaj et al. [129]. However, due to the proprietary nature of the repairs, the detailed information about materials’ constituents is not available.

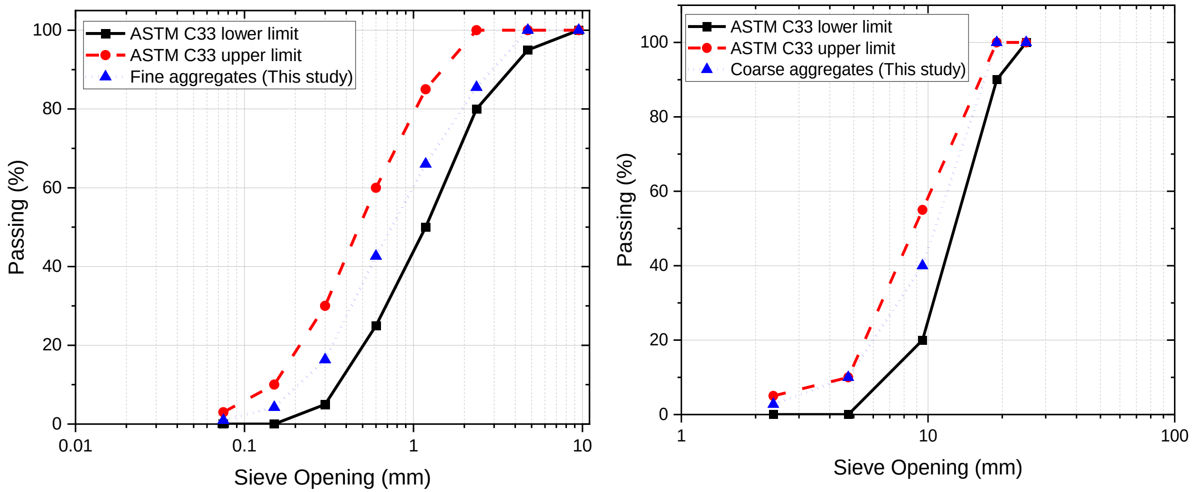

(a)

(b)

Figure 17 Gradation curves of aggregates of Mix S (a) Fine aggregate (b) Coarse aggregate

Table 2 Mix proportions of Mix S $(\boldsymbol{kg/m^3})$

Material	Type I Cement	Gravel	Sand	HWRA[a]	AEA[b]	Water
Mix S	450	1053	762	2.25	2.25	153.7

[a]HWRA: High-range Water Reducing Agent

[b]AEA: Air Entraining Agent

Table 3 Fresh and hardened properties of concrete and repair mixes

Category	Mix	Slump (mm)	Hardened density at 28 days (kg/m^3)	28-day Compressive strength (MPa)	Air content	Setting time (min)	w/m ratio
Parent	S	60	2530	59.4 ± 1.4	4.9%	90	0.067
Repair	F	80	2374	55 ± 2.2	5.1%	-	0.1
Repair	P	15	2289	39.5 ± 1.3	7%	9	0.18
Repair	M	70	2325	68 ± 2.4	5.0%	75	0.09

3.3.2 Specimens

In the field, especially in bridge decks or parking garages, a common maintenance process consists of removal of deteriorated concrete on the tension side, cleaning of substrate concrete, and surface preparation for repair [135]. This study simulates this in-situ repair condition by casting prismatic beams with an induced cavity. Mix S was first placed into the mold where a specially created 3D printed block was attached to the bottom of the mold. The plastic block had known surface roughness and was produced by 3D scanning the concrete surface profile (CSP) chip and then 3D printing on a plastic base. The benefit of using 3D printed blocks is that it can remove any variations associated with preparing the surface that receives the repair. The CSP chip #6 was selected as the base model for 3D scanning. According to the ICRI Technical Guideline No. 310R-2013 [136], CSP chip #6 simulates the surface profile after using methods including abrasive blasting, shotblasting, high/ultra high-pressure water jetting, scarifying, surface retarder, and rotomilling for surface preparation. Hence, this was selected as an appropriate level of surface roughness for the parent specimen. After concrete placement in molds, ten seconds of table vibration was used to consolidate the concrete. After 24 hours of curing in ambient conditions at 18 ± 2℃, inserted blocks were removed from the mold and three types of repairs, Mix F, M, and P were applied to the notches. The steps for specimen preparation explained above are shown in Fig. 18. It should be noted that the side surface of the repaired section is left unroughened as the current repair codes and standards [135], [136] have no stipulations regarding that.

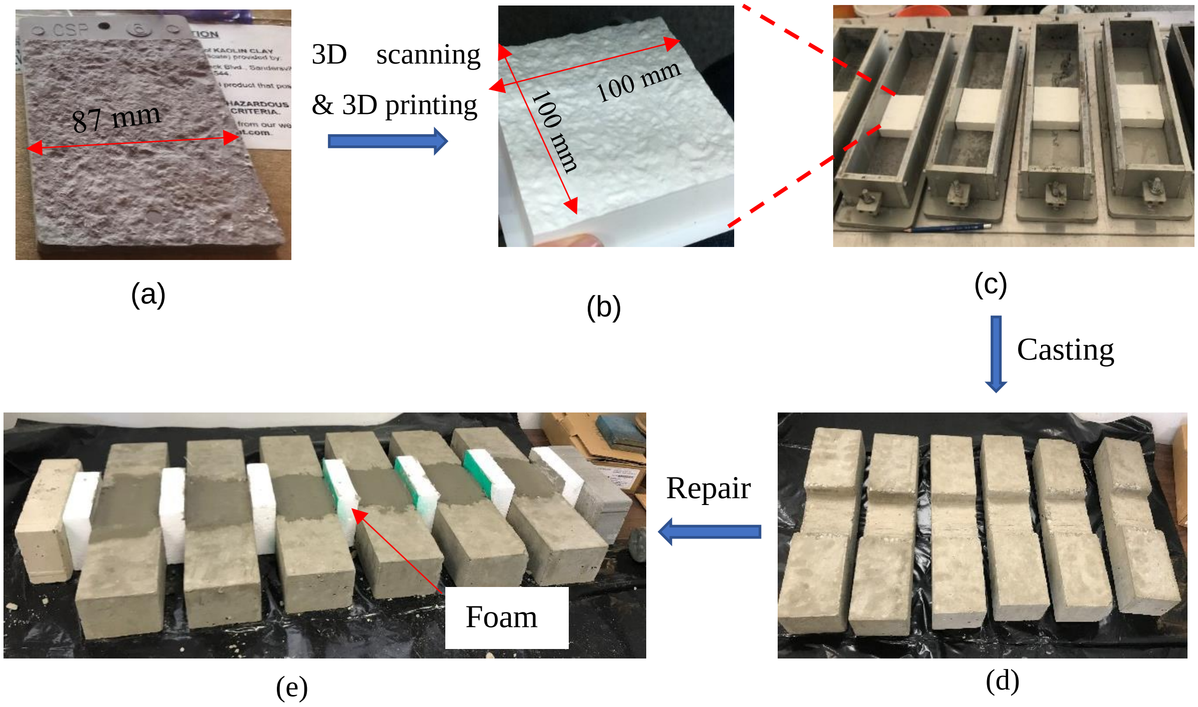

Figure 18 Procedure for preparing repaired specimens (a) #6 CSP chip (b) 3D printed chip (c) concrete mold (d) specimens with a simulated cavity (e) repaired specimens

As per the recommendation of the material suppliers, Mix F is required to be applied only when the minimum dimension of the repair is more than 25 mm (1 inch), whereas Mix M has a requirement of the maximum depth of 25 mm. Therefore, for consistency, all specimens to be tested have an induced cavity of 25-mm depth. Due to the fast setting characteristics of Mix P, the supplier recommends that the repair volume not exceed $0.001\ m^3$. Keeping all of these constraints in mind, the induced cavity had a dimension of 25 mm x 100 mm x 100 mm. The overall size of the specimen was 100 mm x 75 mm x 400 mm according to ASTM C666 [137], as demonstrated in Fig. 18. After receiving the repair, specimens were cured at ambient conditions at 18 ± 2℃ (relative humidity around 60%) for 24 hours and then transferred to a water bath. Water curing temperature was maintained at 23 ± 2°C, and all specimens were cured for 28 days before being exposed to FT cycles in a test chamber. Specimens were also constructed as control with no cavities.

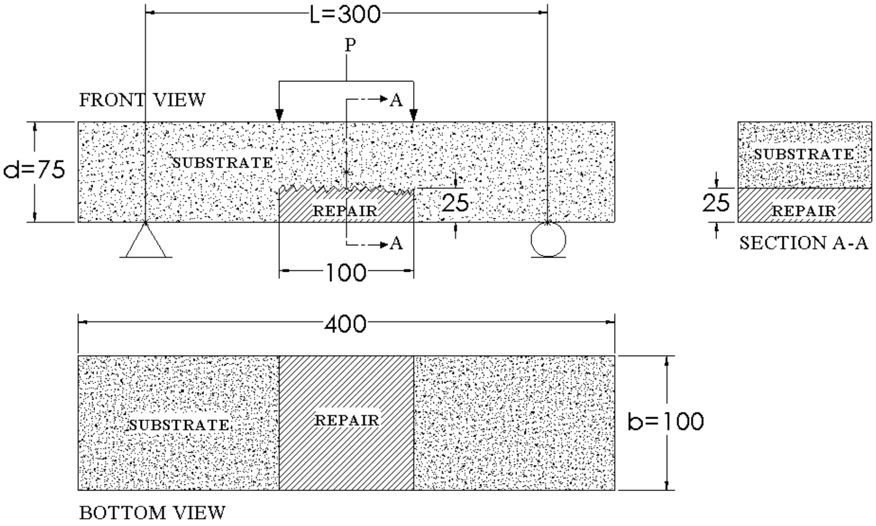

Figure 19 Schematic of flexural testing on repaired prisms (all dimensions are in mm)

3.4 Methods Implemented and Equipment Used

3.4.1 Freeze and Thaw (FT) Test

Humboldt HC-3186S.4F freeze-thaw cabinet was used to perform the tests. The test was conducted following ASTM C666 [137] procedure A, i.e., rapid freezing and thawing in water. One FT cycle consists of lowering the temperature of the specimens from 4 to -18℃ and raising it from -18 to 4℃ in around 3.5 hours. Within one FT cycle, the time of freezing and thawing period is approximately equal. In this work, after 0, 30, 60, 90, 150, 210, 270, and 300 cycles of FT, NDT methods were used to determine the resonant frequency and calculate the dynamic modulus of elasticity (E_{dyn}) of the repaired specimens. All NDTs were performed on specimens at saturated surface dry (SSD) condition at room temperature of 18 ± 2℃.

3.4.2 Non-destructive Test (NDT) Methods

3.4.2.1 Hammer percussion sounding

Hammer percussion method utilizes hammer striking to introduce acoustic disturbance to concrete specimens, and a microphone to collect the acoustic response. The concrete vibration is recorded via the reflected wave in the air in a manner similar to an air-coupled impact echo procedure [138]. The acoustic signal can be further processed to extract useful information such as resonant frequencies. The data acquisition process of hammer percussion method is simpler compared to impulse response method as a non-contact acoustic recorder is used and thus has the potential of saving testing time. In this study, a 56.7-gram (2-ounce) steel ball hammer was used for impacting the specimens, and a set of microphone and audio recorder were used to collect the resulting acoustic response. The specimen was placed on a sponge rubber pad with a hammer striking the center of the rectangular surface, as shown in Fig. 20(a). The audio recording was performed using a Zoom H1 digital voice recorder. This recorder has a maximum sample rate of 96 kHz at 24-bit depth, which means the vibration frequency as high as 48 kHz can be captured. Further, Zoom H1 is capable of analog-digital conversion at 24-bit depth, which ensures high precision in post-production. The microphone used was a Polsen OLM-20 Dual Omnidirectional Lavalier Microphone. The microphone has two channels collecting two mono signals, so the channel that is closer to the specimen surface was used for post-processing in this work. Audacity® audio software was used to trim the acoustic signal such that the environmental noises collected before and after the hammer impact can be eliminated. MATLAB© was used to perform a single-sided fast Fourier transform (FFT) on WAV files, and the peaks were identified as resonant frequencies.

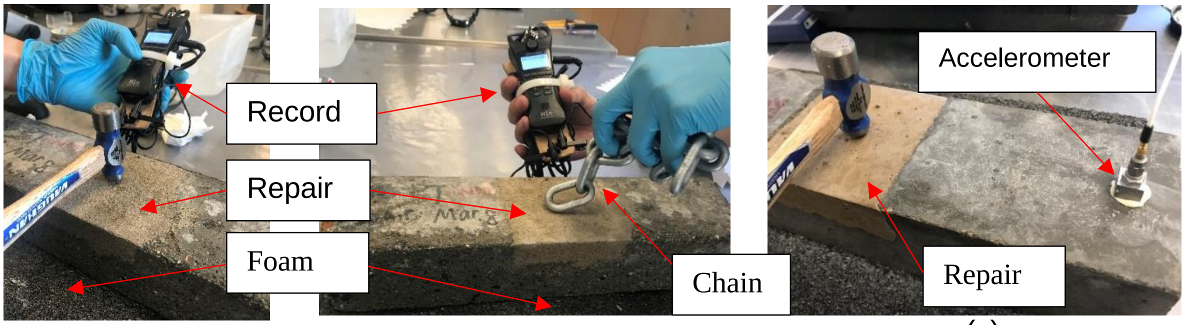

(a) (b) (c)

Figure 20 NDT test configurations (a) Hammer percussion test configuration (b) Modified chain drag test configuration (c) Accelerometer configuration for hammer impact test on specimens

3.4.2.2 Modified chain drag

Chain drag has been adopted by ASTM D4580 [139] to determine the delamination of bridge decks, but it suffers from limitations due to the subjectivity of the test performer. Modified chain drag overcomes that issue by involving the use of an audio recording system to collect acoustic responses when the chain is dragged over the concrete surface [124]. In this work, a heavy-duty chain with a link diameter of 9.5 mm (3/8 inch) and a total link length of 100 mm (4 inches) was used. The specimen was placed on a sponge rubber pad allowing free vibration. The sounding signal was recorded when the chain was dragged longitudinally across the repair. The same audio recording system and data processing technique were used as the hammer percussion sounding method. The benefit of using a chain as opposed to a hammer is that it can cover a relatively larger area in a short time as opposed to point measurements when using a hammer. The test configuration is shown in Fig. 20(b). It should be noted that the excited spectrum has a larger amplitude using a hammer than that using a chain. Also, the use of a hammer will only cause one peak showing in the excited spectrum while the use of a chain link generates multiple peaks due to the random vibration of the beam.

3.4.2.3 Resonant frequency test (RFT)

The use of an accelerometer has been standardized by ASTM C215 [140] to determine the change of resonant frequency and hence dynamic elastic modulus. In this study, an Olson Instruments RTG-1 Resonance Test Gauge which has a built-in data acquisition system and a PCB Piezotronics 353B15 accelerometer were used. When determining the transverse frequency, the accelerometer was attached near the end of the specimen with the hammer striking the middle of the specimen. The transverse frequencies are measured in this study, and the test configuration is shown in Fig. 20(c).

Dynamic modulus of elasticity is one of the most important parameters depicting mechanical performance such as the compressive strength of concrete. ASTM C215 [140] specifies determination of the dynamic elastic modulus based on the resonant frequency of the specimens. Eq. 3 and Eq. 4 are used to calculate the dynamic elastic modulus and relative dynamic elastic modulus. In this study, three prismatic specimens were tested for each mix and the test was repeated three times for each specimen resulting in 36 readings after every 30-60 FT cycles between 0 and 300 cycles.

$$E_{dyn} = \mathrm{CM}n^2 \tag{3}$$

$$P_c = \frac{(E_{dyn})_c}{(E_{dyn})_{c=0}} \times 100\% \tag{4}$$

Where,

C is the dimensional factor of the specimen (refer to ASTM C215 [140] for steps to calculate *C*), *M* is the mass of the specimen, *n* represents the fundamental transverse frequency, $\boldsymbol{P_c}$ is the relative dynamic modulus of elasticity after *c* cycles of freezing and thawing, $\boldsymbol{(E_{dyn})_c}$ is the dynamic modulus of elasticity after *c* cycles of freezing and thawing, $\boldsymbol{(E_{dyn})_{c=0}}$ is the dynamic modulus of elasticity at 0 cycles of FT.

3.4.3 Flexural Strength Test

The flexural strength of the repaired prisms was determined under a third-point loading arrangement. Material Test System (MTS) 810 was used to load the specimen with the repair materials on the tension side following ASTM C78 [141]. The beams were loaded at a rate of 2323 N/min ($522.2\, lbf/min$) such that the maximum stress on the tension surface increases at 1.2 MPa/min, as specified by ASTM C78. The flexural strength of the repaired beams is indicative of the bond strength between concrete and the repair materials. The schematic of the test setup is shown in Fig. 19. Eq. 5 was used to calculate the flexural strength.

$$f_r' = \frac{PL}{bd^2} \tag{5}$$

Where,

$\boldsymbol{f_r'}$ is the modulus of rupture, P is the maximum applied load on the beam, L is the span length, b and d respectively are the width and depth of the specimen.

3.4.4 Statistical Analysis

In this study, analysis of variance (ANOVA) method was used to test if there is a statistically significant difference among the dynamic elastic moduli measured by three different NDT methods. The null hypothesis, denoted by H_0, is the claim that is initially assumed to be true. In the context of this study, the null hypothesis is that dynamic elastic modulus values measured by three different NDT methods have no statistically significant difference. The ANOVA test is performed with the software MATLAB$^{©}$. So far, ANOVA is widely used to determine if the analyzed parameters have a statistically significant effect on the output parameters, and method details can be found in many statistics textbooks, e.g. [142].

3.5 Experimental Results and Discussion

3.5.1 Surface Scaling and Mass Loss

Fig. 21 presents the surface condition of representative specimens of different mixes after exposure to a total of 300 FT cycles. The surface scaling due to FT was inspected by visual examination in accordance with ASTM C672 [143]. Based on this standard, the visual ratings of surfaces include 0 (no scaling), 1 (very light scaling), 2 (slight to moderate scaling), 3 (moderate scaling), 4 (moderate to severe scaling), and 5 (severe scaling). It was observed that Mix S (Control mix) had a rating of 3 as some aggregate particles were visible. In comparison, Mix F-repaired beams exhibited more severe scaling damage, which can be classified as rating 4-5 because coarse aggregates are visible over the entire repaired area. The difference between these two mixes in scaling resistance could be attributed to the pore microstructures. As shown in Table 3, the air content of freshly mixed concrete Mix F and Mix S is similar, i.e., 5.1% and 4.9% respectively, expressed as a percentage of the concrete volume. However, Mix S contains 0.05% (by weight of the cement) air entraining admixture (AEA), which could result in a generation of stable, small-size, and well-distributed air bubbles in the concrete matrix [144], [145]. These air bubbles will remain intact while the concrete is hardening and provide enough room for freezing water to expand in the pores. ASTM C672 is not applicable to mortar mixes and hence changes in scaling for Mix M and P were not quantified using these scales.

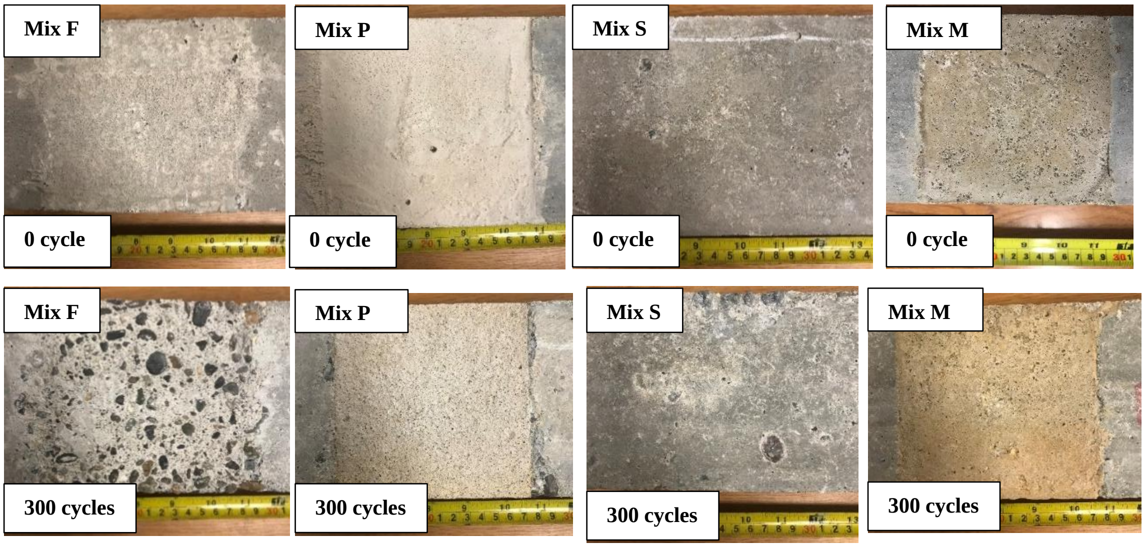

Figure 21 Surface scaling of different mixes due to FT

From 0 to 300 cycles, mass loss of Mix F reached up to 6%, with Mix S (control mix) losing 2.5% mass, Mix M losing 0.17% mass, and Mix P gaining 0.8% mass, as shown in Fig. 22. The percentage mass loss of Mix F-repaired beams was the highest among all mixes, which matches the observation that Mix F had severe surface scaling. Mix M (cementitious repair mortar) showed little change in mass after 300 cycles, which could be due to the high strength of the material. According to the poromechanical theory [100], FT damage occurs when the hydraulic pressure associated with water freezing in pores exceeds the strength of concrete regardless of the effect of entrained air. The average compressive strength of Mix M (68 MPa) at 28-day is the highest among all the mixes which could be beneficial for FT resistance. Mix P (polymer-modified cementitious mortar), showed a mass gain of 0.8% after 300 cycles. As seen in Fig. 22, the average mass of Mix P experienced a gradual increase by approximately 0.02% from 0 to 210 FT cycles, after which mass starts to drop. It is suspected that from 0 to 210 FT cycles, ongoing cement hydration outpaced the frost damage and a similar phenomenon was observed regarding dynamic elastic modulus in another study [146].

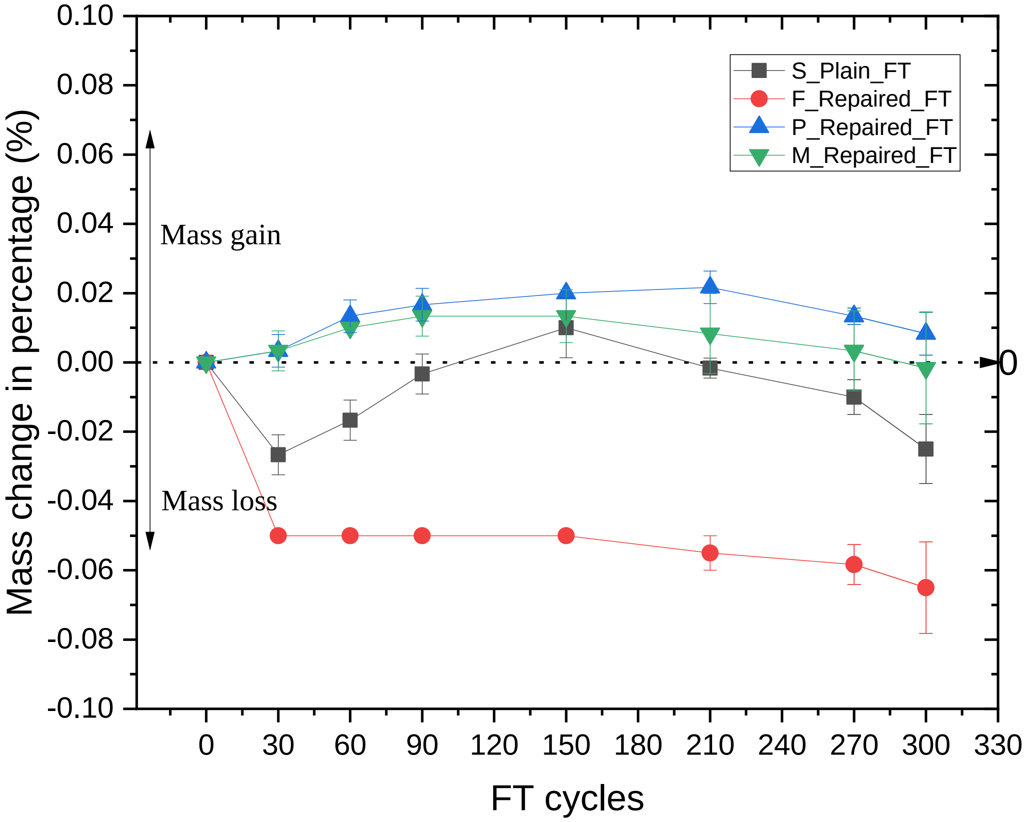

Figure 22 Mass loss of all mixes vs. FT cycles

3.5.2 Dynamic Modulus of Elasticity

Dynamic elastic modulus (E_{dyn}) is an important property that indicates the internal damage caused by freezing and thawing. In this study, E_{dyn} is calculated from the resonant frequency of the 1st mode. Fig. 23(a) and Fig. 23(b) shows examples of vibration signal in the time domain and Fig. 23(c) and Fig. 23(d) shows the corresponding frequency spectrum results after fast Fourier transform (FFT) is performed in MATLAB©. The spectrums have been normalized by diving the amplitude by the amplitude at 0 FT such that the change in amplitude after FT damage is visually easy to see. According to vibration principles [147], the resonant frequency of the 1st mode of a prismatic beam with a free-free end can be estimated using Eq. 6.

$$f_0^{estimate} = \frac{4.73^2}{2\pi L_{total}^2}\sqrt{\frac{E_{dyn}Ig}{A\rho}} \qquad (6)$$

Where $f_0^{estimate}$ is the estimated resonant frequency of the 1st mode in Hz, L_{total} is the total length of the prismatic beam in m, I is moment of inertia in m^4, g is gravitational acceleration in m/s^2, A is cross-sectional area in m^2, E_{dyn} is the dynamic modulus of elasticity in Pa. Using the experimental data summarized in Table 3, the resonant frequency of the specimens in this study can be estimated and is roughly 2000Hz. Therefore, the frequency in Fig. 23(c) and Fig. 23(d) has been limited from 1000Hz to 3000Hz to frame the peaks of interest appropriately. As can be seen in Fig. 23(c) and Fig. 23(d), there is a clear shift of resonant frequency after 300 FT cycles, which represent material and bond deterioration. Also, it should be noted that more noises can be observed in the frequency spectrum for specimens after 300 FT cycles of exposure, especially when the modified chain drag method was used. This phenomenon was observed in most of the specimens tested in this study. Sun et al. [148] reported that multiple chain links can sometimes generate unwanted noises due to the added noise of chain links bumping into each other. After 300 FT cycles, the surface of the specimens became rougher, which causes chain links to vibrate in a higher amplitude and thus higher chances of collision between chain links. The issue of unwanted noises could be mitigated by the use of a single-link chain [124].

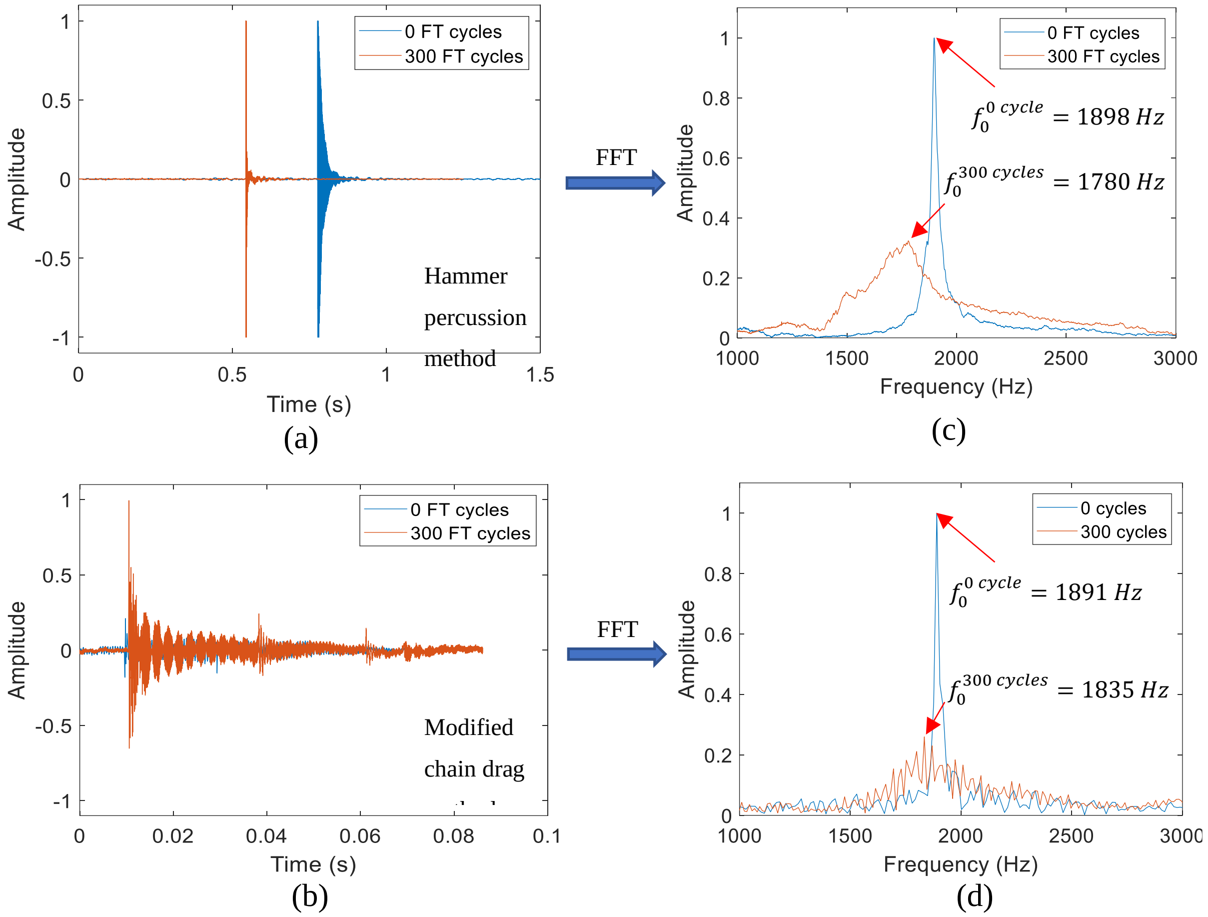

(a) (c)

(b) (d)

Figure 23 Example of frequency analysis (a) Vibration signal of hammer percussion method (b) Corresponding frequency spectrum (c) Vibration signal of modified chain drag method(d) corresponding frequency spectrum

Fig. 24(a) – (b) shows the change of elastic modulus with increasing FT cycles measured by RFT and acoustic methods described earlier. The elastic modulus was calculated based on resonant frequency obtained. All three repaired specimens, along with the plain specimens, experienced a loss of elastic modulus after exposure to FT cycles. There is plenty of research on the damage mechanism during the FT test, and it has been found that the loss of elastic modulus of the materials is related to the generation of the microcracks [90], [146].

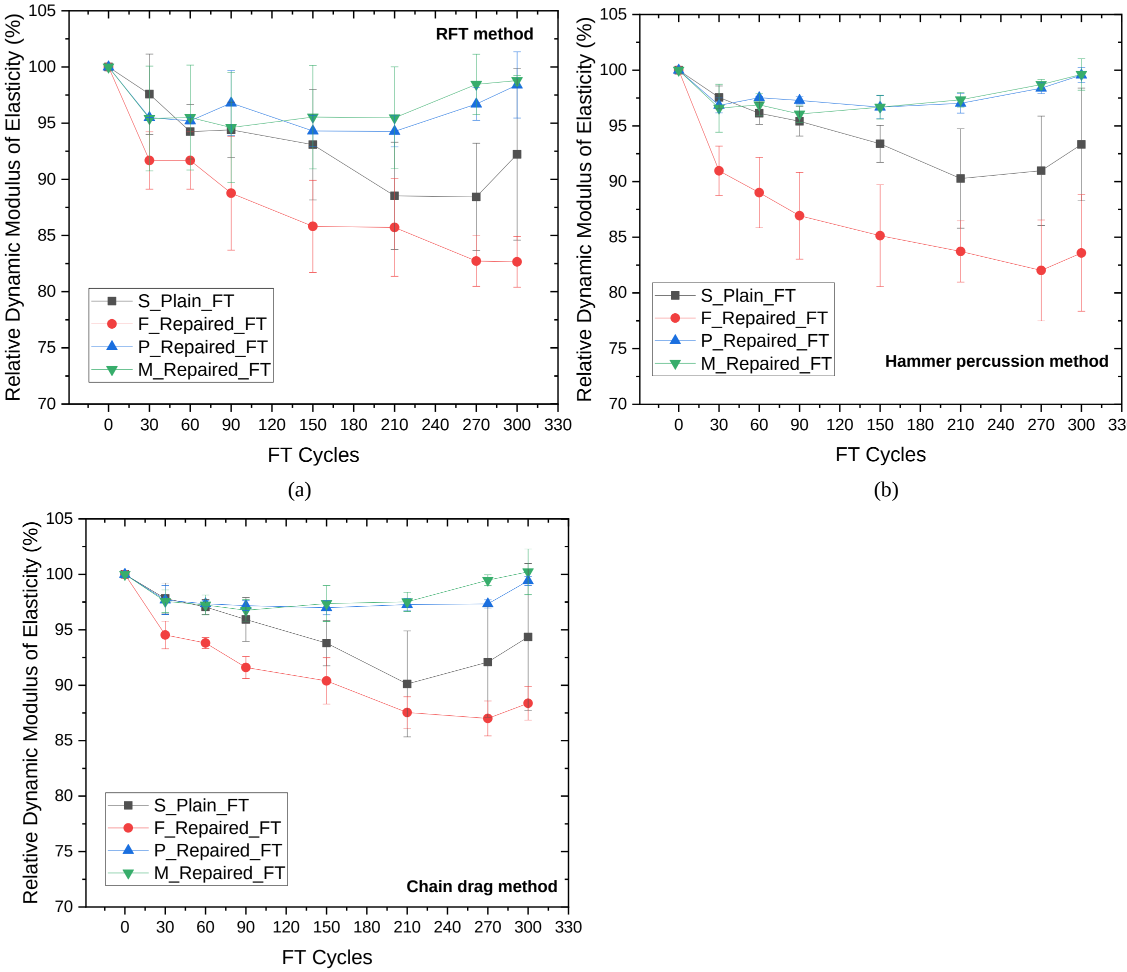

(a) (b)

(c)

Figure 24 (a) Transverse vibration using RFT method (b) Transverse vibration using hammer percussion method (c) Transverse vibration using modified chain-drag method

Fig. 24 (a) also shows that after 300 FT cycles, specimens repaired with Mix M had the smallest decrease in elastic modulus (4.5%), followed by Mix P (5.7%), Plain Mix S (11.6%), and Mix F (14.3%). The relative dynamic modulus of elasticity calculated of all mixes is higher than the threshold (60%) below which the test should be terminated, according to ASTM C666. To compare the variability in E_{dyn} measurement among different NDTs, the average coefficient of variation (COV) of all the mixes throughout the FT test is calculated. The average COV value of RFT method, hammer percussion method, and chain drag method is 4.09%, 3.54%, and 3.47%

respectively. This indicates that the scatter of E_{dyn} measurements using RFT method is slightly more than the other two methods.

It should be noted that concrete repaired with Mix M (cementitious repair mortar) and Mix P (polymer-modified cementitious mortar) can be more resilient to FT than the original intact prism (Plain Mix S). Similar results from using acoustic methods indicate that Mix M experienced the smallest drop in elastic modulus with a 2.7% drop for hammer percussion method. The lower drop in dynamic elastic modulus of Mix M and P indicates that fewer cracks were generated during FT exposure, which could result from the use of fibers and polymers. As mentioned previously, single polypropylene fiber in Mix P has a diameter and length of 36 microns and 6 mm respectively. We can see that the length and diameter of the fibers are fairly small, so the chances of fiber entanglement are lowered and therefore fibers can more effectively bridge the cracks. A similar phenomenon was observed by several researchers [13], [149]–[152] that the involvement of micro-polypropylene fiber increases FT resistance. Richardson [152] reported that micro-fibers can block capillary pores, which contributes to lower water absorption of fiber-reinforced concrete compared to plain concrete. Because concrete needs a high water content to experience FT damage, FT durability is improved due to reduced water absorption. Karahan and Atiş [149] attributed the FT resistance improvement to restrained expansion due to the addition of polypropylene fibers. During FT exposure, the volume of pore water can increase by 9% [13]. Due to the high tensile strength of PP fiber compared to concrete, the FT resistance is improved. However, in previous literature, contradictory findings are reported regarding whether the involvement of fibers could truly improve the FT resistance. Results of Allan and Kukacka [153] indicated that polypropylene fibers did not significantly or invariably alter freeze-thaw durability of tested specimens. In the authors' opinion, the contradictory findings reported in the literature could be due to the fiber's length and diameter. Regardless of the vast difference in mix design, the size of fibers can affect the pore microstructure of cement matrix to a great extent [154]. Fibers are usually not randomly distributed in concrete as assumed and suffer from issues of agglomeration especially when long fibers are used. Porous interfacial transition zone will form at the agglomerated fibers making it susceptible to FT damage. As shown in Table 3, the average hardened density of F, M, and P repaired samples are 2374 kg/m^3, 2325 kg/m^3, and 2289 kg/m^3, respectively. It should be noted that even though Mix P had the lowest density and strength compared to the other three mixes, it almost had the lowest drop in relative dynamic modulus of elasticity. Authors attributed this to the presence of fibers and lower air content in Mix P.

Cementitious repair concrete (Mix F) experienced the highest drop in elastic modulus among all three mixes. This result is consistent with the findings in the previous section where Mix F had the most severe surface scaling and highest mass loss after 300 cycles. Coarse aggregates in Mix F were observed to dislodge from the matrix after freeze-thaw exposure, which partly contributed to the loss in elastic modulus of the material.

ANOVA method was used to determine if there exists a statistically significant difference among the dynamic elastic moduli measured by three different NDT methods. The null hypothesis for ANOVA test is that dynamic elastic modulus values measured by three different NDT methods have no statistically significant difference. Fig. 25 summarizes the results of probability, P, that the null hypothesis is true. Considering a threshold of $P = 0.05$ (at a confidence level of 95%), comparisons where $P < 0.05$ means that the null hypothesis is rejected, and $P > 0.05$ means that the null hypothesis is not rejected.

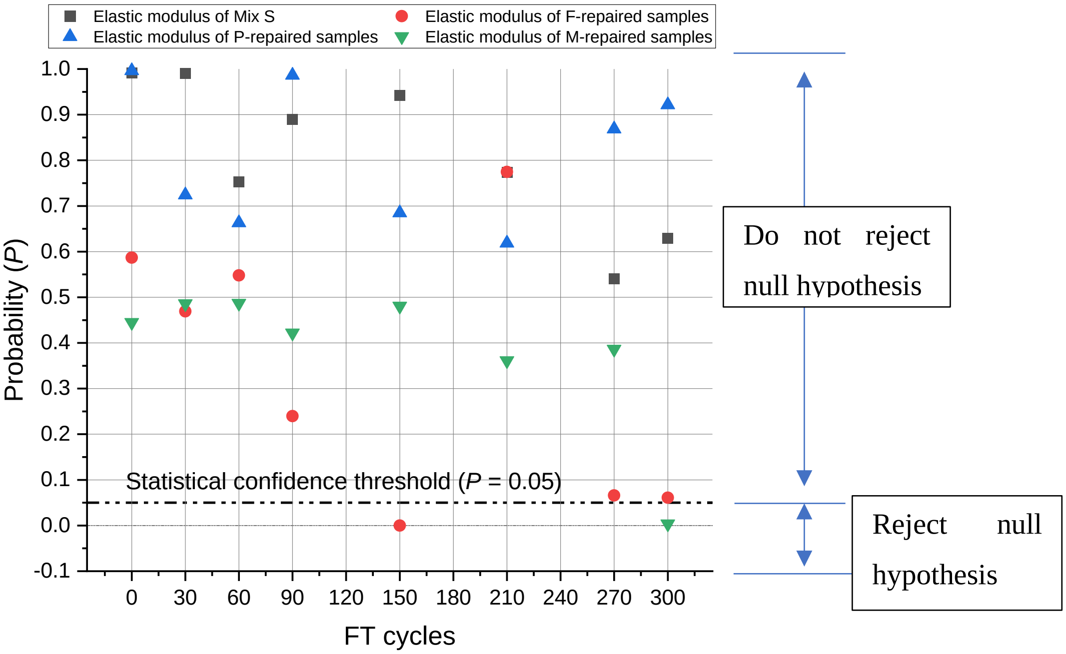

Figure 25 Probability P that the null hypothesis is true for each pair of different NDTs

In Fig. 25, P values higher than 0.05 threshold are observed for almost all mixes. It means that there is no statistically significant difference in using each of the three NDT methods to measure the dynamic modulus of elasticity (E_{dyn}) of different repaired samples. Based on this result, two important inferences can be drawn: 1) Due to no statistically significant difference between RFT and hammer percussion methods, we can infer that force and acoustic sensors can give close results in testing repaired concrete samples, and 2) Likewise, from hammer percussion and modified chain drag methods, we can infer that excitation methods (hammer and chain) are as effective in measuring the E_{dyn} of repaired beams. The first inference agrees with the findings of Huadong Wu and Siegel [155] who found that data from force and acoustic sensors could be used to validate one another. Sean and Gupta [124] also found that these two actuation methods have similar detectability for sub-surface delaminations in concrete slabs. In terms of the second inference, a previous study [124] has indicated that different contact stiffness and mass of the impact determines the contact time, which determines the excitation frequency. In the context of this study, the resonant frequency of the first mode for most of the repaired beams is around 2000 Hz. We can infer that the impact of a heavy-duty chain with a link diameter of 9.5mm and of a 56.7-gram steel ball hammer can generate at least 2000 Hz frequency in order to excite the specimens for free vibration.

Additionally, as seen in Fig. 25, as FT test progresses from 0 to 300 cycles, the probability $P >$ 0.05 holds true for most of the repaired samples. Therefore, the detectability using the 3 NDT methods for E_{dyn} measurements remains consistent with increasing FT cycles. However, E_{dyn} measurements using different NDTs are relevant in Mix F repaired samples at 150 FT cycles as P = 7.28×10^{-5}, and Mix M at 270 cycles as P = 0.0038. This can be considered test anomalies with the possible causes being experimental errors or due to materials properties that cause measurements taken by different methods to differ, which requires further investigation.

3.5.3 Bond Quality of the Repairs

3.5.3.1 Flexural Bond Test

The bond between repair materials and substrate concrete was determined by performing flexural strength test on repaired specimens. Fig. 26 shows the average flexural strength results of 3 specimens per mix without FT exposure and specimens of each mix after 300 cycles of FT exposure. It can be observed that all mixes experienced an increase in strength after 300 cycles of exposure. Mix S, F, P, and M had an increase of 6.15%, 5.43%, 24. 4%, and 41.9% in flexural strength, respectively. Authors hypothesize that this is most likely due to the continued cement hydration that compensated for any strength loss as a result of FT damage. Due to the time taken for the FT test and other NDTs, the flexural strength test on FT-damaged specimens was performed 4 months after testing specimens without FT damage. A similar phenomenon was reported by several researchers [146], [156] where dynamic elastic modulus even increased with increasing cycles of FT exposure. Zhou and Qiao [146] attributed the phenomenon to the ongoing cement hydration which outpaced the frost damage. Sun et al. [156] observed that the dynamic elastic modulus experienced a slight drop at the early stage after which the modulus values increased with increasing FT cycles. This is attributed to the decrease of pore size due to cement hydration that lowered the freezing point, which in turn enhanced the FT resistance of the materials.

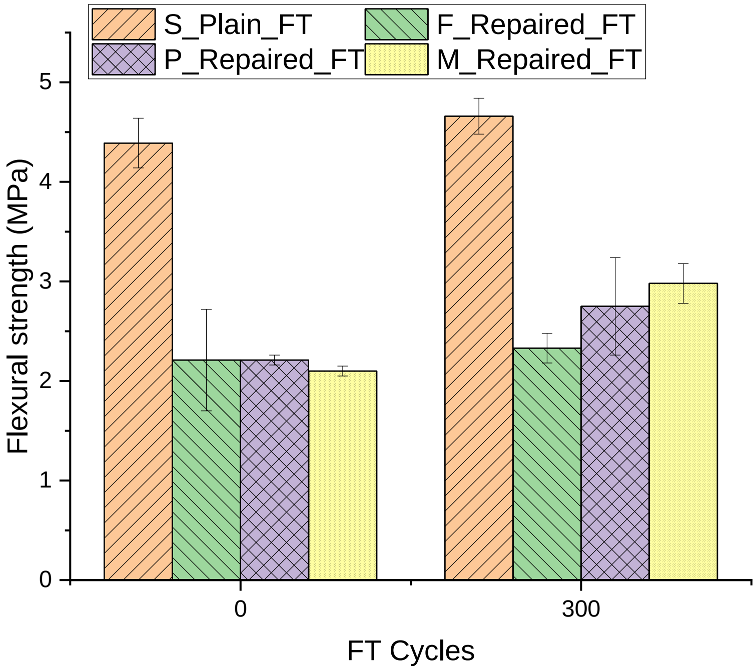

Figure 26 Flexural strength of repaired beams at 0 and 300 FT cycles

Additionally, the strength difference between specimens is pronounced after 300 cycles of FT exposure. In Fig. 26, at 0 cycles, no significant difference was observed between beams repaired by Mix F, P, and M. Compared to the results of control Mix S (4.39 MPa), the flexural strength of the repaired beams dropped almost 50%. After 300 cycles of FT exposure, the averaged flexural strength of Mix F, P, and M are 2.33 MPa, 2.75 MPa, and 2.98 MPa, respectively. The increased difference across different mixes is mostly due to the difference in material properties including FT resistance and chemical composition of the cementitious matrix. Mix P and M showed better bond flexural strength compared to Mix F, which conforms with the elastic modulus measurements and mass loss values.

Bond failure modes in repair materials can be classified into two categories including cohesion and adhesion failure. Cohesion failure refers to materials fracturing either in repair materials or substrate materials. Adhesion failure indicates that fracture occurs exactly at the substrate-repair interface. Fig. 27 shows the failure mode of repaired beams with and without FT damage. It can be observed that all repaired beams failed in adhesion modes, which means that the cold-jointed interface was not as strong as either the repair materials or the substrate. Past research showed that a cold-jointed interface could compromise structural integrity [157]. The reason behind this is that there is insufficient chemical bond between the new and old concrete. This also indicates that a rougher surface of the parent material may be required to increase interfacial adhesion/bond. Additionally, the difference in the elastic modulus between the substrate and repair materials could also contribute to adhesion failure. Previous literature [158], [159] studied the fracture behavior of concrete-concrete interface and found that the load-bearing capacity, fracture toughness, and critical energy release rate at the interface decreases with increasing difference in elastic moduli between the two materials. Fig. 28 shows the E_{dyn} values measured on 100 mm (Diameter) x 200 mm cylinders of plain Mix F, P, M, and S. These cylinders were cured in water at 23 ± 2°C and tested for E_{dyn} using RFT method following the ASTM C125 [140]. As shown in Fig. 28, a relatively constant difference in E_{dyn} can be observed between the substrate and repair materials, which could potentially weaken the interfacial bond during the specimen loading.

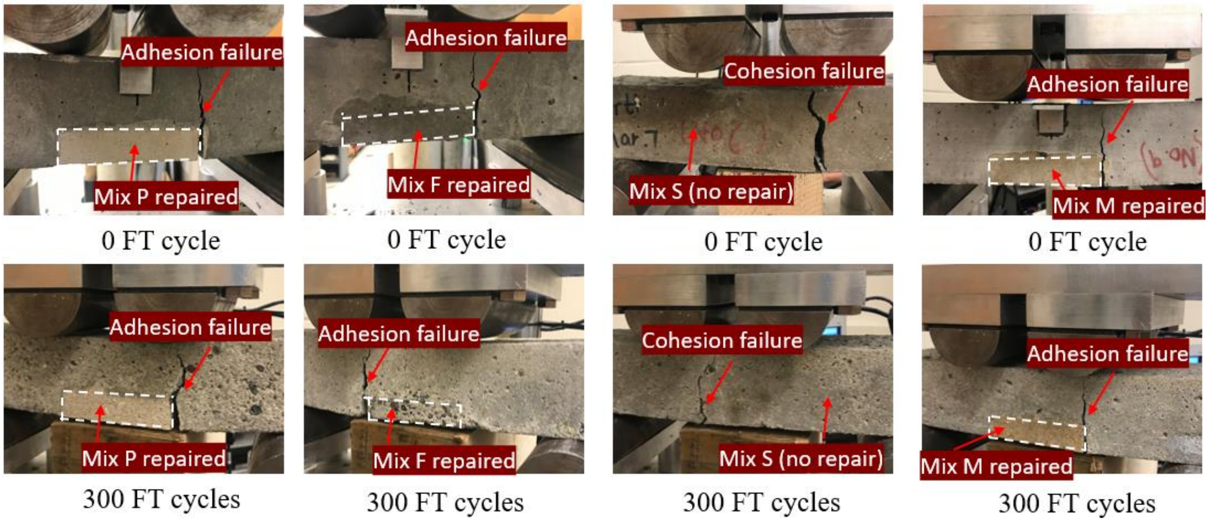

0 FT cycle 0 FT cycle 0 FT cycle 0 FT cycle

300 FT cycles 300 FT cycles 300 FT cycles 300 FT cycles

Figure 27 Bond failure modes of repaired beams before and after FT exposure

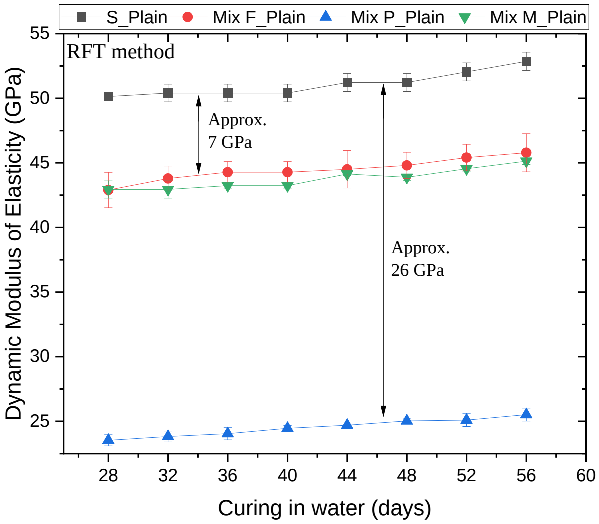

Figure 28 E_{dyn} measured from the transverse vibration of cylinders

3.5.3.2. Image analysis on interfacial cracks

Image analysis process

After the flexural strength test, the cracked specimens were placed under an optical microscope to examine the characteristics of interfacial cracks, as shown in Fig. 29. Image analysis results are useful because they reveal the interfacial bond characteristics at a microscopic scale and can be used to validate destructive and NDT test results. In this study, a trinocular stereo zoom microscope produced by Amscope© was used for the examination. Specifications of the microscope include 7X-45X continuous zoom magnification power with the super widefield optical system and a 4” working distance. Images captured by the optical camera were analyzed using ImageJ software. Fig. 30 shows the image analysis process for measuring crack width and tortuosity.

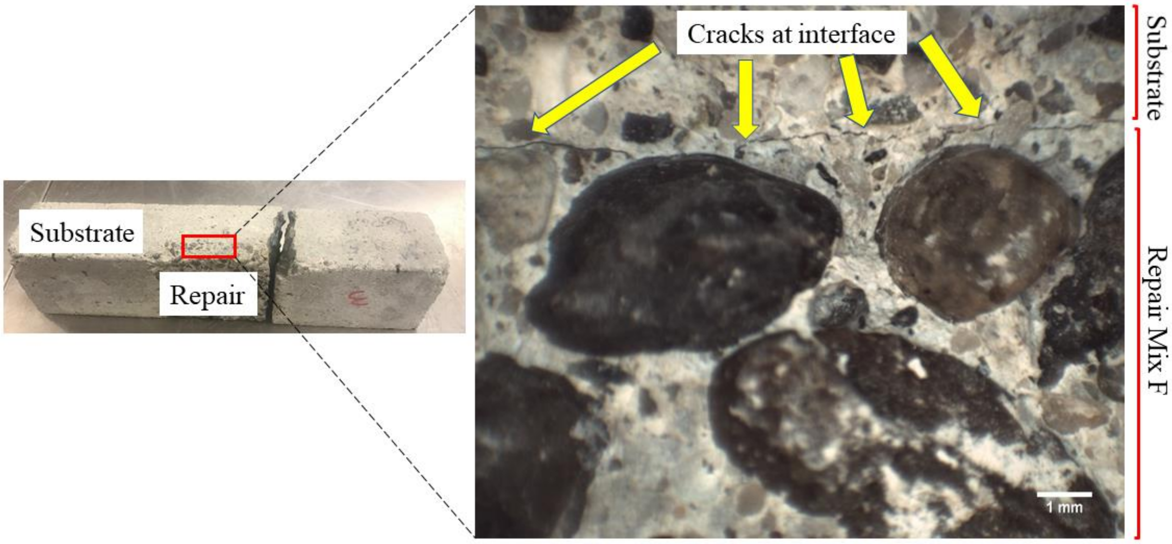

Figure 29 Horizontal interfacial cracks in Mix F after the flexural test

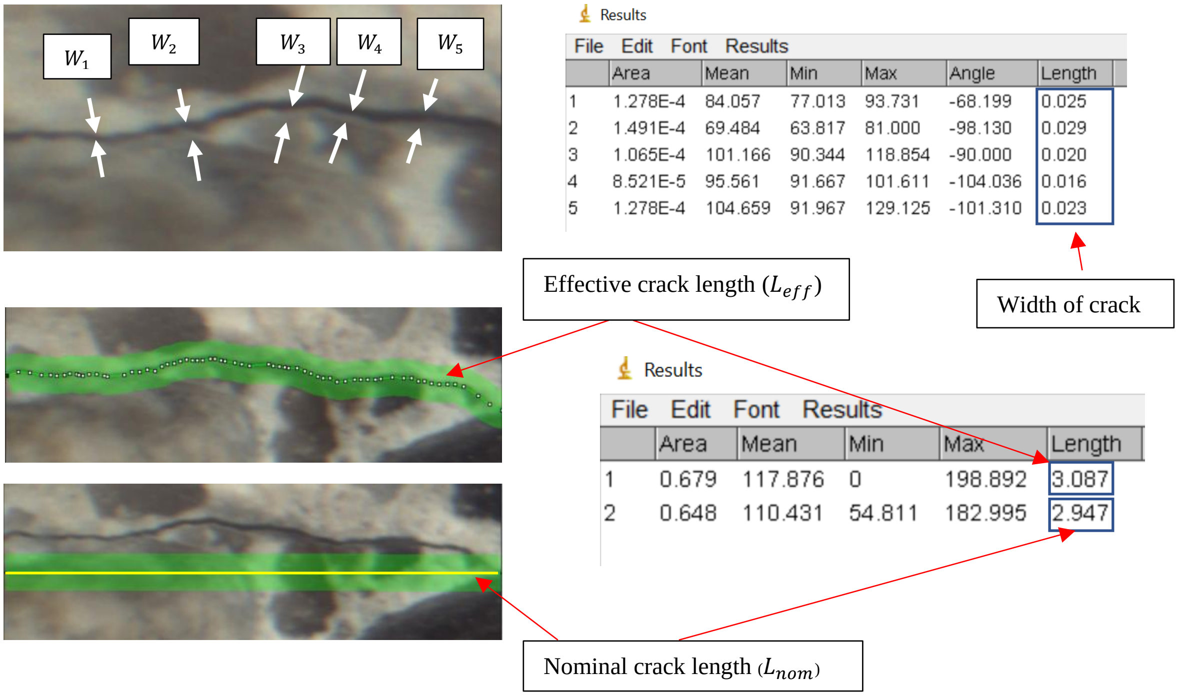

	Area	Mean	Min	Max	Angle	Length
1	1.278E-4	84.057	77.013	93.731	-68.199	0.025
2	1.491E-4	69.484	63.817	81.000	-98.130	0.029
3	1.065E-4	101.166	90.344	118.854	-90.000	0.020
4	8.521E-5	95.561	91.667	101.611	-104.036	0.016
5	1.278E-4	104.659	91.967	129.125	-101.310	0.023

	Area	Mean	Min	Max	Length
1	0.679	117.876	0	198.892	3.087
2	0.648	110.431	54.811	182.995	2.947

Figure 30 Image analysis using ImageJ software

Since the width of the crack varies along the repair-concrete interface, the average width of the crack was determined at five randomly picked locations along each crack. The interfacial crack profile is wavy, resulting in an effective crack length (L_{eff}) larger than the nominal crack length (L_{nom}), as demonstrated in Fig. 30. The nominal crack length is defined as the length of the line that is parallel to the substrate-repair interface connecting the head and tail of the interfacial crack. The tortuosity factor quantifies how tortuous a crack is. It is defined as the square of the ratio of the crack length to the straight-line distance between the starting and end points of the crack, as shown in Eq. 7 [160]:

$$\tau = (\frac{L_{nom}}{L_{eff}})^2 \tag{7}$$

where L_{nom} is the nominal crack length (straight) and L_{eff} is the effective (actual) crack length.

Image analysis results

Table 4 summarizes the interfacial crack width and tortuosity data of the repaired beams. Some specimens of Mix M and P did not have any interfacial cracks. The average crack width of three Mix F samples is 0.027 mm which is higher than that of any Mix M or P sample. This could be due to the lower bond strength of Mix F compared to Mix M and P. Accordingly, Mix F repaired beam is found to have the highest loss both in mass (6%) and dynamic elastic modulus (14.3%) after FT exposure. The average tortuosity of three Mix F samples is 0.68 which is close to the average values of Mix P (0.64). Issa et al. [161] found the crack tortuosity correlates well with fracture toughness or crack growth resistance. At the bi-material interface, a slight deviation of the failure plane from the bond plane was desired, as this is a toughening mechanism. As the mechanical interlocking at the interface increases, the fracture toughness increases. A good way to improve interface interlocking is to increase surface roughness [162]. In this study, all specimens are prepared to have a CSP value of 6, which results in a similar tortuosity factor.

Table 4 Characteristics of interfacial cracks

Mix	No.	Effective crack length (mm)	Width of crack (mm)		Nominal crack length (mm)	Tortuosity factor
			Avg.	S.D.		
F	1	3.087	0.0226	0.0049	2.947	0.911
	2	8.510	0.0480	0.0048	5.653	0.441
	3	4.238	0.0104	0.0015	3.516	0.688
M	1	No interfacial cracks observed				
	2	No interfacial cracks observed				
	3	1.848	0.0104	0.0015	1.663	0.810
P	1	3.329	0.0104	0.0015	2.802	0.708
	2	No interfacial cracks observed				
	3	5.175	0.0108	0.0018	3.947	0.581

3.5.4 Relationships Between Destructive and NDT Methods

Codes and standards, such as AS 3600-2009 [163], ACI 318-14 [164], and CSA A23.3-04 [165], have reported the relationship among compressive strength, modulus of elasticity, and modulus of rupture. Based on the empirical equations from these codes and standards, modulus of rupture of concrete is known to have a linear relationship with modulus of elasticity, as summarized in Table 5. Therefore, the relationship proposed in this study takes the form as shown in Eq. 8.

$$E_c = a \times (w_c^{1.5}) f_r' + b \tag{8}$$

Where a and b are variables that will be determined through least square fitting of experimental data, f_r' is the modulus of rupture value, and E_c is static modulus of elasticity, w_c is the density of the repaired specimen, which is computed by dividing mass by volume.

Table 5 Relationships between destructive and NDT methods proposed by codes and standards

Codes & standards	Model	Ref.
ACI 318-14	$E_c = 0.0694(w_c^{1.5}) \times f_r'$	[164]
CSA A23.3-04	$E_c = (\frac{w_c}{2300})^{1.5} \times (5500f_r' + 6900)$	[166]
AS 3600-2009	$E_c = 0.0717(w_c^{1.5}) \times f_r'$ when $f_c' \leq 40MPa$; $E_c = (w_c)^{1.5} \times (0.024f_r' + 0.12)$ when $f_c' > 40MPa$	[163]

Note: units of E_c and f_r' are GPa and MPa respectively.

To determine a correlation between destructive and non-destructive tests, results obtained from the same specimens were compared. All NDTs were completed first and then destructive tests were performed. Overall, nine regression curves were established between modulus of rupture (f_r') and modulus of elasticity measured by different NDTs. In addition, the coefficient of determination values was also calculated.

However, the relationships proposed by the codes and standards in Table 5 are based on static modulus of elasticity (E_c) whereas our study measured the dynamic modulus of elasticity (E_{dyn}). Due to the nonlinearity of concrete materials, E_{dyn} is a more reasonable estimate of the initial tangent modulus, while E_c is a close approximation of chord modulus. Many studies [167], [168] have found good linear relationships between static and dynamic elastic moduli. Zhou et al. [167] proposed the empirical equations correlating static with dynamic moduli of elasticity based on input parameters including volume content of aggregate and maximum size of coarse aggregates. In this study, the volume content of aggregate is approximately 0.797 and the maximum size of coarse aggregate is 19 mm, neglecting the effect of the repaired materials. Therefore, Eq. 9 is used to convert dynamic modulus of elasticity for all specimens.

$$E_c = 0.923E_{dyn} - 0.456 \tag{9}$$

Table 6 presents the empirical relationships established between destructive and NDT methods in this study. The units of E_c, f_r', and w_c shown in Table 6 are GPa, MPa, and kg/m^3 respectively. It is seen that the highest coefficient of determination between the results from destructive and non-destructive tests for Mix P, Mix M, and Mix F are 0.9292, 0.9476, 0.4721, respectively. Strong correlations can be found for all Mix P and M samples where all coefficient of determination values vary from 0.87 to 1. For the Mix F samples, the coefficient of determination value varies from 0.4 to 0.5. The lower coefficient of determination values could be due to the larger standard deviation of E_{dyn} of Mix F, as opposed to that of Mix M and Mix P. Hanjari et al. [169] linked the variation of E_{dyn} results to the level of frost damage. They found that both the compression test and elastic modulus test results scattered more for frost-damaged concrete than for the undamaged concrete. This agrees with the findings of this study as Mix F had a higher loss in mass and modulus of elasticity and had a lower modulus of rupture, compared to that of Mix M and Mix P. To address this issue, more test samples may be required in the future for Mix F to establish a better relationship between destructive and NDT methods.

Table 6 Relationships between the results from destructive and NDT methods

Method	Mix	Relationship	R^2
RFT method	P	$E_c = 0.03790(w_c)^{1.5} f_r' + 23.422$	0.9292
	M	$E_c = 0.02456(w_c)^{1.5} f_r' + 34.346$	0.9476
	F	$E_c = 0.02365(w_c)^{1.5} f_r' + 30.466$	0.4721
HP method	P	$E_c = 0.03275(w_c)^{1.5} f_r' + 24.702$	0.8773
	M	$E_c = 0.01532(w_c)^{1.5} f_r' + 38.562$	0.8956
	F	$E_c = 0.01552(w_c)^{1.5} f_r' + 33.680$	0.4331
Chain drag method	P	$E_c = 0.03174(w_c)^{1.5} f_r' + 25.083$	0.8904
	M	$E_c = 0.01380(w_c)^{1.5} f_r' + 39.517$	0.8703
	F	$E_c = 0.01220(w_c)^{1.5} f_r' + 35.824$	0.438

Note: The range of E_c: $30GPa < E_c < 45GPa$

As shown in Fig. 31, the values of static modulus of elasticity vs. modulus of rupture are plotted against values calculated from current codes and standards listed in Table 5. The function behind each regression curve is summarized in Table 6. In Table 5, the density value w_c is set to be the same as that of Mix S ($2530kg/m^3$) as codes and standards are intended to be used for concrete without repair. All density results are computed based on the weight of the samples at 0 FT cycles because the change in density throughout the FT test is minor and thus negligible.

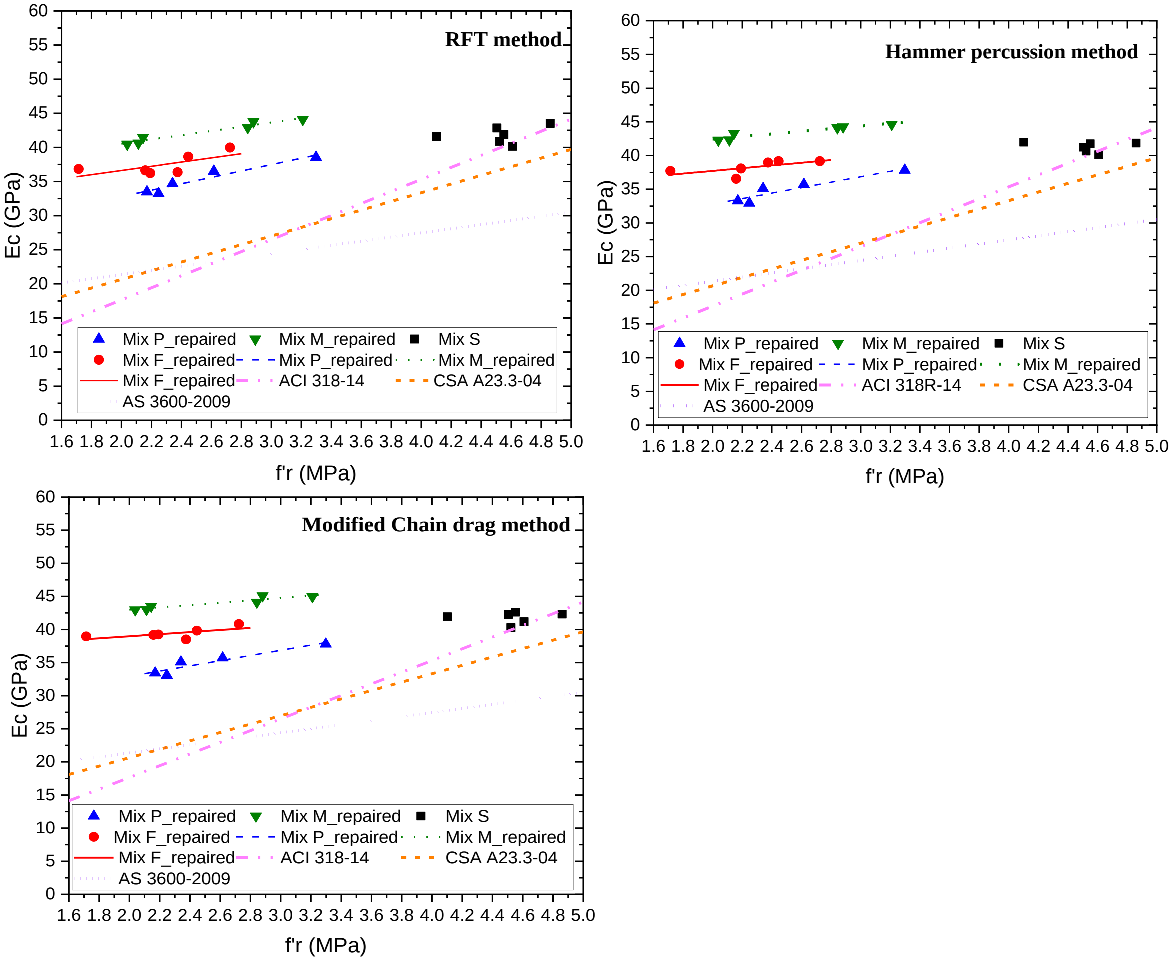

Figure 31 Comparison of experimental results based on RFT method and building code predictions

As shown in Fig. 31, it is observed that most of the data points of Mix S are situated closely to the prediction curve of ACI 318-14 regardless of the NDT methods used. This manifests the applicability of the three NDTs to estimate the structural capacity of FT-damaged samples. As for repaired specimens, all data points are located above the predicted curves of ACI 318-14, CSA A23.3-04, and AS 3600-2009. Based on the calculations, the modulus of rupture values of repaired beams in this study were approximately 50% lower than the calculated values as per ACI 318-14. This is due to the different failure modes between repaired samples and intact (control) samples. As shown in Fig. 31, the elastic moduli of repaired and intact samples center around 40 GPa, whereas the modulus of rupture of repaired and intact samples differ significantly. Therefore, the empirical equations in codes and standards that assume concrete failure in cohesion modes, may not be applicable for repaired samples. In other words, the use of NDTs to predict the load-bearing capacity of repaired samples may not be accurate unless prediction curves are modified. However, due to the limited number of data, the regression curves proposed in this study have upper and lower limits and should be used with care to predict modulus of rupture that lies within the specified ranges.

3.6 Conclusions

Based on the findings of this study, the following conclusions can be drawn:

1. RFT, hammer percussion, and modified chain drag can be used interchangeably to determine E_{dyn} of repaired specimens. Based on the results, it was established that RFT, hammer percussion, and modified chain drag lead to similar determinations of E_{dyn} regardless of the effect of FT exposure. This was confirmed by performing ANOVA on E_{dyn} measurements from different NDT methods.
2. This study confirms the applicability of RFT, hammer percussion, and modified chain drag for the detection of FT damage of repaired samples. The modulus of elasticity results determined from NDTs agree well with other observations including surface scaling, mass loss, and interfacial crack width. For example, cementitious concrete repair (Mix F), which has the highest loss (14.3%) in modulus of elasticity, shows the most severe surface scaling (rating 4-5), highest mass loss (6%), and largest average interfacial crack width (0.027 mm), among all mixes after 300 cycles of FT exposure.
3. The experimental results including E_c and f_r' of intact samples (Mix S) closely centered around the prediction curve of modulus of rupture in ACI 318-14. It manifests the applicability of using RFT, hammer percussion, and modified chain drag to predict the flexural capacity of intact specimens after FT exposure.
4. The samples repaired with polymer-modified cementitious mortar (Mix P) showed better FT resistance compared to other repaired samples. In this study, Mix P-repaired specimens showed the lowest mass loss (gained 0.8% mass), a low drop in relative E_{dyn} (5.7%, measured by RFT method), and a relatively small interfacial cracks width (maximum

0.0108 mm) after 300 FT cycles. Future research requires a more comprehensive study on the FT performance of various polymer-modified cementitious mortars of different mix design in repairing concrete structures.

5. The modulus of elasticity properties determined from the respective RFT, hammer percussion, and modified chain drag method has a strong linear correlation with the modulus of rupture values for Mix P and Mix M samples. The coefficient of determination values of regression curves of Mix M and P repaired samples ranged from 0.87 to 0.95.

Data Availability Statement: Some or all data, models, or code that support the findings of this study are available from the corresponding author upon reasonable request.

Funding: This work was supported by Natural Sciences and Engineering Research Council of Canada (NSERC) [grant number CRDPJ 533917-18].

Acknowledgements: Financial support of Natural Sciences and Engineering Research Council of Canada (NSERC) is greatly appreciated. Involvement and guidance of Terry Bergen and Peter Dias from Read Jones Christoffersen Ltd is also acknowledged. Assistance from technical staff Armando Tura and Geoff Burton is gratefully acknowledged. Assistance from co-op student Liam Sprangers in experimental work is greatly appreciated. Input from colleagues Maryam Monazami, Wenmeng Liu, and Qian Zhang is greatly appreciated.

Conflict of Interest: None.

Chapter 4 Performance of Repaired Concrete Under Cyclic Flexural Loading

Article Link: https://www.mdpi.com/1996-1944/14/6/1363

Boyu Wang[a], Rishi Gupta[b*]

[a] Graduate Student, Department of Civil Engineering, University of Victoria, 3800 Finnerty Road, Victoria, B.C., V8W 2Y2, CANADA; https://orcid.org/0000-0002-9983-7606

[b] Associate Professor, Department of Civil Engineering, University of Victoria, 3800 Finnerty Road, Victoria, B.C., V8W 2Y2, CANADA; https://orcid.org/0000-0002-3402-6095

* Corresponding author, Tel +1 (250)721-7033, email guptar@uvic.ca

Note: This chapter is adapted from the paper that has been published in Journal of Materials (MDPI), with permission where appropriate. This chapter highlights the use of a novel loading regime to characterize the mechanical response and service life of repaired concrete beams under cyclic loading performance. The resonant frequency method is used to determine the damage due to cyclic loading. The feasibility of using the Palmgren-Miner rule and Goodman linear model to estimate the fatigue life of repaired structures is confirmed within the context of this study.

4.1 Abstract

There is limited research reported on the effect of cyclic loading on cement-based repair materials as conducting such tests is time consuming. To overcome this issue, this study utilized a novel loading regime consisting of cycle groups with increasing stress amplitude to accelerate the test process. The Palmgren-Minder rule was used to estimate the fatigue life of repaired specimens. Specimens repaired with Mix M (cementitious repair mortar), which was estimated to have the highest 2-million-cycle fatigue endurance limit (77.4%), showed the longest fatigue life (95,991

cycles) during the cyclic loading test, the highest slant, and splitting bond strength among all repair mixes. The estimated two-million cycle fatigue endurance limit of Mix S (70.8%) was very similar to that was reported in literature (71%) using the traditional loading method. This study confirms the usefulness of Palmgren-Minder rule on estimating the fatigue life of repaired specimens. Also, the use of the novel loading regime showed the benefit of shortening the test process while producing results similar to those from using traditional loading methods. To improve the prediction accuracy, future research is required to modify the failure criteria to accommodate specimens that may not fail even when the average flexural strength is met.

4.2 Introduction

Concrete is widely used as a traditional building material in construction engineering, road engineering, and bridge engineering due to its low cost and excellent mechanical and durability performance [36]. However, due to external loading, environmental temperature changes, and ingress of aggressive substances, concrete can suffer from cracking and spalling, which substantially compromises the durability and safety of concrete structures [170]. It is a common practice to use repair materials to restore and extend the service life of concrete structures [2]. Most of the repair materials can be classified into three categories including polymer-modified cement-based materials, polymer materials, and cement-based materials [81]. Conventional Portland cement-based material is one of the most widely used materials for concrete repair [171], but has issues such as high drying shrinkage [172], permeability [172], and susceptibility to aggressive chemicals [84]. Polymer-modified cement repair materials, on the other hand, have advantages such as superior chemical resistance [108], low cure shrinkage [171], and good adhesion characteristics [173]. Some of the commonly used polymers include polyvinyl acetates, styrene butadine rubber, and polyvinyl dichlorides, which serve as a water reducing plasticizer that improves the workability while lowering the shrinkage.

In the recent decade, the fatigue behaviour of construction materials received great attention because natural or human activity-induced loads on buildings are often cyclic in essence [174]. When concrete is subjected to cyclic loading, there will be residual strain accumulating after each cycle, which indicates the internal progressive permanent structural change in concrete [175]. The fundamental mechanisms behind fatigue failure can be explained using stress concentration and fracture mechanics [176], and various approaches have been used by researchers to predict the concrete failure due to fatigue loading. One of the widely accepted approaches is based on empirically derived S-N diagrams, where S represents the load during cyclic loading and N means the number of cycles required to cause failure. Unlike most metals, concrete does not have a fatigue limit which means it will eventually fail after certain loading cycles. An example is that plain concrete subjected to repeated uniaxial tensile stresses appeared to fail before N reaches 2×10^6 cycles regardless of the stress level [177]. To quantify the fatigue damage of materials, different damage variables are introduced, and they are based on fracture mechanics [178]–[180], numerical approach [181], [182], or continuum damage mechanics [26], [183], [184]. The fracture mechanics method estimates fatigue crack propagation by measuring the stress intensity factor which indicates the stress state of the materials. However, the analysis of results can be quite cumbersome if the nonlinear mechanistic models are used [185]. Also, the complex detection equipment is indispensable for real-time monitoring of crack development [186]. The numerical approach involves using finite element method to simulate the crack growth of materials under fatigue loading [187]. The continuum damage mechanics considers the creation and growth of microcracks, which is discontinuous in its nature, to be continuous at a larger scale [188]. Damage leads to the change of materials properties such as elastic modulus, hardness, density, etc. Therefore, some commonly used variables that are chosen to quantify damage include elastic modulus, maximum strain, residual strain, energy dissipation, and ultrasonic pulse velocity [188]. The advantages of using fatigue damage variables based on continuum damage mechanics include: 1) easy measurement and application in engineering practice 2) distinct physical meaning 3) taking initial damage during fatigue loading into account. As a result, this study employs the method of continuum damage mechanics to derive S-N diagrams and estimate the fatigue life of materials under fatigue loading. In 1945, Miner [189] introduced the concept of damage accumulation in a simple form. This rule assumes linear accumulation of fatigue damage with the increasing number of cyclic loads. Over the years, efforts have been made to formulate this rule involving more factors such as fatigue loading history [27], stress ratio [28], thermodynamics potential [29], and fatigue inelastic parameters [26]. The modified Palmgren-Miner's rules have improved accuracy in predicting fatigue life, but face challenges in being widely used in current building codes due to their complex forms [30].

In the case of repaired structures, it is important to ensure sufficient fatigue life for the bond between the parent concrete and repair materials. Shah et al. [190] studied the fracture behavior at a concrete-concrete interface under fatigue loading conditions. It was found that the fatigue life of intact specimens was the highest and decreased with increasing differences between the elastic moduli of materials on either side of the interface. Shah et al. [158], [191] reported similar findings that the mismatch in elastic modulus and in compressive strength between the parent and repair materials increases the vulnerability to cracking when a patch repair system is under quasi-static loading conditions. Ong et al. [192] investigated the fatigue behavior of concrete beams repaired with steel-fiber cement-based mortars. They found that repair concrete beams survived 100,000 load cycles without any delamination and significant loss in stiffness if the maximum amplitude of cyclic loading was below 45% of ultimate static strength. Some researchers [193], [194] investigated the steel-reinforced concrete beams retrofitted with ultra-high performance concrete. They used epoxy-based adhesives to bond repair concrete plates with the substrate concrete and tested them under fatigue loading. It was found that the fatigue life of repaired beams was longer than the control (intact) beam [193].

In summary, most of the aforementioned literature focused on the bond strength of cement-based repair concrete under fatigue loading, but scarce work studied other types of repair such as polymer-modified cementitious mortar, which outperform cement-based concrete repair in many aspects [104]–[106], [108]. Also, apart from the exhaustive studies [26]–[31] that used Palmgren-Miner’s rule and its modified forms on concrete materials, there are insufficient studies about the applicability of Palmgren-Miner’s rule on predicting the fatigue life of repaired structures. In this study, authors aim to determine the applicability of Palmgren-Miner’s rule to estimate the fatigue life of repaired concrete structures. Since cyclic loading is time-consuming, a modified loading regime consisting of cycle groups of increasing cyclic stress amplitude is used to accelerate the test process. A method based on fatigue stress to flexural strength ratios is also proposed to derive the S-N curve. The estimated fatigue life in this study is compared with the results in previous literature to determine its liability. Additionally, the failure mode, hysteretic behavior, and dynamic elastic modulus drop of repaired samples after cyclic loading are analyzed and discussed, which is used to validate the predicted S-N curves. The findings of this study not only provide information on how to conduct a rapid and easy estimation of the fatigue life of repaired structures but explore the fatigue resilience performance of various repair materials.

4.3 Materials and Methods

A total of 4 mixes were prepared including one control mix developed in the lab and three commercial repair products locally available in the market. The control mix for the substrate, named Mix S, received the repair and had a design compressive strength of 50 MPa. The rationale for using 50 MPa concrete as the substrate was to minimize its own degradation (prior to that of the applied repair material) due to external loadings such that the fatigue resilience performance of different repair materials could be determined. Also, the use of Mix S as the substrate is the same as a previous study by authors [195] and its use provides for better research continuity. Table 7 summarizes the mix design details of Mix S, and the gradation information of aggregates is shown in Fig. 32. Based on the gradation curves, the fineness moduli of coarse and fine aggregates were calculated to be 6.48 and 2.85 as per ASTM C136 [126]. The water to material ratio (w/m) for Mix S, F, P, M were 0.067, 0.1, 0.18, and 0.09 respectively. In this study, cementitious repair mortar (Mix M), cementitious repair concrete (Mix F), and polymer-modified cementitious mortar (Mix P) are used. These three types cover most of the commercial repair products on the market and thus are representative. To have sufficient workability, 2.37 kg, 4.26 kg, and 2.5 kg of water were added to Mix M, Mix P, and Mix F per bag respectively as recommended by the material manufacturers. The slump of Mix S was adjusted to 60 mm which meets the range stipulated by ACI 211.1 [125]. Manufactures provided the setting time information which is shown in Table 8. The fresh properties of the repair and control mixes include air content and slump which are measured following ASTM C231 [131] and ASTM C 143 [130] respectively. The hardened properties include compressive strength (f_c') and density at 28 days which were determined following ASTM C39 [132]. All this information can be found in Table 8. More information about the properties such as freeze-thaw and corrosion resistance performance of the repair materials can be found in Wang et al. [133], [134], [195] and Bajaj et al. [129].

Table 7 Mix design details of the parent material ($\boldsymbol{kg/m^3}$) (data from [195])

Name	Fine aggregate	Coarse aggregate	Cement	Superplasticizer	Air-entraining agent	Water
Mix S	762	1053	450	2.25	2.25	153.7

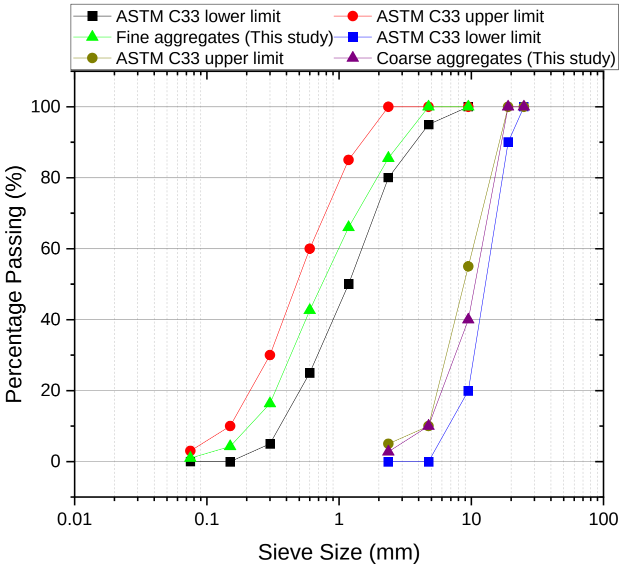

Figure 32 Gradation curves of aggregates used in this study (Redrawn from [195])

Table 8 Details of fresh and hardened properties of substrate and repair materials (data from [195])

Material Type	Hardened properties		Fresh properties			
	Density (kg/m^3)	f_c' after 28-day curing (MPa)	Slump (mm)	Time to set (min)	w/m	Air content percentage (%)
Repair Mix M	2325	68 ± 2.4	70	75	0.09	5.0
Repair Mix F	2374	55 ± 2.2	80	-	0.1	5.1
Repair Mix P	2289	39.5 ± 1.3	15	9	0.18	7
Parent Mix S	2530	59.4 ± 1.4	60	90	0.067	4.9

4.3.1 Specimens

4.3.1.1 Prisms

In field applications, a common practice to rehabilitate structures is to remove delaminated concrete, clean the parent substrate and rebars, and apply the repair materials. In order to simulate in-situ damaged structures, prismatic beams with an induced cut on the tension side were prepared. Notched beams were prepared using Mix S and received the repair materials (Mix M, F, and P). All specimens were cast with a dimension of 75 x 100 x 400 mm, as shown in Fig. 33. For comparison purposes, specimens made of Mix S with no cut were prepared as well. Additionally, the material supplier of Mix F specifies the minimum depth of repair to be 25 mm which is the upper limit prescribed by the supplier of Mix M. Given these constraints, all specimens in this study have a repair depth of 25 mm. The shape of the repair is selected to be square (100 x 100 mm) in order to prevent problems such as feather edge. Experience has shown that repair areas with feather (very thin) edges usually fail quickly.

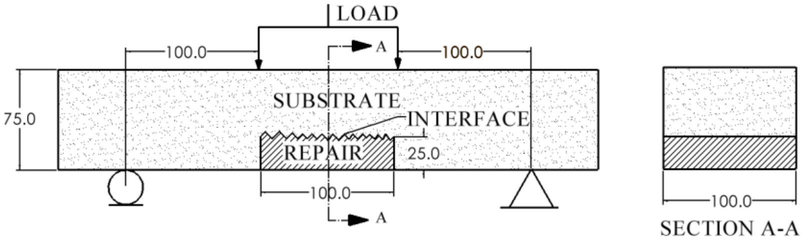

Figure 33 Prismatic specimens under four-point loading (all dimensions are in mm)

Prior to the application of the repair, surface roughening is an important step to ensure a good bond. Typically, quantifying the roughness of a concrete surface is mainly through comparing the target surface with nine standard concrete surface profile chips. These chips were proposed by International Concrete Repair Institute (ICRI) [136]. In this study, surface profile chip #6 was selected as the target surface profile on the surface receiving repair on the substrate as shown in Fig. 34(a). This was recommended as per the ICRI Technical Guideline No. 310R-2013 [136]. In order to achieve a good consistency between specimens in terms of surface roughness, an innovative plastic block with certain surface roughness was conceived and designed by the authors. As shown in Fig. 34(a), the block was made by 3D printing on a plastic base following a model that is produced by 3D scanning the #6 surface profile. A high-resolution 3D printer named Ultimaker 3 was used to print the inserted blocks. This 3D printer has up to 20 micro resolution which ensures printing objects with high accuracy.

The block was introduced into the mold before concrete placement. Fig. 34(b) shows the 3D printed block placed at the bottom of the mold. Concrete was placed into the molds and placed on a vibrating table for a ten-second consolidation. Specimens were cured in ambient conditions at 18±2℃ for 24 hours before the inserted blocks were removed. Three types of repair materials (Mix M, F, and P) were applied to the cavity. Another 24 hours later, all specimens were demolded and transferred to the water bath for water curing. The range of water curing temperature was 23±2℃. Prior to testing, all specimens were cured in water for 28 days.

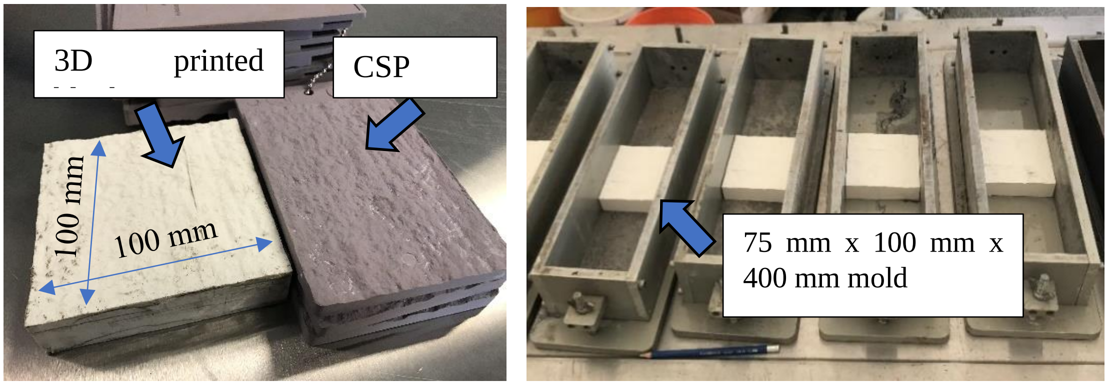

(a) (b)

Figure 34 Mold preparations (a) 3D printed block and #6 CSP chip (b) 3D printed blocks in molds

4.3.1.2 Cylinders

Cylindrical specimens were prepared for splitting tensile and slant shear bond tests. The dimension of the prepared specimens is illustrated in Fig. 35. Cylinders of dimensions $100 \times 200\ mm$ and $75\ \times 150\ mm$ were first cast and cured in water for over 28 days at 23±2°C before receiving the repair. The $75\ \times 150\ mm$ cylinders were saw cut at an angle of $30°$ for slant shear test following ASTM C882 [113]. The $100 \times 200\ mm$ cylinders were saw cut along diametrical lines for splitting tensile test. They were then repaired with Mix F, M, and P, and kept in water at 23±2°C for 14 and 28 days before the bond tests were performed. Note that no surface treatment, such as surface roughening, was done on the cylinder. The purpose is to simulate the worst bonding condition.

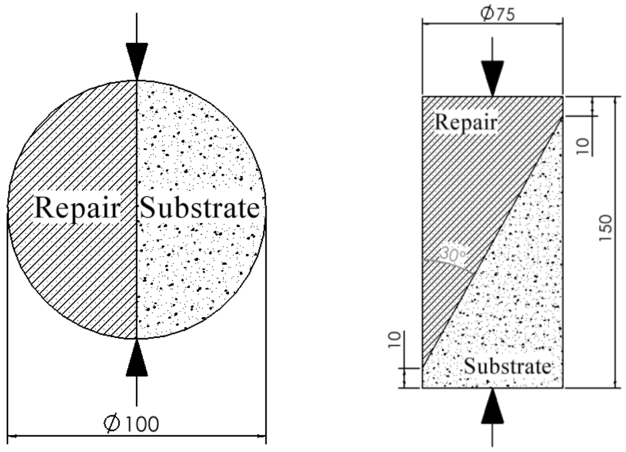

(a) (b)

Figure 35 Bond test sketches (a) Splitting tensile test (b) Slant shear test (all dimensions in mm)

4.3.2 Flexural Strength & Cyclic Loading Test

A third-point loading test was conducted to determine the static flexural strength of the repaired prisms as per ASTM C78 [42]. An MTS 810 machine with 250 kN load capacity was used to load the specimens. A total of 3 specimens for each mix were tested and the modulus of rupture was calculated using Eq. 10. The specimens were loaded with the repair materials on the tension side. According to ASTM C78, the loading rate was set as 2323 N/min such that the maximum stress on the tension surface is 1.2 MPa/min. The loading setup is shown in Fig. 36.

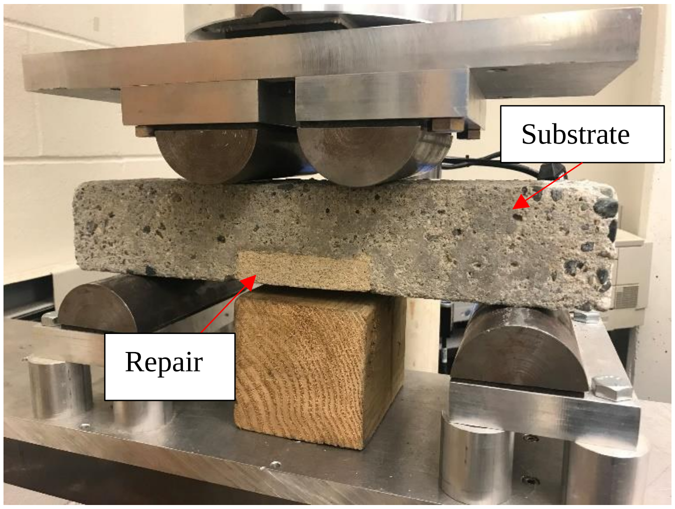

Figure 36 Test setup for cyclic loading

$$\sigma_u = \frac{PL}{bd^2} \tag{10}$$

where σ_u is the ultimate stress of the material, P is the maximum applied load indicated by the test machine, L is the span length, b is the average width of specimen, and d is the average depth of specimen.

Following the flexural strength test, a series of specimens were exposed to flexural cyclic loading, and the test setup was the same as shown in Fig. 36. Conventional cyclic loading may consume a large amount of time and have risks of failing the specimens in the first few cycles especially when the applied stress is close to the ultimate strength. In order to overcome these problems, all specimens in this work were subjected to cycle groups of increasing amplitude, and a new approach was used to obtain the S-N curve for repaired specimens. In this study, the load variation was sinusoidal with a frequency of 10 Hz. Different loading force groups were used on intact and repaired beams as they had different flexural strength. Table 9 and Fig. 37 show the details of loading protocols adopted in this study. According to ACI 215R-74 [196], when a structure is under fatigue stress, the minimum stress is due to the dead load while the maximum stress is due to the dead plus live load. The dead load for structures before and after the repair should remain the same, so the minimum stress applied on the samples in this study is the same. The load bearing capacity of the structure after the repair could be different than that of the intact structure. As a result, the maximum stress applied on the samples is different. In this study, beam repaired with different repair materials showed similar load bearing capacity under flexural loading, so the maximum cyclic load for all repaired samples is the same.

The moduli of rupture of repaired beams with different mixes were first determined, which provides the benchmark for setting cyclic loading parameters. In the case of intact beams (Mix S) that was cured for 28 days, the first 10,000 cycles exert a maximum force of 4235 N, which corresponds to 55% of the averaged modulus of rupture of Mix S. The minimum cyclic force was set as 800N for all the specimens. If the specimen has not failed after the first cycle group, the maximum cyclic load will increase to 5005 N, which corresponds to 65% of the averaged modulus of rupture value. The loading forces increase at an interval, which corresponds to approximately 10% of the modulus of rupture value. The cyclic test continues until the resulting stress reaches the average modulus of rupture value or until the specimen fails, whichever happens first. Some specimens may not fail even when the maximum cyclic load has reached 100% of the average ultimate load. In this case, the cyclic test continues with increased cyclic loading force (200 N above the average ultimate load) and loads the specimen for another 10,000 cycles. The loading force keeps increasing until the specimen breaks. The number of cycles at failure is recorded.

Table 9 Loading force groups for different samples

Percent of ultimate load (%)	Mix S		Mix F		Mix M		Mix P	
	Max.	Min.	Max.	Min.	Max.	Min.	Max.	Min.
55	4235	800	2090	800	2090	800	2090	800
65	5005	800	2470	800	2470	800	2470	800
75	5775	800	2850	800	2850	800	2850	800
85	6545	800	3230	800	3230	800	3230	800
95	7315	800	3610	800	3610	800	3610	800
100	7700	800	3800	800	3800	800	3800	800

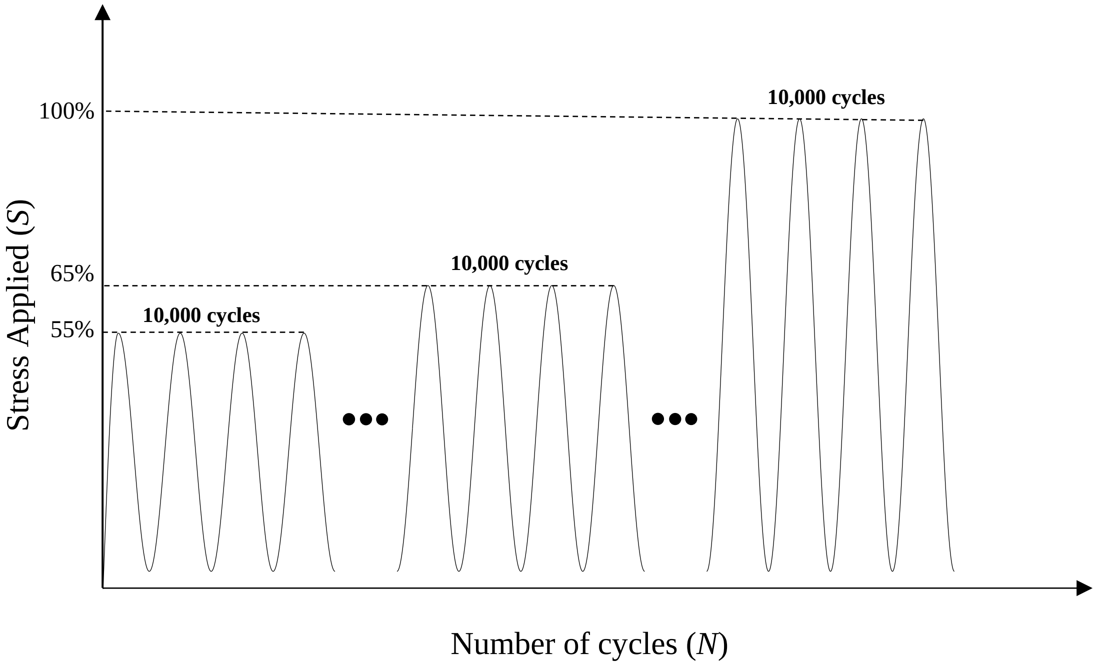

Figure 37 Cyclic Loading Regime

In this study, the use of cycle groups to obtain an S-N curve was adopted from the work of Nieto et al. [32]. Different than [32], this study used cycle groups to test repaired concrete beams. The determination of S-N curve was based on the assumption that the curve can be approximated by a straight line in a logarithmic scale, as shown in Eq. 11. By means of Palmgren-Miner rule and Goodman linear model [32], Eq. 11 can be further derived into Eq. 12, which can be used to calculate the straight line slope b in Eq. 11. As demonstrated in Eq. 12, the accumulative damage factor D_i will reach 100% when the specimen fails.

$$S = \sigma_u N^b \tag{11}$$

where N is the number of cycles to failure, S is the stress applied on the specimen, and b is the slope of the straight line.

$$D_i = \sum_{i=1}^{i=k} n_i \left(\frac{\sigma_u - \sigma_i^m}{\sigma_i^a}\right)^{1/b} \tag{12}$$

where D_i is the accumulative damage factor expressed in percentages, n_i is the number of cycles applied at *i*th cycle group, σ_i^m indicates the mean stress value at *i*th cycle group, and σ_i^a is the alternating stress value at *i*th cycle group.

4.3.3 Non-destructive Test (NDT) Method

The Resonant frequency test was performed when each cycle group is completed to determine the changes in dynamic modulus of elasticity (E_{dyn}). According to ASTM C215 [41], the resonant frequency and E_{dyn} can be determined using an accelerometer. In this study, the resonant frequency tester consisted of a PCB Piezotronics 353B15 accelerometer and a data acquisition system manufactured by Olson Instruments. The transverse resonant frequency of the 1st mode was used to calculate E_{dyn}. The specimens were first placed on a foam piece to allow for free vibration. An accelerometer was then attached to the end of the specimen through an adhesive grease. A hammer was used to strike the middle of the specimen, and the vibration signal was captured by the accelerometer. The test setup is shown in Fig. 38.

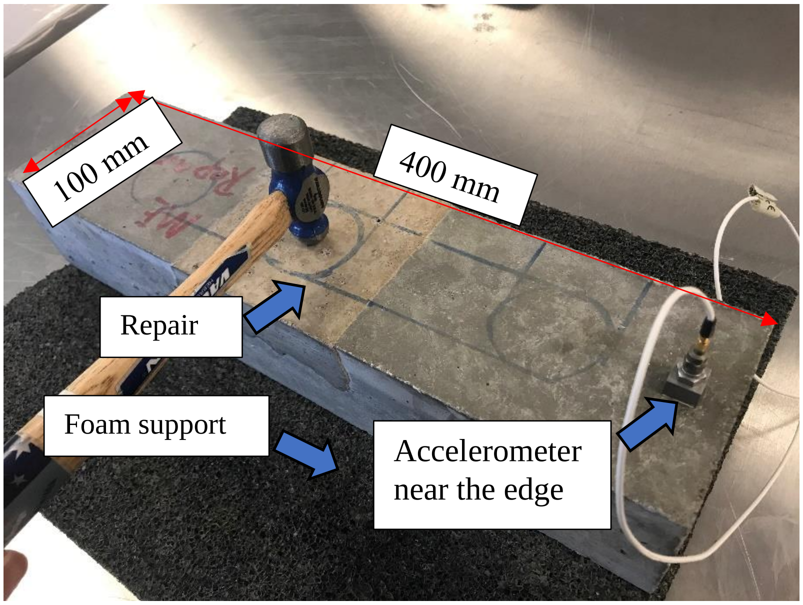

Figure 38 Resonant frequency test setup

4.3.4 Bond Test Methods

The interfacial tensile and shear bond strength between substrate concrete (Mix S) and repair materials are determined using methods shown in Figs. 35 (a) and 35 (b). The splitting tensile test follows the standard procedures stipulated by ASTM C496 [197]. This test applies a diametral compressive force along the concrete-repair interface at a rate of 0.5 kN/s, and the peak load at failure was recorded. Eq. 13 is used to calculate splitting tensile bond strength (σ_t).

$$\sigma_t = \frac{2P}{\pi LD} \tag{13}$$

where P is the load at failure, L and D are cylinder length and diameter.

The slant shear test was performed following ASTM C882 [113]. The specimen was loaded at a rate of 1.1 kN/s until failure as shown in Fig. 35(b). Eq. 14 is used to calculate slant shear bond strength (τ).

$$\tau = \frac{1}{2}\sigma_0 \sin 2\alpha \tag{14}$$

where τ is slant shear bond strength, σ_0 is the vertical stress applied at the cylinder edge, α is the bond plane inclination angle which is 30° in this study. FORNEY compression testing machine (model:F-650), which has a load capacity of 2891 kN, was used for this test.

4.4 Results and Discussions

4.4.1 Bond Strength

The life cycle of the repaired beams under cyclic load is affected by the bond strength of the repair materials [198]. In this study, the shear and tensile bond strength of three repair materials are determined, and the average results of three specimens from each mix are shown in Fig. 39. Among all repair mixes, Mix M (cementitious repair mortar) shows the best bond performance with an average slant shear bond strength of 12.3 MPa and 16.7 MPa and tensile bond strength of 1.4 MPa and 2.3 MPa at 14 and 28 days of curing, respectively. Past research reported that the slant shear bond strength of different repair materials ranged from 5 MPa to 70 MPa [111], [199]–[202], and the splitting tensile strength ranged from 0.5MPa to 5MPa [200]–[204]. The large deviation in bond test results could be due to many reasons [205]. The factors that affect bond strength include surface roughness, cleanliness, soundness [206], chemical adhesion and cohesion [207], mix design, and curing regimes of the repair materials [208]. Some recent research [200], [209] reported that the bond strength of ultra-high-performance concrete (UHPC) used as repair materials is excellent. The main reason is the dense interfacial transition zone between UHPC and the substrate as UHPC has a very low water-to-cement ratio [58]. Also, the absence of coarse aggregate in UHPC contributes to better compaction during concrete placement. In this study, Mix M (cementitious repair mortar) possesses the highest strength which potentially results in a better bond compared to other repair mixes. Also, since the repaired samples in this study have the same roughness (because of the identical 3D printed blocks used for surface preparation) and curing regimes, the dominant factor is attributed to the mix design. Past research has shown that the involvement of fibers [210], [211] and polymers in the mix [212] is beneficial in improving the adhesion strength of the repair materials. In this study, the polymer-modified cementitious mortar (Mix P) contains polypropylene fibers with an approximate dosage of 0.2% by weight of all the constituents in the mix. Though the compressive strength of Mix P is 10 MPa less than Mix F (cementitious repair concrete), Mix P exhibited similar slant and tensile bond strength compared to Mix F (considering their error bars are mostly overlapped for both 14-day and 28-day results). In Fig. 39 (b), mix M and P samples have relatively large variations compared to mix F samples. This could be attributed to the bond test method used in this study. This is supported by the past literature [109], [111] that has shown that the scatter of bond test results using various test methods could be large. It is observed that some specimens of Mix M and P samples experienced slight crumbling along with adhesion failure during the bond test, which could result in variations of bond test results. Additionally, in a study by Feng et al. [201], the scatter in bond test results varies with different mixture designs.

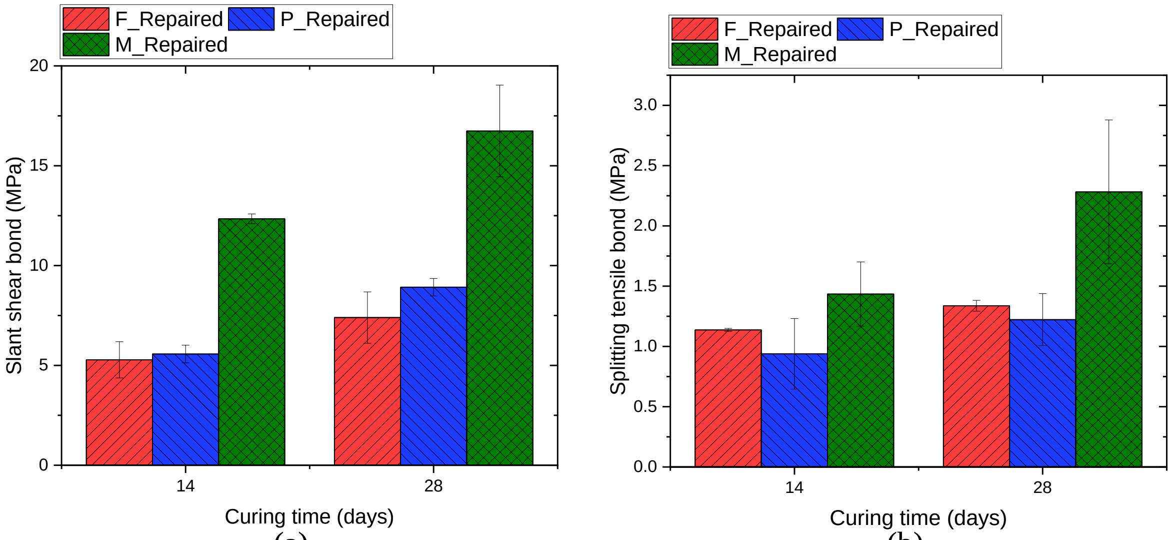

(a) (b)

Figure 39 Bond stresses at failure for different repair materials (a) slant shear bond (b) Splitting tensile bond

The failure mode can be classified into two types, adhesive failure and cohesive failure. Cohesion failure occurs when either the substrate concrete or repair material fails. When the substrate concrete fails, some substrate materials will be left on the half cylinder of repair materials. Adhesion failure occurs when fracture is at the exact concrete-repair interface leaving a clean and smooth failure interface. Fig. 40 shows an example of failure pattern of bond tests. We can observe that all repaired specimens had adhesion failure.

(a) (b)

Figure 40 Failure patterns of bond test (a) Splitting tensile test (b) Slant shear test

4.4.2 Hysteretic Force-displacement Response

To simulate in-situ repaired structures, prismatic beams with a square patch on the tension side were prepared and tested under cyclic load. To accelerate the test process, a modified loading regime consisting of cycle groups of increasing cyclic stress amplitude is used. The hysteretic force-displacement response of each specimen after each load cycle is recorded, which reflects the damage accumulation and energy absorption capability of the samples [213]. Fig. 41 shows the hysteretic curves of representative specimens. Only the results at every 10,000 cycles were plotted for better clarity and readability. A shift in load-displacement curve with increasing number of cycles can be observed for all repair mixes. This shift indicates the permanent deformation after loading cycles, denoted as δ. Table 10 shows the permanent deformation accumulated between the first cycle and failure. Mix F, M, P and S has a δ value of 0.18 mm, 0.22 mm, 0.11 mm, and 0.24 mm, respectively. Disregarding the intact specimens (Mix S), Mix M (cementitious repair mortar) had the highest permanent deformation before failure among all repaired specimens. High inelastic deformation can help delay local failure by redistributing redundant stress in the critical section of a structure and is thus beneficial [214]. Note that Mix M also has the highest fatigue life (N_f) as shown in Table 10. The superior performance of Mix M repaired specimens to resist cyclic loading could be due to the mechanical characteristics of Mix M. Mix M has an average compressive strength of 68 MPa which is the highest among all the mixes.

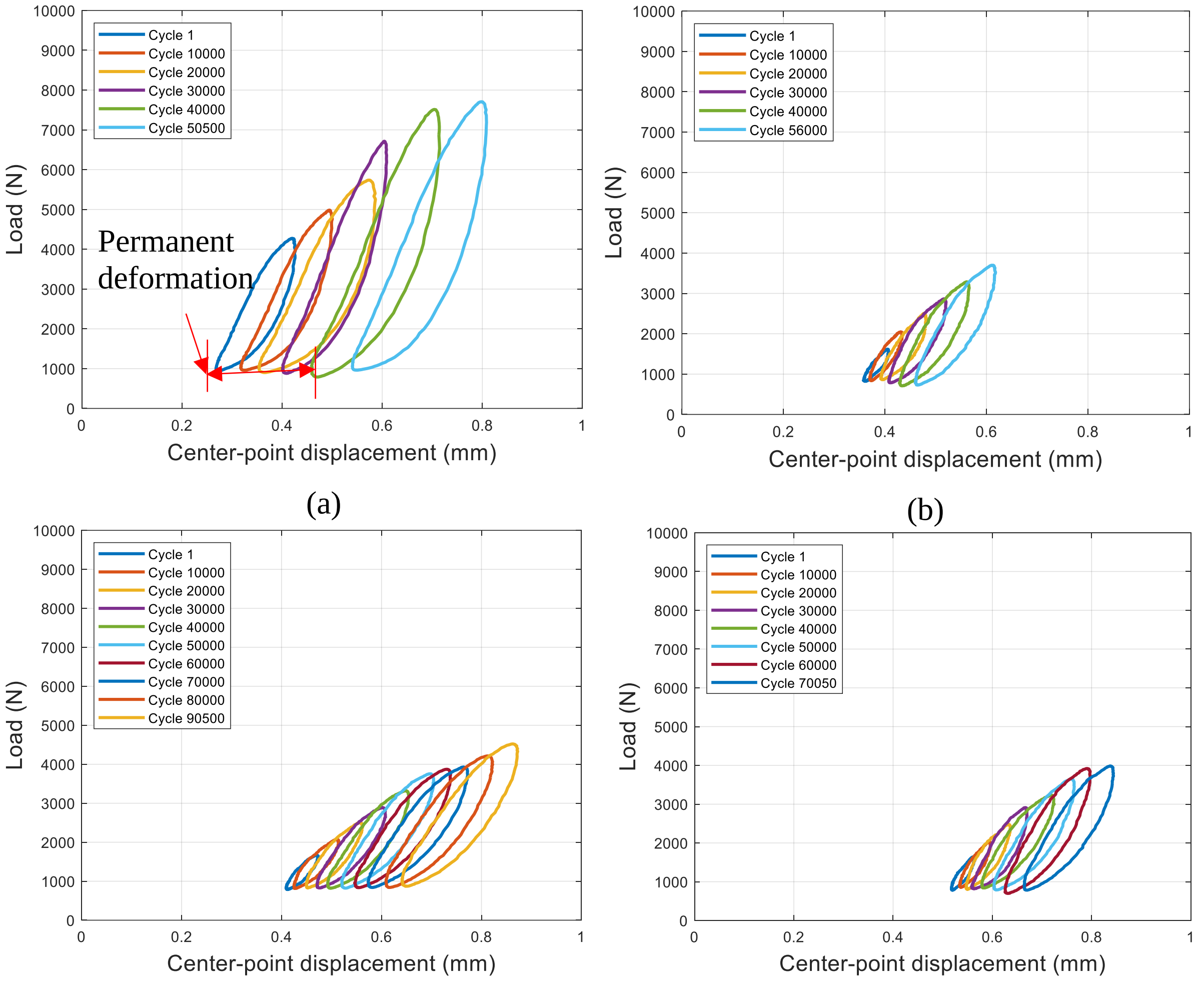

(a) (b) (c) (d)

Figure 41 Hysteretic force-displacement curves of representative specimens for (a) Mix S (b) Mix F (c) Mix M (d) Mix P

Table 10 Fatigue lives and permanent deformation before failure of different mixes

Specimen	Average permanent deformation (δ_d) (mm)	Average number of cycles to failure (N_f)
Mix F-repaired sample	0.18	58,580
Mix M-repaired sample	0.22	95,991
Mix P-repaired sample	0.11	57,530
Mix S	0.24	41,311

Note: The average results in this table are based on the results of four samples

Figs. 42(a) – (c) show the crack pattern of the repaired specimens under cyclic loading. This failure mode can be classified as adhesion failure [111] which is the same as the bond strength test described previously. Adhesion failure occurs when the bond strength between repair and substrate is lower than that of repair and substrate materials. This implies that the chemical bond between the repair and parent concrete is insufficient. Therefore, the use of a bonding agent or a rougher bonding interface may be required in this case. Fig. 42(d) shows the crack pattern of the intact specimen (Mix S). This failure mode can be classified as cohesion failure.

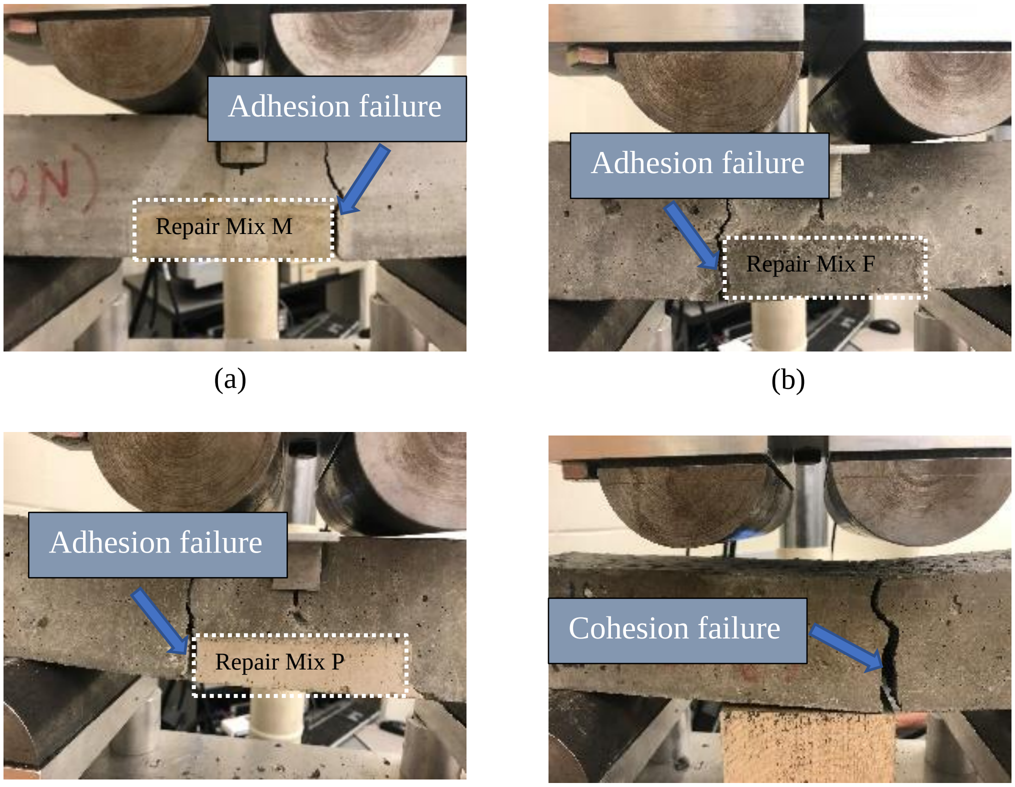

(a) (b)

(c) (d)

Figure 42 Failure mode under cyclic loading of (a) Mix M repaired specimen (b) Mix F repaired specimen (c) Mix P repaired specimen (d) Control Mix S specimen

4.4.3 Loss in E_{dyn} After Cyclic Loading

Dynamic elastic modulus (E_{dyn}) is an important property that indicates the loss in stiffness of a beam caused by cyclic loading. In this study, E_{dyn} is calculated based on the transverse resonant frequency of the 1st mode. Fig. 43(a) shows an example of the vibration signal captured by the accelerometer, and Fig. 43(b) shows the peaks in the frequency domain after fast Fourier transform (FFT) is performed.

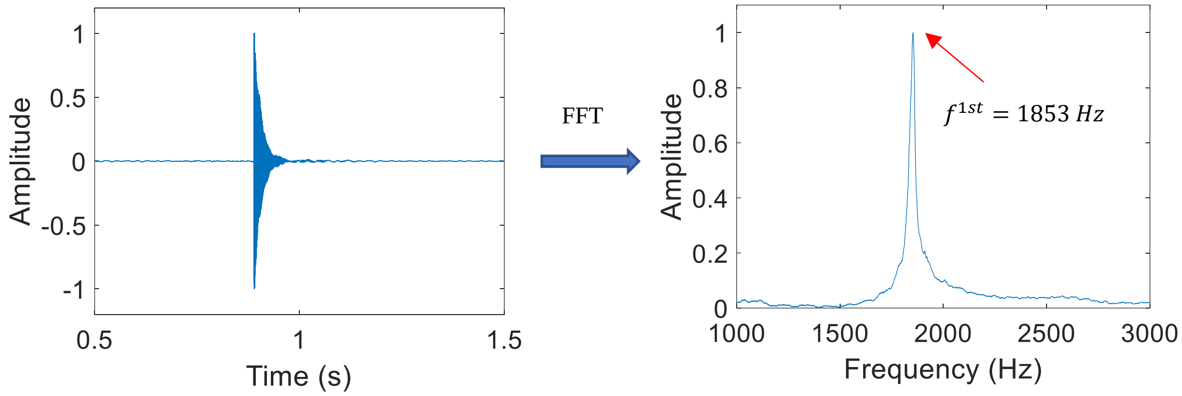

(a) (b)

Figure 43 Example of extracting resonant frequency (a) Vibration signal generated by hammer impact (b) Frequency spectrum obtained via FFT

Fig. 44 shows the changes in modulus of elasticity vs. loading cycles. The modulus of elasticity was measured when the maximum cyclic load was 55%, 65%, 75%, 85%, and 95% of the modulus of rupture of each sample type. It can be observed that as expected all mixes experienced a loss during the cyclic loading test. Mix S, F, P, and M had a percentage loss in dynamic elastic modulus of 2.3%, 5.2%, 3.6%, and 5.1%, respectively. Among all the mixes, the intact specimens (Mix S) had the lowest drop in E_{dyn}. It is because intact specimens (Mix S) did not have a concrete-repair interface, which contributes to better resistance to cyclic loading compared to repaired samples. Hui-cai et al. [215] proposed a micro-scale model depicting the three-layer structure at the concrete-repair interface. The middle layer contains a great deal of $\mathrm{Ca(OH)_2}$ and needle-shaped ettringite crystals, which result in a high porosity and weak bond. Among all the repaired samples, Mix F had the highest drop in elastic modulus (5.2%). This could be due to the low bond strength (as shown in Fig. 39) and low flexural strength of Mix F. According to ACI 318-14 [164], the flexural strength of Mix F can be estimated to be 5.5 MPa which is the lowest compared with flexural strength of Mix P and M (as shown in Fig. 14).

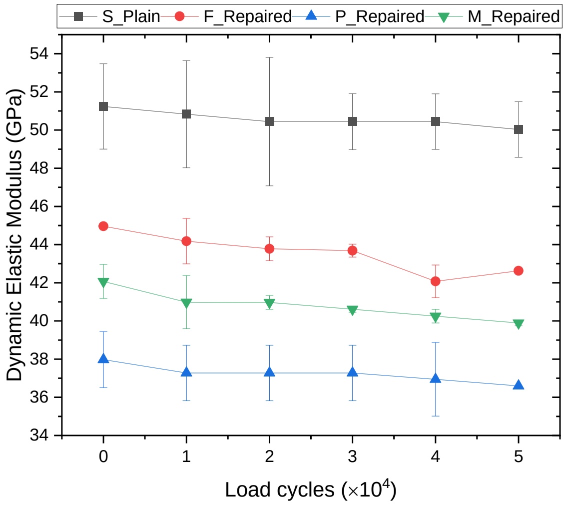

Figure 44 Change in dynamic elastic modulus as a result of flexural cyclic loading

4.4.4 S-N Curve of Repaired Beams

Fig. 45 shows the S-N curve for the four repaired mixes. The stress axis in this plot is normalized using the average modulus of rupture results. Based on Palmgren-Miner's rule, the slope value *b* of Mix S, F, M, and P can be calculated to be -0.033, -0.039.5, -0.013, and -0.026, respectively. In Table 11, S-N curves from other researchers [216]–[218] using normal strength concrete are listed for comparison. The slope values in their studies [216]–[218] range from -0.01 to -0.15, and these values from this study falls within this range. Note that other studies all used a fixed stress level for each specimen throughout the entire fatigue test process. This study used a novel concept of cycle groups, which accelerates the fatigue test process and can be regarded as producing similar S-N curves as other studies [219]. Among all the repair mixes, Mix M showed the lowest absolute slope value in Fig. 45 which indicates its superior performance under cyclic loading. This result is validated by the fact that Mix M had the highest average number of cycles before failure (95,991 cycles) compared to other mixes. Specimens repaired with Mix F showed a relatively steep slope, which means the failure stress drops tremendously with the increasing number of cycles. In the case of repaired specimens, the number of cycles is indicative of the bond quality of the repair. The slant shear and splitting tensile tests conducted in this study showed that Mix F had the lowest bond strength regardless of the curing days. Also, Mix F repaired specimens showed the largest drop in

E_{dyn} during the cyclic loading compared to repair mixes. These results are in line with the predicted S-N curve of Mix F.

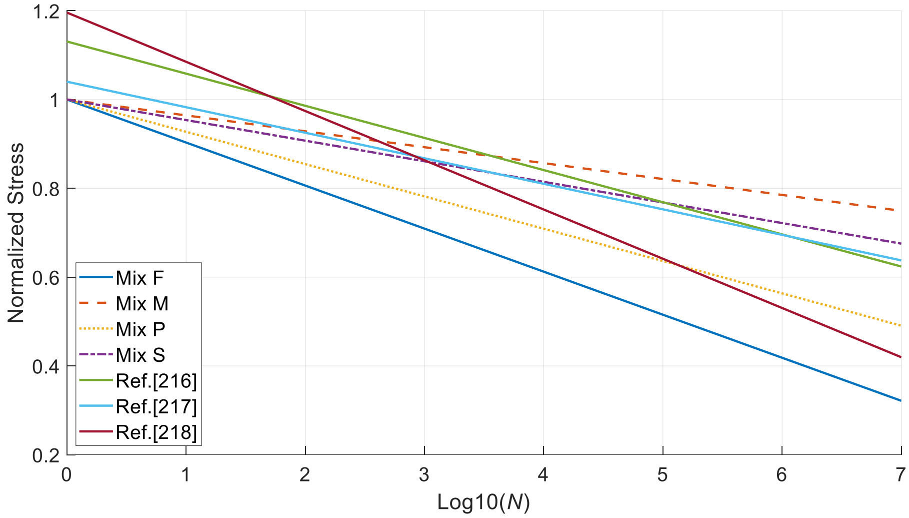

Figure 45 S-N curve for different samples

Table 11 S-N curves reported in literature

Ref.	S-N curve	Materials
[216]	$S = 1.1306 - 0.0724 \log_{10} N$	Self-compacting fiber reinforced concrete containing 0.5% by volume of steel fibers
[217]	$S = 1.0401 - 0.0575 \log_{10} N$	Concrete with 0.5% fibers added
[218]	$S = 1.1958 - 0.1109 \log_{10} N$	Concrete made with aggregates and 100% unsaturated polyester resin binders

The flexural fatigue endurance limit is an important design parameter, especially in applications like bridge deck overlays and pavements [219]. Endurance limit is defined as the highest stress the structure can sustain after two-million cycles of non-reversing loading [220], [221]. It is believed that if the structure can withstand two-million cycles without failure, it can meet almost all practical purposes [222]. In this study, the fatigue endurance limit of different repaired and control mixes is determined using S-N curves. The endurance limit was calculated by plugging the number of fatigue cycles (N) into the S-N curves to obtain the stress values (S) expressed as a percentage of ultimate strength. The two-million cycle fatigue endurance limit of Mix F-, Mix M-, Mix P-repaired specimens and the control mix is 38.9%, 77.4%, 54.1%, and 70.8% of the static flexural strength, respectively. The endurance limit of the control mix in this study is compared with the results of normal strength concrete reported in previous literature [219], [223], [224]. The modulus of rupture value of Mix S in this study is estimated to be 6 MPa based on the building code ACI 318-14 [164]. In a study by Goel and Singh [219], the normal-strength concrete having a modulus of rupture value of approximately 6 MPa was reported to have an endurance limit of 71%, which is similar to the results in this study (70.8%). The flexural strength of the mixes in [82] and [83] is 5 MPa and 3.28 MPa respectively which are lower than that of this study. Accordingly, the endurance limit of the mixes in [82] and [83] was reported to be 58% and 64% respectively, which is lower than that of this study. Compared with [219], [223], [224], this study produced similar results with less time consumed indicating the applicability of the novel testing methodology. Mix M shows the highest endurance limit among all repaired specimens including the control mix. However, this does not mean that Mix M-repaired specimens have longer service life than the control mix under fatigue loading as the static flexural strength of the control mix is almost twice as high as that of Mix M-repaired specimens.

4.4.5 Discussion of Results and Recommendations

In this section, results are supported by a general discussion and hypothesis by the authors. Mix S (control mix) showed twice the flexural strength of repaired samples, better energy absorption capacity (higher permanent deformation), and the least drop in E_{dyn} (2.3%) after completing cyclic loading regime. Though Mix S showed the lowest number of cycles to failure (41,311 cycles), it is not the true representation of the resilience of Mix S to cyclic load as Mix S has higher force amplitude applied during cyclic loading as opposed to repaired samples. It is most likely that the concrete-repair interface results in the difference between intact and repaired samples. Among all repair mixes, the S-N curve of Mix M showed the least slope which is validated by the number of cyclic load Mix M can withstand, as discussed in the previous section. According to the S-N curve, the two-million cycle fatigue endurance limit of Mix M is estimated to be 77.4% of the static flexural strength. To validate this finding, future work will be needed to load the specimen at a value of approximately 77.4% of its static modulus of rupture and determine its fatigue life. As per the Palmgren-Miner rule and Goodman linear model [32], it is assumed that the specimen will fail when the accumulative damage factor D_i reaches 100%. As a result, all S-N curves in this study in Fig. 45 have an intercept of 100%. However, it is seen that the S-N in the literature [216]–[218] reported an intercept higher than 100%. It is possible that some samples may not fail even when the maximum cyclic load reaches the static flexural strength of the samples. To address this issue, future work may include introducing a statistical distribution to describe the possibility of the structure failing under cyclic load that reaches 100% of the static load.

4.5 Conclusions

This study explored the applicability of the Palmgren-Miner rule on estimating the fatigue life of repaired concrete structures under cyclic loading. A novel loading regime consisting of increasing cyclic stress amplitude was used to accelerate the test process. The predicted S-N curve and 2-million-cycle endurance limit of different repaired specimens were validated by comparing with results including the number of cycles to failure, E_{dyn}, slant shear and splitting tensile bond strength, and hysteretic behavior. Additionally, the experimental results using the novel testing regime were compared with those using the traditional fatigue testing method. Based on the results from various tests in this study, the key conclusions are as follows:

1. Mix M (cementitious repair mortar) showed superior bond performance compared with different repair mixes currently used in the field. Mix M had an average shear bond strength of 12.3 MPa and 16.7 MPa and tensile bond strength of 1.4 MPa and 2.3 MPa at 14 and 28 days of curing, respectively. This study confirmed the benefit of using high-strength materials as repair to improve the bond strength.

2. The feasibility of using the Palmgren-Miner rule and Goodman linear model [32] to estimate the fatigue life of repaired structures was confirmed within the context of this study. Mix M, which was estimated to have the highest 2-million-cycle fatigue endurance limit (77.4%), showed the longest fatigue life (95,991 cycles) during cyclic loading test, the

highest slant, and splitting bond strength among all repair mixes. Future research may be required to further validate this conclusion by loading the specimen under a fixed cyclic loading range and determining its fatigue life.

3. This study found the usefulness of using cycle groups of increasing cyclic stress amplitude to accelerate the fatigue test process. The two-million cycle fatigue endurance limit estimated using cycle groups of Mix S (70.8%) was very similar to what was reported in the literature (71%) using the traditional cyclic loading method. The use of this method will help shorten the time for performing fatigue tests.
4. The substrate-repair interface was found to have an important role in determining the static and cyclic flexural performance of the repaired structure. Mix S (control mix) showed twice the flexural strength of repaired samples, better energy absorption capability (higher permanent deformation), and the least drop in E_{dyn} (2.3%) after cyclic load. The difference is mainly due to the cold-jointed concrete-repair interface which is the weakest part of the specimens during static and cyclic loading.

5. The predicted S-N curve was in line with bond strength, failure pattern, and modulus of elasticity measurements. Specimens repaired with Mix F (cementitious repair concrete), which had a steeper slope compared to other mixes, had the highest drop in elastic modulus (5.2%) and lowest shear and tensile bond strength.

6. The limitation of the Palmgren-Miner rule is that it assumes that the specimen will fail when the damage accumulation reaches 100%, which is contrary to the observations from past literature [219], [223], [224]. Future research may require the involvement of statistical distribution to account for this phenomenon for improved prediction accuracy.

Author Contributions: Conceptualization, Boyu Wang and Rishi Gupta.; methodology, Boyu Wang.; software, Boyu Wang.; investigation, Boyu Wang.; data curation, Boyu Wang.; writing—original draft preparation, Boyu Wang.; writing—review and editing, Rishi Gupta.; supervision,

Rishi Gupta.; funding acquisition, Rishi Gupta and Boyu Wang. All authors have read and agreed to the published version of the manuscript.

Funding: This research was funded by Natural Sciences and Engineering Research Council of Canada (NSERC), grant number CRDPJ 533917-18.

Data Availability Statement: Some or all data, models, or code that support the findings of this study are available from the corresponding author upon reasonable request.

Acknowledgments: Financial support of Natural Sciences and Engineering Research Council of Canada (NSERC) is greatly appreciated. Involvement and guidance of Terry Bergen and Peter Dias from Read Jones Christoffersen Ltd is also acknowledged. Assistance from technical staff Armando Tura and Geoff Burton is gratefully acknowledged.

Conflicts of Interest: The authors declare no conflict of interest.

Chapter 5 Evaluating Flexural Performance of Repaired Reinforced Concrete Under Static and Repeated Loading Using Non-destructive Methods

Boyu Wang[a], Rishi Gupta[b*]

[a] *Graduate Student, Department of Civil Engineering, University of Victoria, 3800 Finnerty Road, Victoria, B.C., V8W 2Y2, CANADA;* *https://orcid.org/0000-0002-9983-7606*

[b] *Professor, Department of Civil Engineering, University of Victoria, 3800 Finnerty Road, Victoria, B.C., V8W 2Y2, CANADA;* *https://orcid.org/0000-0002-3402-6095*

* Corresponding author, Tel +1 (250)721-7033, email guptar@uvic.ca

Note: This chapter is adapted from the paper that has been submitted to Journal of Engineering Structures (Elsevier) and is currently under review (submission date: Jan/16/2022). This chapter highlights the study of the flexural performance of repaired steel-reinforced concrete. It is found that the formulas proposed by CSA 23.3 can effectively predict the moment resistance of RC beams repaired by cementitious concrete and cementitious repair mortar with the modified binder.

5.1 Abstract

Deterioration of concrete structures is one of the major issues faced by the construction industry. Repair and rehabilitation are necessary to extend the service life of such structures. This study aims to investigate the effect of repair material type, length of repaired region, and loading regime on the structural characteristics of the repaired reinforced concrete (RC) beams. To achieve this goal, a total of 30 repaired and non-repaired RC beams were prepared and tested under static and repeated loading conditions. Three types of sounding-based non-destructive test (NDT) methods are employed to determine the material deterioration and sub-surface delamination after repeated loading. Results showed that under static loading conditions, full-length repaired beams had better performance than 1/3-span repaired beams. Beams repaired with cementitious repair mortar and

cementitious repair concrete in full length had a yield strength that was 14% and 9% respectively higher than that of beams repaired in 1/3 span. All RC beams with full-span repair outperformed the intact beams. After repeated loading, beams repaired with Mix M (cementitious repair material with modified binder) over full length showed a 14% improvement in yield strength compared to control samples. It was found that repair materials that had a high compressive and flexural strength are beneficial. The resonant frequency drops correlate well with the yield strength results. The formulas proposed by CSA 23.3 can effectively predict the moment resistance of both intact (control) and repaired RC beams. The ratio of experimental moment resistance values to its predictions ranges from 0.91 to 1.04.

5.2 Introduction

Existing reinforced concrete (RC) structures are subjected to structural deterioration due to their intrinsic defects (such as poor-quality concrete), external loading, and adverse environment [225]. In recent years, many materials or methods have been proposed to repair and strengthen RC structures to extend and retain their service life. They include the use of strain-hardening cement-based composite [9], [226], [227], polymer-modified cementitious mortar [228], geopolymer mortar [229], ultra-high performance concrete [230], [231], and fiber-reinforced polymer sheets [232]–[234]. Various repair products can be classified into three main categories including cement-based materials, polymer-modified cement-based materials, and polymer or resin materials [83]. The selection of repair materials is affected by the factors such as compatibility between repair and parent materials, durability, and bond strength of the repair materials [194]. Different repair materials have their own advantages and limitations. Portland cement mortar or concrete is one of the most common repair materials used because of its availability and low cost. However, under adverse environmental conditions, the performance of Portland cement-based products has been less than satisfactory, especially in aggressive exposure environments [84]. As a result, polymer modifiers such as acrylic, styrene butadiene, and some co-polymers have been added to modify the cement latex. The polymer-modified cement-based repairs are found to have improved bond strength, compressive, and tensile strength [235], reduced shrinkage [236], and permeability [235].

However, there is limited work that reported the performance of steel reinforced concrete structures repaired by cementitious materials with modified binders.

For actual structures, such as bridges, repeated loading simulates the real loading situation more closely than static loads. As a result, it is important to ensure that repaired structures have sufficient load-bearing capacity under both static and repeated loading conditions. Many studies focused on studying the static and fatigue loading performance of damaged RC beams strengthened with fiber-reinforced polymer [6], [7], [237], [238] and ultra-high-performance concrete sheets [194], [239]. The strengthening sheets made of polymers and cementitious composites are externally bonded to the tension side of RC beams with and without adhesives. The load-bearing capacity of the damaged structures was improved due to the increased cross-sectional area introduced by the externally bonded sheets. The effectiveness of using strengthening sheets is dependent on the use of sheet anchors [6], number of sheet layers [7], size of repair [239], and material properties of sheet layers [194]. Most studies [6], [7], [237]–[239] have found that externally bonded layers can effectively recover the load-bearing capacity of damaged beams and in some cases [238], the strengthened beams outperformed the undamaged beams. However, using externally bonded sheets could be limited when the deteriorated concrete and corroded steel reinforcement need to be removed prior to repair. The Guide To Concrete Repair [135] stipulates a series of steps for repair which involves saw cutting the perimeter of the repair area, removing the deteriorated and damaged concrete/steel, and then replacing it with different types of repair products. This repair technique does not increase the cross-sectional area of the repaired structures, which makes it different than using externally bonded sheets. Safdar et al. [11] investigated the flexural behavior of RC beams with part of the beams retrofitted with ultra-high performance fiber reinforced concrete (UHPFRC). It was found that the use of UHPFRC led to higher structural stiffness and delayed the formation of macro cracks. Teixeira et al. [10] conducted an experimental study that used a polymer-modified mortar and alkali-activated mortar to repair damaged RC beams. The repaired RC beams were prepared with a repaired region that accounts for 1/3 and 3/3 of the span. It was found that the repair length and type of repair materials affect the yield and ultimate strength. However, authors could not find research that studies the flexural behavior of such repaired RC beams under repeated loading. In a real loading condition, repaired beams are expected to experience load at different amplitudes. It is of interest to study the progressive damage after repeated loading and study the interfacial crack under such conditions, which forms the purpose of this study.

During repeated loading, it is important to monitor and assess the progressive damage that occurred within repaired RC structures. Most non-destructive test (NDT) methods can be classified as either a local or global damage identification technique [240]. The local damage identification techniques such as ultrasonic pulse velocity (UPV) method may require prior knowledge of approximate defect locations as testing the entire structure could be time-consuming. The UPV is dependent on the density and elasticity of the materials. Because of that, the UPV method is useful in detecting uniformity and determining the strength and mechanical properties of concrete [241]. The global damage identification technique such as vibration-based methods [242] examines changes in global vibration characteristics of structures and gives holistic evaluations on structural health. Modal parameters such as natural frequencies, mode shapes, and their variants are commonly used as damage indices. Capozucca [243], [244] found that the drop in natural frequencies of RC beams can well reflect the damages such as cracks and stiffness loss as a result of progressive damage. During repeated loading, it has been found that beams with cold-join interfaces may fail along with the cracking of concrete itself. Shah et al. [190] reported that the number of load cycles are high for intact specimens but decrease with the mismatch in elastic modulus of either side of the interfacial materials. Similar work was reported by Wang and Gupta [195], [245] that the concrete-repair interface at the perimeter of the repair area was prone to fail under flexural static and cyclic loading. The modulus of rupture of the repaired beam had approximately 50% of that of the intact beams. It can be critical to not only detect cracking but also the interfacial cracking between concrete repair and the substrate during repeated loading.

In summary, most previous studies focused on the static and cyclic loading performance of strengthened RC beams with externally bonded layers. However, scare studies reported repeated loading performance of beams where deteriorated materials are replaced by repair patches. It is of interest to study the bond between the repair and parent concrete and investigate the progressive damage after repeated loading and unloading. This study aims to study the mechanical properties of the repaired RC beams under static and repeated loading performance as compared to the control beams. The RC beams are repaired using two types of commercially available repair products over the middle third and full length. Two vibration-based sounding methods and UPV test methods are used to detect the progressive damage with repeated loads. The effect of repair material type, length of repaired region, and loading regime on the successfulness of repaired RC beams will be investigated. The models proposed by the current codes and standards are compared with the experimental results in this study. The findings of this study will contribute to better utilization of concrete repair for designing and developing more durable repaired RC structures.

5.3 Experimental Program

5.3.1 Materials

The materials used in this study involve one lab-developed normal strength concrete mix and two types of commercially available repair materials that are widely used in the field of restoring concrete structures. The normal strength concrete (termed as Mix S) serves as the parent material to receive the repair. Mix S is made of Type I cement, sand, gravel, superplasticizer, air entraining admixture, and water with a target strength of 45 MPa. The sand and gravel have fineness moduli of 2.85 and 6.60 respectively. The detailed mix proportions of Mix S are listed in Table 12. The two types of repair materials used in this study include cementitious repair concrete (Mix F) and cementitious repair mortar with modified binder (Mix M). Per bag of pre-mixed Mix F and Mix M, 2.5 kg and 2.37 kg of water are added following the recommendations from the manufactures. The water-to-material ratio (w/m) for Mix S, F, M are 0.08, 0.1, and 0.09 respectively. Table 13 summarizes the fresh and hardened properties of the two repair mixes and the control mix. The setting time information for each mix is obtained from the product brochure provided by the manufacturers. The air content and slump values are determined as per ASTM C231 [131] and ASTM C 143 [130] respectively. The compressive strength (f_c') is measured on samples after 28 days of curing in water at $21 \pm 2℃$ in accordance with ASTM C39 [132]. The results for slant shear bond and splitting tensile bond tests are adopted from a previous study [245] conducted by the authors. More information about the properties such as freeze-thaw, cyclic loading, and corrosion resistance of the repair materials can be found in Wang et al. [134], [195], [245] and Bajaj et al. [129].

Table 12 Mix proportions of the parent material receiving the repair ($\boldsymbol{kg/m^3}$)

Mix ID	Cement	Sand	Gravel	Superplasticizer	AEA[a]	Water
Mix S	450	762	1053	2.25	2.25	182.7

[a]AEA: Air Entraining Admixture

Table 13 Fresh and hardened properties of parent and repair mixes

Mix	Hardened Density (kg/m^3)	Air content (%)	Setting time (min)	w/m ratio	f_c' at 28 days (MPa)	f_r' at 28 days (MPa)	Slump (mm)	Slant shear bond (MPa)	Splitting tensile bond (MPa)
Mix S	2300	3	90	0.08	45 ± 2.7	4.8 ± 0.4	60	*	*
Mix M	2325	5.0	75	0.09	68 ± 2.4	7.0 ± 0.7	70	16.7 ± 2.3	2.3 ± 0.6
Mix F	2374	5.1	*	0.1	55 ± 2.2	4.9 ± 0.6	80	5.3 ± 7.4	1.3 ± 0.04

*Data Not Available

5.3.2 Test Specimens

A total of 30 RC beams are constructed and used for evaluating the flexural behavior of repaired RC beams under static and repeated loading. Six of them are control beams without repair while 24 beams are repaired beams using the two types of cement-based repair materials. Table 14 summarizes the specimen and the loading protocol details.

Table 14 Description of test specimens

Sample ID	Repair materials	Repair length	Loading protocols	Number of RC beams
Ctrl_st	None	Intact	Static/	3
Ctrl_r	None	Intact	Repeated loading	3
F_1/3_st	Mix F	1/3 span	Static	3
F_1/3_r	Mix F	1/3 span	Repeated loading	3
F_full_st	Mix F	Full length	Static	3
F_full_r	Mix F	Full length	Repeated loading	3
M_1/3_st	Mix M	1/3 span	Static	3
M_1/3_r	Mix M	1/3 span	Repeated loading	3
M_full_st	Mix M	Full length	Static	3
M_full_r	Mix M	Full length	Repeated loading	3

Six control beams labeled as “Ctrl_st” and “Ctrl_r” are tested under static and repeated loading, respectively. Twenty-four repaired beams are divided into 8 groups in accordance with repair length, repair material type, and loading protocol to cover various combinations for testing. Each group consists of three identical RC beams to have good confidence in test data. The naming of sample ID follows the rule: repair material_repair_length_loading protocol. For example, sample ID “F_1/3_st” represents that RC beams are repaired with Mix F, have a repair length of 1/3 span, and are tested under static loading. The dimension of the RC beams is shown in Fig. 46. Figs. 46 (a), (b), and (c) show the beam with 1/3-span repair, the beam with full-length repair, and the intact beam (control beam), respectively. The length of all RC beams is 900 mm with a rectangular cross section of 150 mm by 150 mm. The selection of the beam size follows the ASTM C31 [246]. Two rebars with 90° hooked ends are placed on the tensile side of the beam serving as longitudinal reinforcements, as shown in Fig. 46. Six stirrups were tied to longitudinal bars to prevent shear failure, and they have a maximum spacing of 125 mm. The 10M/400W black steel bars are used for making stirrups and longitudinal bars, which have a nominal diameter of 11 mm and yield strength of 400 MPa. The repair section has a thickness of 50 mm (2 inches) and a width of 250 mm (1/3 span) or 900 mm (full length) as shown in Figs. 46(a) and (b).

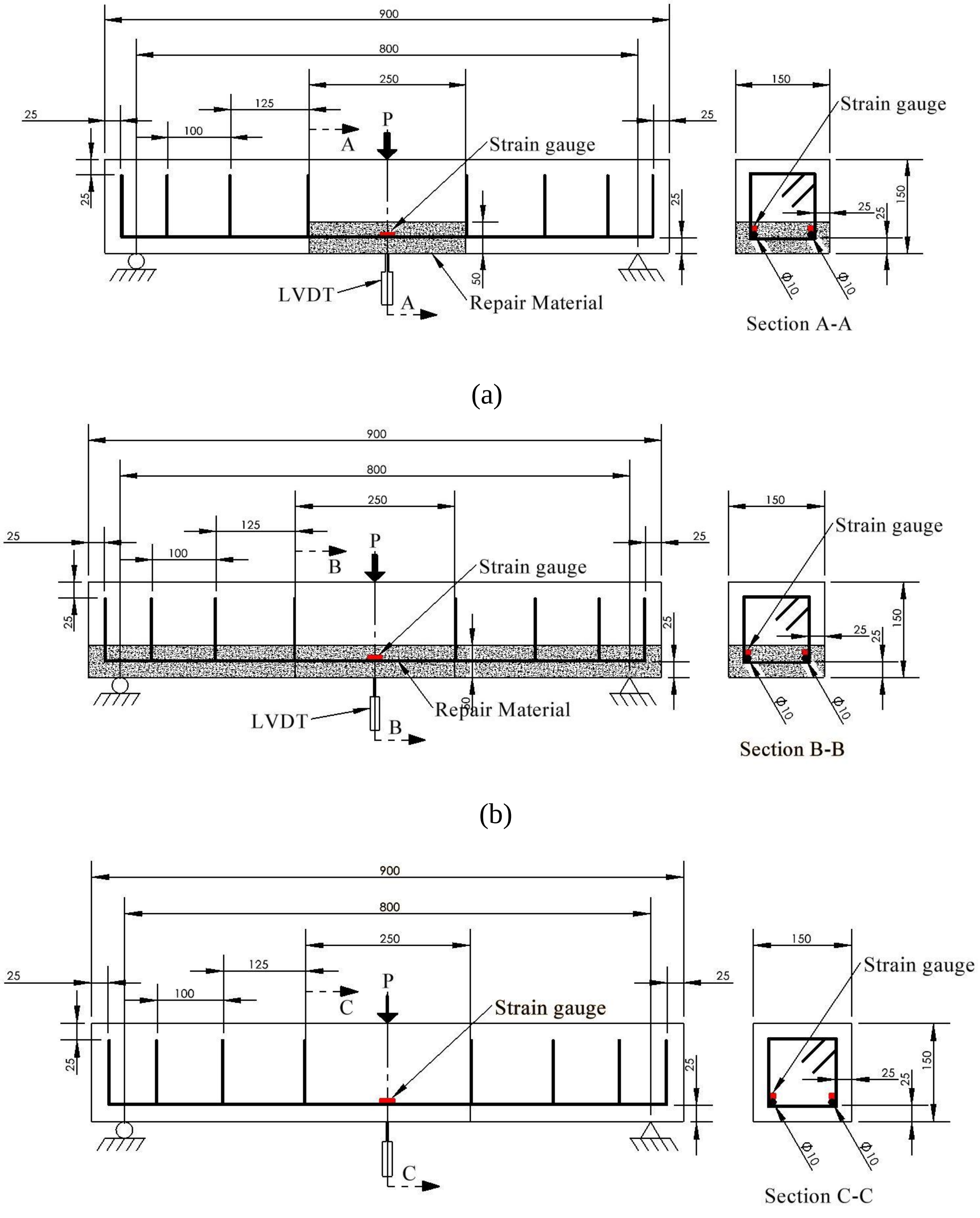

Figure 46 Steel reinforcement details for (a) RC beam with 1/3-span repair (b) RC beam with full-length repair (c) Intact beam without repair (all dimensions in mm)

5.3.3 Specimen Preparation Procedure

There are numerous examples in the field such as bridge decks or parking garages, where deteriorated concrete on the tension side is removed, parent substrate cleaned, and prepared to receive the repair materials. To simulate the in-situ repair conditions, prismatic beams with an induced cavity are cast. The fabrication procedure is shown in Fig. 47. Foam pieces are placed in the mold before concrete placement and then removed to induce a cavity. Textured papers are attached to the top surface of the foams. The textured papers have similar surface roughness as that of surface profile chip #6, which according to ICRI Technical Guideline No. 310R-2013 [136], simulates the surface profile on site for parking garages, as shown in Figs. 47(a) and 47(b). The benefit of using foam blocks with textured paper is that it can remove any variations associated with preparing the surface that receives the repair. After concrete placement in molds, according to ASTM C31/31M [246], five seconds of vibration using an internal vibrator is performed to consolidate the concrete. The specimens are kept at the ambient environment ($15 \pm 5^{\circ}\mathrm{C}\ with\ 80 - 90\%$ relative humidity) for 48 hrs before demolding. After demolding (as shown in Fig. 47(c)), they are transferred to a water bath. Water curing temperature is maintained at $23 \pm 2^{\circ}\mathrm{C}$, and all specimens are cured for 7 days followed by a 28-day air curing at ambient environment ($15 \pm 5^{\circ}\mathrm{C}\ with\ 80 - 90\%$ relative humidity). The inserted foams are then removed (as shown in Fig. 46(d)), and the specimens are repaired with Mix F and Mix M, as shown in Figs. 47(e) and (f). The repaired RC beams are left at ambient environment ($15 \pm 5^{\circ}\mathrm{C}\ with\ 80 - 90\%$ relative humidity) for 2 days and cured for 28 days before testing. Specimens are also constructed as control with no cavities and have the same curing time and condition as that of repaired samples.

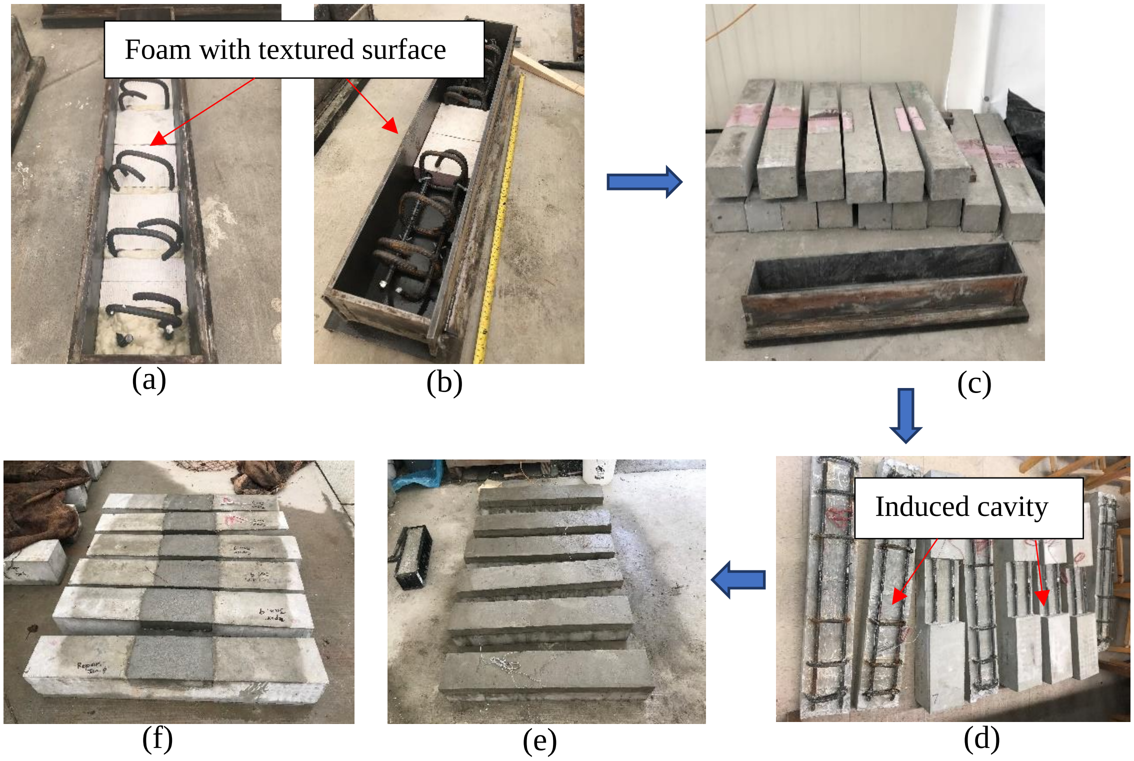

Figure 47 Sample preparation procedures (a) Inserting foam for full-length repaired beams (b) Inserting foam for 1/3-span repaired beams (c) demolded samples (d) Samples with foams removed (e) Full-length repaired beams (f) 1/3-span repaired beams

5.3.4 Test Setup and Instrumentation

5.3.4.1 Strain Measurement

Due to the large number of samples used in this study, only 1 out of 3 beams with the same sample ID (as shown in Table 12) has strain gauges attached. Two strain gauges are attached to each repaired beam. They are bonded to the bottom surface of the longitudinal bars in the middle of the beam.

5.3.4.2 Loading Protocol

A three-point bending test is performed on RC beams using a Materials Testing System (MTS) with a load-bearing capacity of 200 kN. Specimens were tested under both static and repeated loading. Under static loading, all specimens were loaded at a rate of $1\,mm/min$ until the yield stress of the steel is met and then at a rate of $2\,mm/min$ until the crushing of concrete is observed in the compression zone. The repeated loading protocol was adopted from the literature [247], [248]. During repeated loading, the test protocol consists of a sequence of increasing load at an equal interval of 5 kN. Fig. 48 illustrates the loading and unloading regimes that are adopted in this study. The maximum loads per cycle applied are 20 kN, 25 kN, 30 kN, 35 kN, 40 kN, 45 kN, which corresponds to different damage degrees, D_i (i = 1-6), of the beams after the loading. The beams are first loaded at a rate of $1\,mm/min$ until the maximum load is reached and unloaded at the same rate until the load is almost zero. Such loading-unloading process is repeated three times per load value before moving to the next damage degree. Between each damage level, NDTs are performed which include hammer percussion, modified chain drag, and ultrasonic pulse velocity tests, which are described in the following sections. One linear variable displacement transducer (LVDT) is mounted at the middle span of the beam to record displacement, as shown in Fig. 46. The displacement values are used to characterize the elastoplastic properties of the RC beams. After repeated loading (damage degree D_6), beams are loaded until failure at a rate of $1\,mm/min$.

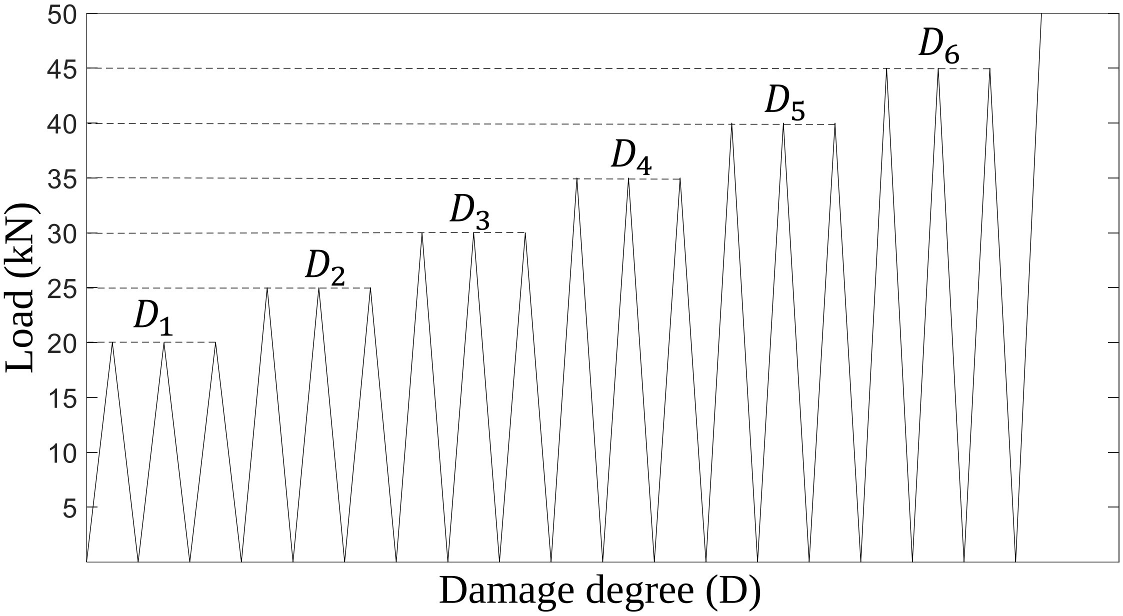

Figure 48 Loading-unloading regime of the repeated loading

5.3.4.3 Non-destructive Test Methods

Three types of sounding methods are employed to determine the material deterioration and sub-surface delamination after repeated loading. One of the standard methods to determine delamination is outlined by ASTM D4580 [139] and is called chain drag test, which has been widely used in the field. According to ASTM D4580, a heavy-duty chain or a hammer can be dragged over a concrete surface and the detection of delamination occurs by the test performer hearing dull or hollow sounds. However, this test is adversely impacted by the subjectivity of the test performer. To overcome this issue, in the current study, the sound of the impact is recorded by a microphone, and the frequency spectrum of the impact is extracted and used for defect identifications. Both hammer and chain are used to impact the concrete. Another sounding method called ultrasonic pulse velocity (UPV) is used to compare with the results measured by the previous two methods. The steps to perform the UPV test are outlined in ASTM C597 [249]. The detail for performing each test is explained in the following section.

Hammer Percussion Test

The hammer percussion test [124] is carried out using a 57 g (2 oz.) spherical head steel hammer striking the center of the beam to introduce low-amplitude vibrations of the beam, as shown in Fig. 49(a). The generated beam vibrations were detected by means of an acoustic recorder and microphone. The recorder has a sampling rate of 96 kHz at 24-bit depth, which indicates a working frequency range from 0 to 48 kHz. The microphone recorded vibration signals from two microphones, and the signal collected from the microphone that is closer to the concrete surface is used for frequency analysis. The recorder exported audio files in WAV format. Audacity audio software was used to trim the vibration signal such that the environmental noises before and after the impact can be removed. MATLAB software was used to perform a single-sided fast Fourier transform on the WAV files to extract frequency information.

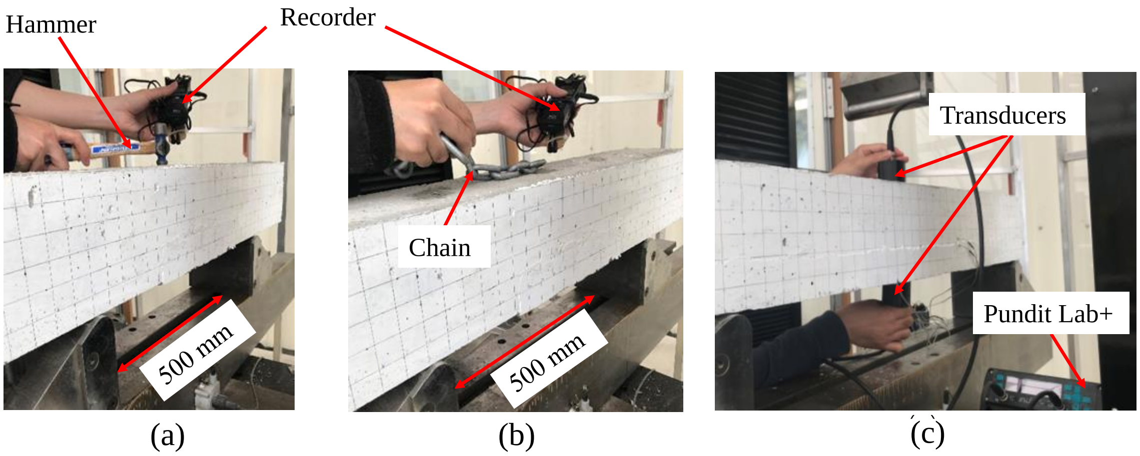

Figure 49 Experimental setup of (a) Hammer percussion test (b) Modified chain drag test (c) Ultrasonic pulse velocity test

Modified chain drag test

The modified chain drag test involves dragging a heavy-duty chain with four links over the concrete surface and collecting vibration responses of the beam using a digital recorder, as shown in Fig. 49(b). The chain link has a diameter of 9.5 mm (3/8 inch). The vibrational frequency of the beam is extracted from the recorded audio following the same data processing procedure of the hammer percussion test. Compared with the traditional chain drag test standardized by ASTM D 4580 [139], the modified chain drag removes the subjectivity of the operator variance from the test.

Ultrasonic pulse velocity (UPV)

UPV tests are executed using Proceq Pundit Lab$^+$ device. Transducers are placed at the center of the beam such that the ultrasonic pulse can travel across the repair and its interface, as shown in Fig. 49(c). The direct arrangement of the sensors is used to ensure the maximum signal transmission between the transducers. The transducer frequency was set as 125 kHz such that the wavelength of the ultrasonic wave is at least twice as large as the aggregate size and rebar diameter, which is recommended by the equipment supplier.

5.4 Experimental Results and Discussion

5.4.1 Failure mode and crack pattern

All beams were uncracked before testing. During repeated loading and unloading, noticeable crack initiation and propagation were observed on the beams. Fig. 50 shows the typical failure crack pattern of the repaired and control beams. The red color indicates the vertical cracks while the blue color represents the horizontal interfacial cracks. The symbol next to the cracks shows the damage level at which the cracks started. As shown in Fig. 50(a) and (b), the vertical bond failure initiated when the damage degree reaches D_4 and D_2 respectively for samples with a 1/3 span repaired by Mix M and Mix F. Table 15 summarizes the information about when the bond failure started in the vertical and horizontal direction. As shown in Table 13, Mix M showed higher slant shear and splitting tensile strength, which potentially delay the bond failure between Mix M and the parent material. As shown in Table 15, it is observed that all 6 samples with a 1/3-span repair had vertical interfacial cracks. Similar findings were reported by Wang and Gupta [245] that all repaired beams (without reinforcement) failed at the vertical concrete-repair interface.

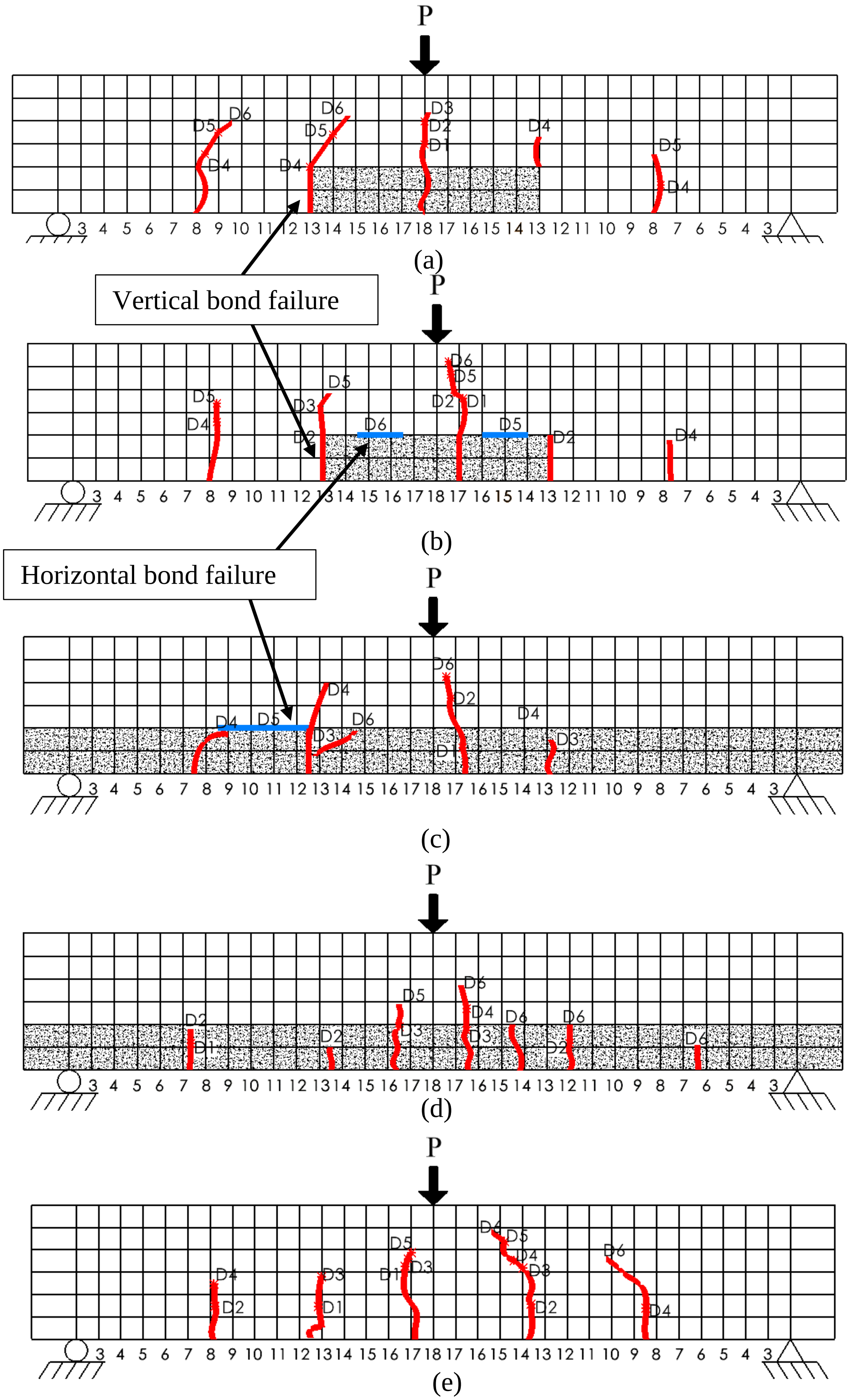

Vertical bond failure

Horizontal bond failure

(a)

(b)

(c)

(d)

(e)

Figure 50 Crack pattern of beams with (a) 1/3-span repaired with Mix M (b) 1/3-span repaired with Mix F (c) full-length repair with Mix F (d) full-length repair with Mix M (e) no repair

Table 15 Summary of damage levels at which vertical and horizontal bond failure started

Mix ID	Sample	Vertical bond failure initiation stage	Horizontal bond failure initiation stage
M_1/3_r	1	D_4	None
	2	D_4	None
	3	D_4	None
F_full_r	1	Not applicable	D_4
	2	Not applicable	D_3
	3	Not applicable	D_6
F_1/3_r	1	D_2	D_4
	2	D_2	D_5
	3	D_2	None
M_full_r	1	Not applicable	None
	2	Not applicable	None
	3	Not applicable	None

To quantify the progressive damage, the crack length of beams at each damage level was measured and summarized in Table 16. Note that the crack length includes both cohesive cracks and interfacial cracks that occurred at the concrete-repair interface. As shown in Table 15, at damage degree D_6, beams with a full-length repair by cementitious repair mortar with modified binder (Mix M) showed the lowest average crack length among all mixes. In comparison, the control mix showed the longest average crack length which is 556 mm.

Table 16 Summary of crack length after repeated loading

		Accumulative crack length in mm (including interfacial cracks)					
Mix ID	Sample	D_1	D_2	D_3	D_4	D_5	D_6
M_1/3_r	1	80	105	116	301	407	452
	2	0	50	85	236	354	420
	3	0	32	32	132	240	367
F_full_r	1	29	86	229	360	460	485
	2	0	85	199	310	486	556
	3	0	0	136	271	520	591
F_1/3_r	1	53	140	226	292	344	470
	2	92	203	235	346	462	519
	3	54	162	218	288	423	493
M_full_r	1	29	102	201	226	252	350
	2	0	40	80	116	158	249
	3	0	0	82	262	298	397
Ctrl_r	1	187	200	290	370	423	538
	2	205	267	319	462	586	610
	3	133	211	299	372	408	503

5.4.2 Load-deflection Behavior

5.4.2.1 RC Beams Under Static Load

Figs. 51 (a)-(c) show the load vs. center-point deflection curves for repaired and intact (control) beams.

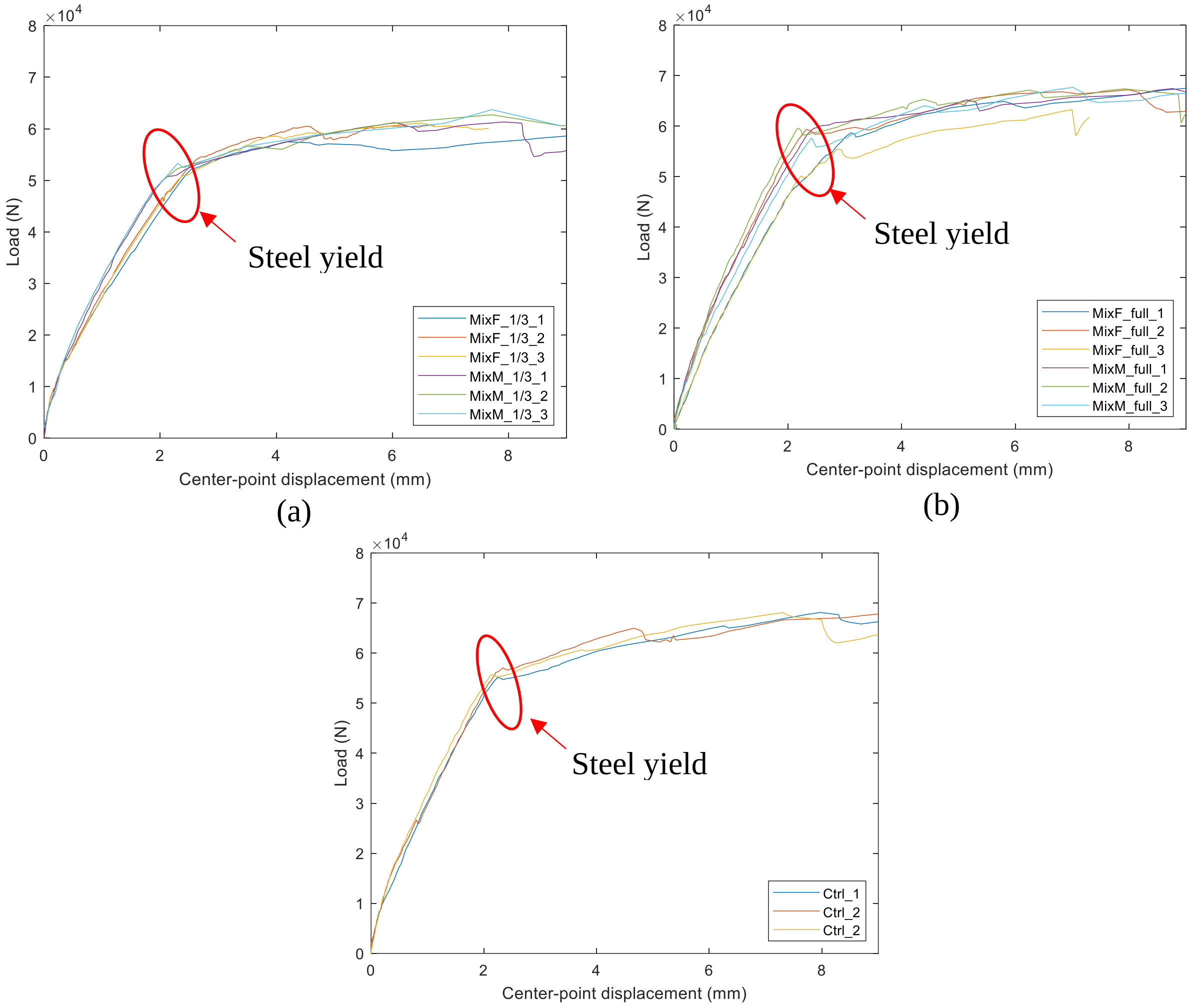

(a) (b)

(c)

Figure 51 Load-center point deflection curve of beams with (a) 1/3 span repair (b) full-length repair (c) no repair

Table 17 summarizes the yielding loads and NDT test results. The yield strength is measured based on the force-displacement curves. Compared with the intact beams (control), the average yield strength of beam M_full_st and beam F_full_st was 6.4% and 3.6% higher respectively. Compared with beams having 1/3-span repairs, the yield strength of beams having a full-span repair using Mix M and Mix F is 14% and 9% respectively higher. Khan and Abbass [9] found that the use of a layer of steel fiber-reinforced concrete on the tension side is beneficial to improving the yield strength of steel rebar. In the case of this study, Mix M has the highest flexural strength (7.0 MPa, as shown in Table 13) which helps increase the yield strength of Mix-M repaired beams. The yield strength of beam F_1/3_st and M_1/3_st was 5.3% and 6.9% lower than that of the control beam. During the static loading, interfacial cracking was observed. According to a previous study by Wang and Gupta [245], interfacial cracks between concrete and repairs could lead to as high as 50% loss in flexural strength for unreinforced concrete. We can see that such effect is mitigated in the case of RC beams as steel is carrying most of the tension forces. In terms of resonant frequency (RF) results, beams with higher yield strength tend to have a higher resonant frequency, whereas UPV results for all samples have no significant difference.

Table 17 Yield strength, bending stiffness, and NDT results

	Yield load (N)	Resonant frequency (Hz)		UPV through repair sections (m/s)
		Hammer percussion	Modified chain drag	
Ctrl_st	55504 ± 979	671 ± 3	670 ± 3	4505 ± 15
F_1/3_st	52545 ± 1865	587 ± 5	589 ± 6	4528 ± 39
F_full_st	57484 ± 2007	637 ± 3	638 ± 3	4535 ± 143
M_1/3_st	51692 ± 1210	606 ± 17	608 ± 16	4528 ± 39
M_full_st	59046 ± 1317	699 ± 7	699 ± 8	4579 ± 70

5.4.2.2 Beams Under Repeated Loading

Table 18 summarizes the yield strength of beams after going through 6 groups of loading-unloading cycles. The control mix samples experienced a loss of 4.9% in yield strength after repeated loading whereas the yield strength of other samples is comparable to that before repeated loading. This manifests that both Mix M and Mix F have better cracking resistance performance under repeated loading compared to the control mix. Because the repeated loading stress is smaller than the yield stress of steel and the number of cycles is much less than the fatigue cycles of the steel, so the steel did not experience much damage as opposed to concrete. It should be noted that beams with full-length repairs have higher yield strength compared to beams with a 1/3-span repair. During the repeated loading, interfacial cracking was observed which could potentially reduce the load-bearing capacity of the concrete and thus lead to an early yield of steel.

Table 18 Yield strength of the RC beams post repeated loading

	Yield load (N)
Ctrl_r	52791 ± 722
F_1/3_r	52909 ± 880
F_full_r	57269 ± 2742
M_1/3_r	52882 ± 680
M_full_r	60147 ± 722

5.4.3 NDT Results

The NDTs give quick and easy assessments of the beam damage after each increment of repeated loading. The goal is to capture early damage that may not be visible to naked eyes. Figs. 52 (a) and (b) summarize the drop in resonant frequency of the repaired and control beams after repeated loading and unloading. It can be observed that after the first load step (i.e., at damage degree D_1), all beams exhibited a significant drop in resonant frequency, which accounts for approximately 5-9% of its original resonant frequency. This is due to the generation of the cracks during the loading-unloading process. Following the first load step, the development of the cracks tends to stabilize such that frequencies drops are less remarkable until the yield of the steel reinforcement [250]. Regardless of the NDT methods used, intact and repair beams experienced a drop in resonant frequency ranging from 9% to 16% at damage degree D_6. After all load steps are completed, beams having full length repairs using Mix M (M_full_r) showed the lowest drop (9%) in resonant frequency while the control mix (Ctrl_r) showed the highest drop (16%) in resonant frequency. This is consistent with flexural test results as the Ctrl_r and M_full_r showed the lowest and highest average yield load, 52791N and 60147N, respectively. Previous studies [250], [251] reported that resonant frequencies reflect the changes in structural stiffness due to crack formation and thus are related to the damage severity of the structure. In this study, all specimens have the same rebar layout so the difference in yield load is mainly due to repair materials. Also, it is found that hammer percussion and modified chain drag method are well correlated and gave very similar NDT results.

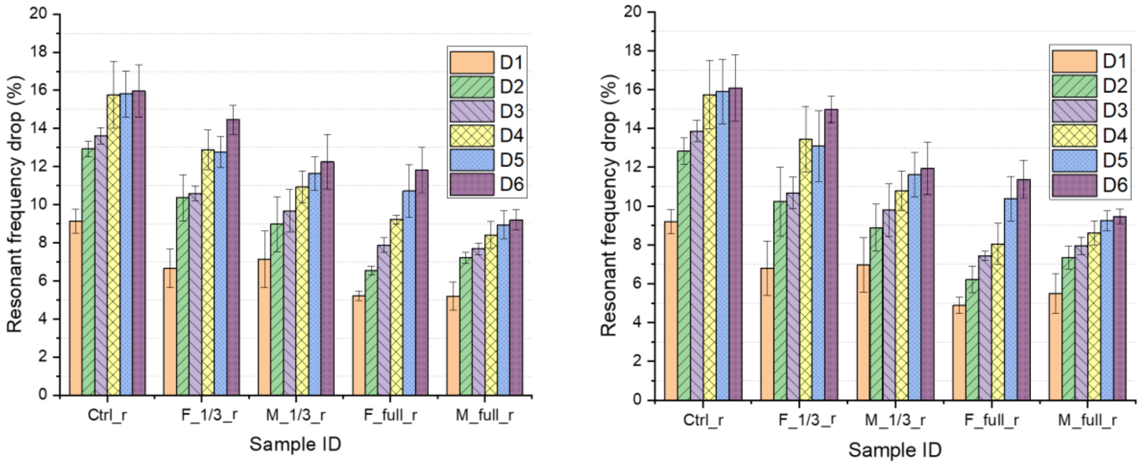

(a) (b)

Figure 52 Resonant frequency for beams at different damage degree D_i (i = 1,…,6) measured using (a) hammer percussion method (b) modified chain-drag method

The UPV test was performed at the center of the beam to detect debonding at the concrete-repair interface and damage caused by repeated loading. Figs. 52 show the drop in UPV for all samples at different damage degrees. An increasing drop in UPV values can be observed for all samples, which indicates the progressive damage due to repeated loading. When repeated loading was completed (at damage level D_6), samples F_1/3_r and F_Full_r showed the highest (2.6%) and second highest (2.0%) drops in UPV respectively among all repaired samples. This is most likely due to the concrete cracking and debonding between concrete and repair. As shown in Table 15, samples repaired with cementitious repair concrete (Mix F) showed more severe cracking compared to those repaired with cementitious repair mortar with modified binder (Mix M). Also, all beams with 1/3 span repaired with Mix F showed horizontal interfacial cracks. For sample F_1/3_r, the earliest horizontal interfacial cracks started to appear at damage level D_3 (shown in Table 15) which matches the notable drop in UPV as shown in Fig. 53. Also, it can be observed that UPV drop was more than 2% at damage level D4 for M_1/3_r, but for full-length repair

(M_Full_r), the UPV drop at the same damage level was less than 0.5%. Table 15 summarizes the horizontal and vertical bond failure results. No horizontal bond failure was observed for samples with a full-span repair and 1/3-span repair using mix M. As a result, it is likely that the difference in UPV drop between M_1/3_r and M_full_r is due to the micro cracks generated during the repeated loading for M_1/3_r samples. This requires further study in future such as using other testing techniques or microscope to find out the reason that led to this difference in UPV drop.

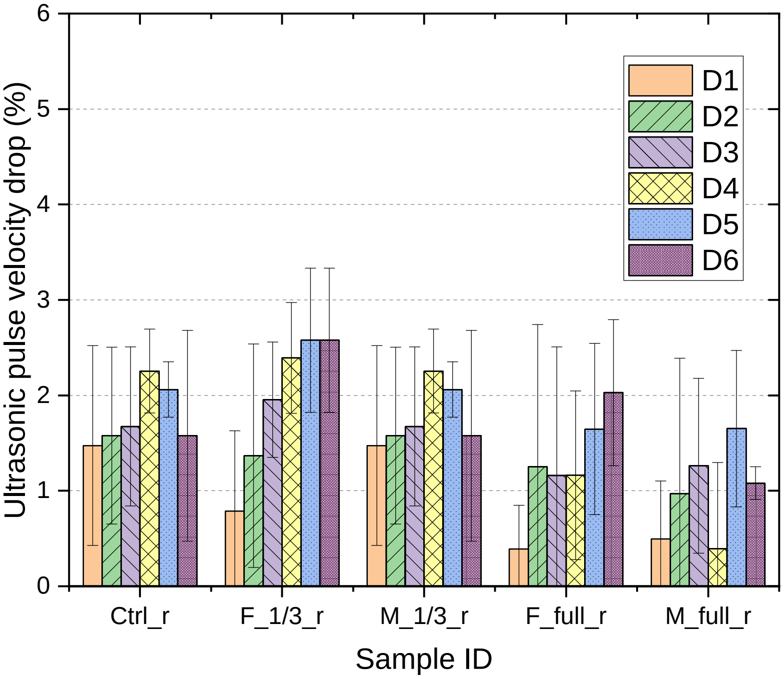

Figure 53 UPV of beams at different damage degree D_i (i = 1,…,6)

5.4.4 Load-strain Relationship

From strain gauges mounted on the rebar, the load-strain relationships of steel reinforcements of different repaired and control beams are plotted in Fig. 54. The tensile strain in the reinforced steel can be split into three distinct stages. The first stage is the elastic stage of concrete where cracking of the concrete has not yet started. At this stage, the load-strain curve is almost a vertical line because the load is majorly carried by the concrete, as shown in Fig. 54 from 0 to point A. It can be observed that repaired and control samples have a first cracking load ranging from 3000N to 7000N. The second stage is the elastic stage of the steel reinforcement. After the cracking of concrete, the steel reinforcement starts carrying most of the tensile forces. As shown in Fig. 54 from point A to B, the strain in steel reinforcements begin to grow. It can be observed that the slopes of the load-strain curves decreased slightly after the cracking of concrete (point A). Stage three is the yield stage of the steel reinforcement. As shown in Fig. 54, this happens when the strain in steel reinforcement significantly increases while the load only increases slightly. Compared with the beams that have gone through repeated loading, the slopes of the load-strain curves of the undamaged beams are slightly lower. This is due to the internal force redistribution for damaged beams which causes the rate of change of strain to differ between damaged and undamaged beams [252].

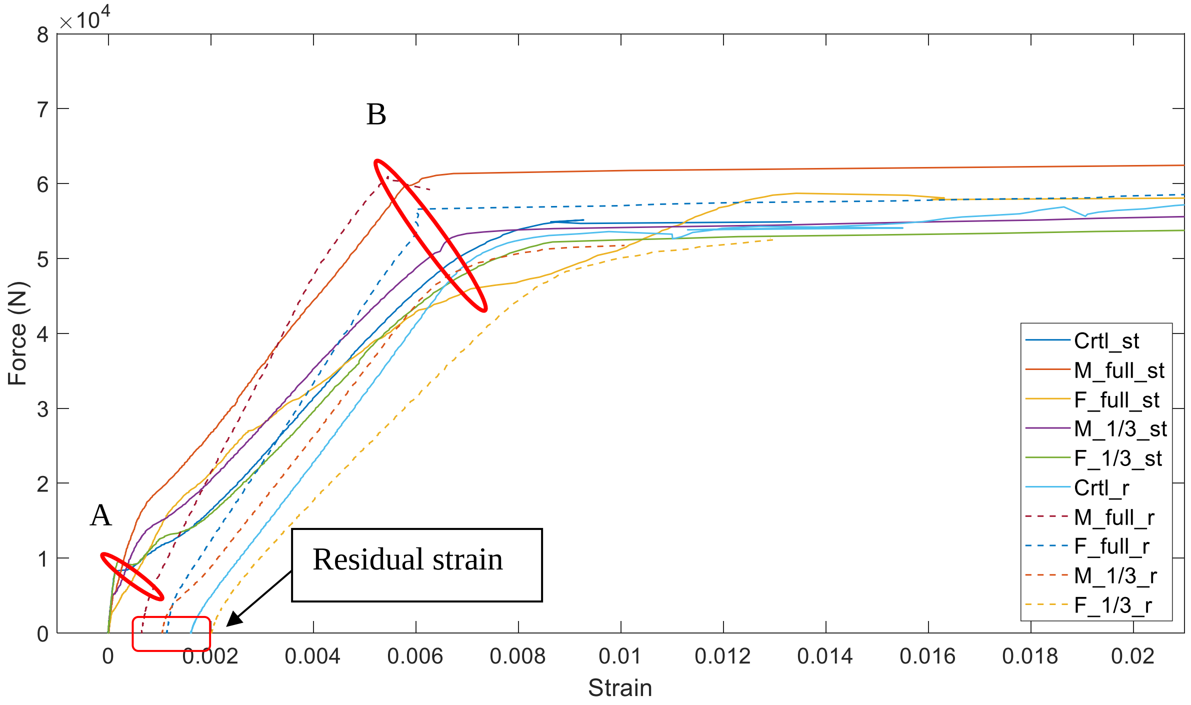

Figure 54 Load vs. strain of steel reinforcements

5.5 Theoretical Analysis of Load-bearing Capacity

The RC beam was designed such that it is expected to fail in steel control mode. An equivalent rectangular stress block was used to replace the actual stress distribution as per CSA 23.3 [253].

The depth of the rectangular stress block was determined using Eq. 15.

$$a = \frac{\emptyset_s f_y A_s}{\alpha_1 \emptyset_c f_c b} \tag{15}$$

Where,

α_1 is a mathematical parameter based on the requirement that the compression stress resultants of the actual and equivalent rectangular stress distributions are equal, f_y is the yield strength of tensile steel reinforcement, f_c is the compressive strength of concrete, A_s is the reinforcement area, $\emptyset_s$ and $\emptyset_c$ are the resistance factors of steel and concrete respectively, b is the width of the sample

The theoretical moment resistance (M_{r_th}) of the RC beam was calculated using Eq. 16.

$$M_{r\_\mathrm{th}} = \emptyset_s f_y A_s (d - \frac{a}{2}) \tag{16}$$

Where,

d is the distance from the centroid of the tension steel to the extreme compression fiber

The design guideline CSA 23.3 CL. 10.1. 7 also specifies the formula for calculating the first cracking moment of RC beams, as shown in Eq. 17 and Eq. 18.

$$M_{cr\_th} = \frac{f_r I_g}{y_t} \tag{17}$$

$$I_g = \frac{bh^3}{12} \tag{18}$$

Where,

M_{cr_th} is the theoretical cracking moment of the RC beam, f_r is the modulus of rupture of the concrete on the tension side measured by flexural test (with results summarized in Table 13), I_g is the moment of inertia of the gross cross-section of concrete beams around the neutral axis, y_t equals $h/2$ which is the distance from the neutral axis to the extreme tension fiber.

To determine the moment resistance (M_{r_exp}) and first cracking moment (M_{cr_exp}) of a beam experimentally, Eq. 19 and Eq. 20 are used respectively.

$$M_{r\_exp} = \frac{P_y L}{4} \tag{19}$$

$$M_{cr\_exp} = \frac{P_{cr} L}{4} \tag{20}$$

Table 19 summarizes the experimental and theoretical results of moment resistance and first cracking moment of test beams. Regarding the moment resistance, the ratio of experimental values to its theoretical prediction ranges from 0.98 to 1.04 for beams without repair and with full-length repair, which indicates a good correlation. Note that for beams with a 1/3-span repair, the theoretical calculation overestimates the moment resistance by 10%. The low moment resistance could be due to the weak interfacial bond which reduces the loading bearing capacity of the repair materials. In terms of first cracking moment, the theoretical calculations has a good prediction over beams repaired with Mix F with a ratio of 0.96. However, the prediction ratio of Mix M-repaired beams ranges from 0.72 to 0.79, which means concrete cracked before the flexural strength was reached. The reasons could be manifold. Since slight interfacial cracking was observed when loading the beam with 1/3 repair, the main cause could be due to a weak interfacial bond. For beams with full-length repair, the reason could be the size effect of concrete which is caused by the low workability of the mix. The size effect happens when the strength of a concrete member decreases when its size increases. For large area repair, the repair requires good workability for sufficient consolidation.

Table 19 Experimental and theoretical moment resistance and first cracking moment

Sample ID	Moment resistance			First cracking moment		
	M_{r_exp} $(kN \cdot m)$	M_{r_th} $(kN \cdot m)$	M_{r_exp} $/M_{r\_th}$	M_{cr_exp} $(kN \cdot m)$	M_{cr_th} $(kN \cdot m)$	M_{cr_exp} $/M_{cr\_th}$
Ctrl_st	11.1	11.4	0.98	2.4	2.7	0.89
F_1/3_st	10.6	11.4	0.93	2.7	2.8	0.96
F_full_st	11.5	11.4	1.01	2.7	2.8	0.96
M_1/3_st	10.4	11.4	0.91	2.8	3.9	0.72
M_full_st	11.9	11.4	1.04	3.1	3.9	0.79

5.6 Conclusion

The flexural behavior of RC beams repaired with different repair materials was investigated under both static and repeated loading conditions. The purpose of this study was to evaluate the effect of length of repair, bond strength, and flexural strength of repair on the flexural behavior of RC beams. To achieve this purpose, this study compared and analyzed the yield strength, load-displacement curve, load-strain curve before and after the repeated loading. In addition, three different NDT methods were employed to capture and estimate the material damage after each loading group of the repeated loading proposed by the authors. Based on the experimental study, the following conclusions are drawn:

1. The length of the repair affects the yield strength of repaired RC beams. Beams that are repaired in full length using cementitious repair mortar with modified binder (Mix M) and cementitious repair concrete (Mix F) had a yield strength that are 14% and 9% higher than that of beams repaired in 1/3 span.
2. The repair material that has higher bond strength and flexural strength is found to be beneficial to a more successful repair. Under static loading, beams repaired with Mix M (cementitious repair material with modified binder) in full length showed a 6.4% improvement in yield

strength compared to control samples. After repeated loading, beams repaired with Mix M in full length showed a 14% improvement in yield strength compared to control samples.

3. The hammer percussion and modified chain drag methods are useful methods to detect concrete cracking and accumulated damage by measuring the resonant frequency drop after repeated loading. The resonant frequency drops are well correlated with the destructive test results such as yield strength results.
4. The formulas proposed by CSA 23.3 can effectively predict the moment resistance of both intact (control) and repaired RC beams for the geometry studied in this research. The ratio of experimental moment resistance values to its predictions ranges from 0.91 to 1.04. In addition, the formulas proposed by CSA 23.3 can well predict cracking moment of control and Mix F-repaired RC beams. To improve predictability for RC beams repaired with high-strength mortar, authors recommend taking into account bond-substrate failure and size effect of concrete specimens.

5.7 Future work

This chapter presents a preliminary study that investigated the performance of repaired RC beams under static and repeated loading conditions. It was found that repair materials having high compressive and bond strength showed excellent resistance to interfacial cracking under repeated loading, whereby the repaired RC beams achieved a yield strength of 6.4% higher than that of intact beams. Future work will involve testing the repaired RC beams under both FT and cyclic loading conditions. Duan et al. [254] studied the flexural behavior of reinforced concrete beams under FT. It was found that both ultimate breaking load and the yield load of RC beams decreased with increasing FT cycles. Duan et al. [254] observed the surface scaling and internal damage due to FT exposure, which resulted in reduced concrete strength on the compression side of the beams. Since the rebar was the main load-carrying component on the tension side, the effect of FT on steel rebars in RC has also been studied [255], [256]. It was found that FT exposure aggravates the steel corrosion and reduces the concrete-rebar bond, which led to reduced load-bearing capacity of the RC beams. When RC beams are loaded under cyclic loading conditions, the common failure mode is due to the steel rupture [7], [194]. However, there is scarce work that investigates the combined effect of FT and cyclic loading and thus this part will be the future scope of this work.

Funding: This research was funded by Natural Sciences and Engineering Research Council of Canada (NSERC), grant number CRDPJ 533917-18.

Data Availability Statement: Some or all data, models, or code that support the findings of this study are available from the corresponding author upon reasonable request.

Acknowledgments: Financial support of Natural Sciences and Engineering Research Council of Canada (NSERC) and RJC is greatly appreciated. Involvement and guidance of Terry Bergen and Peter Dias from Read Jones Christoffersen Ltd. is also acknowledged. Assistance from technical staff Bastien Lanusse and Geoff Burton is gratefully acknowledged. Assistance from colleague Perla Rodulfo in experimental work is greatly appreciated.

Declaration of Competing Interest: The authors declare no conflict of interest.

Chapter 6 Modeling the Freeze-thaw and Cyclic Loading-induced damage

6.1 Introduction

FT cycles have long been recognized as one of the major causes of the premature failure of concrete in cold regions. The damage caused by FT cycles was due to the expansion of water existing in concrete. In real life, a structure can experience the combined effect of FT cycles and external load. For structures, such as bridges and pavements, repeated/cyclic loading is closer to the real loading situation than static loads. Many researchers have been trying to model the damaging effect as a result of either FT or cyclic/repeated loading, but the combined damage effect was less reported. More importantly, the mechanical response of concrete to cyclic/repeated loading is different from that to FT [257]. The FT damage originates from the development of micro-cracks due to the internal stress and strain during the freezing process. With increasing FT cycles, the uniformly distributed micro-cracks will propagate due to the progressive changes in pore microstructures. In contrast, cyclic load damage originates from the pre-existing defects in concrete and aggravates due to the externally applied cyclic load. The small cracks will gradually merge into large cracks with increasing load cycles until a fracture takes place. Due to the different damage mechanisms between cyclic load and FT, it is significant to unify the damaging effect of both conditions and predict the structures’ service life.

To model the behavior of structures under combined FT and cyclic loading, different researchers approach this problem differently. They can mainly be divided into three categories depending on their testing conditions. The first case [258]–[260] is when concrete experienced flexural fatigue load and FT cycles simultaneously. It was found that the damage caused by coupled fatigue and FT loading caused more severe damage than that caused by summing the damage of each individual loading condition. Li et al. [259] proposed a numerical model predicting the remaining service life of samples under such coupling conditions, which showed satisfactory results. The second condition [261], [262] is that the samples are loaded with alternating FT and compressive loading groups. It is found that the number and width of the cracks increase with the increase of alternating times of repetitive load and stress level. The third condition [263], [264] is that repeated loading is performed on FT-damaged samples. A damage constitutive model was proposed to predict the repetitive stress-strain curve of samples after FT damage. To take FT damage into a model, a shape factor is proposed which is dependent on FT cycles and stiffness degradation after FT exposures.

In this study, we aim to study the effect of FT on the fatigue performance of repaired concrete. As a result, specimens were first exposed to FT and cyclic loading separately to determine their damage. The damage model for individual FT and cyclic loading exposure on repaired concrete were proposed. The FT exposure causes a reduction in dynamic modulus of elasticity and flexural strength of repaired concrete, which results in reduced cyclic service life. Therefore, the initial flexural strength was adjusted and incorporated into the formulas that are used to predict the service life of the repaired concrete.

6.2 Damage Model of FT Exposure

The issues caused by FT cycles have been studied since the middle of the last century. The internal damage of concrete under FT is widely believed to be caused by the freezing of water within the concrete’s pore system. As a result, the damage of concrete under freeze-thaw can be modeled in three different levels including microscopic, mesoscopic, macroscopic levels. For microscale and mesoscopic models [88], [265]–[269], the porosity, pore diameter, pore volume, and pore size distributions are the key damage parameters to characterize the FT damage. Using these models can give a more accurate prediction about the mechanical and thermal behavior of concrete under FT compared to macroscale models. However, it is challenging to obtain the micro- and meso-damage parameters due to the complex pore structures. For macroscale models [87], [270], [271], damage parameters such as deformation, strength, dynamic elastic modulus, and moisture content are commonly used to characterize the FT damage. The benefit of using macroscale parameters is that they are easy to be measured and acquired. Currently, there are no FT damage models for repaired structures, so we aim to start with building a model based on macroscale damage parameters. Based on the basal theory of damage mechanics, the dynamic elastic modulus is used to quantify the FT damage. A summary of previous macroscale models for FT damage is shown in Table 20.

Table 20 Summary of FT damage models in the literature

Ref.	Materials	Relationship	Symbol meanings
[270]	Alkali-activated slag concrete	$D = 1 - \frac{(E_{dyn})_{FT=n}}{(E_{dyn})_{FT=0}}$ $= aN^b$	N is number of FT cycles; a and b are regression coefficients; E_{dyn} is dynamic modulus of elasticity
[272]	Portland cement concrete	$D = 1 - \frac{(E_{dyn})_{FT=n}}{(E_{dyn})_{FT=0}}$ $= \alpha - \beta \ln\left(\frac{k}{N} - \gamma\right)$	N is number of FT cycles; α, β, k, and γ are regression coefficients; E_{dyn} is dynamic modulus of elasticity
[263]	Portland cement concrete	$r = \frac{Dk_c}{k_c - k_{sec}}$ $D = aN^2 + bN + c$	N is number of FT cycles; k_c and k_{sec} are initial stiffness and secant stiffness after repeated uniaxial compression; a, b, and c are regression coefficients; r is shape factor
[273]	Concrete-concrete interface	$D(N) = (\tau_0 - \tau_N)/\tau_0$	τ_0 and τ_N represent the shear bond strength at 0 and N cycles of FT

As shown in Table 20, Fu et al. [270] used dynamic modulus of elasticity as damage variables to model the FT damage, which was assumed to be a power function of the number of FT cycles. The model showed good predictivity. Wang et al. [272] used dynamic modulus of elasticity as damage variables, which was assumed to be a logarithmic function of the number of FT cycles. Both Fu et al. [270] and Wang et al. [272] proposed the damage constitutive models of concrete after FT exposure. Qiu et al. [263] established the regression curves between FT damage and the number of FT cycles. They induced a damage factor that is dependent on the number of FT cycles to modify the stress-strain curve of concrete after FT damage. Tian et al. [273] measured the shear strength at the concrete-concrete interface and used it as the damage variable, which is a function of the number of FT cycles. Based on the literature review, it can be seen that dynamic elastic modulus, number of FT cycles, and bond strength were commonly used as damage variables. The limitation of using destructive test results such as bond strength as damage variables is that destructive methods can introduce further damage to the structures and can be time-consuming. In comparison, as discussed in Chapter 3, using NDT methods such as hammer percussion and modified chain drag allows users to have quick and easy evaluations of structures' health. The measured dynamic modulus of elasticity was found to correlate well with destructive test results. For that reason, this study uses dynamic modulus of elasticity as the damage variable, as shown in Eq. 21. Similar to [272], E_{dyn} was assumed to have a logarithmic relationship with the number of FT cycles, as shown in Eq. 22. A regression analysis was performed to calculate regression variables and the results are summarized in Table 21.

The damage variable is formulated as shown in Eq. 21.

$$D_{FT} = \left(1 - \frac{(E_{dyn})_{FT=n}}{(E_{dyn})_{FT=0}}\right) \times 100 \tag{21}$$

$$D_{FT} = a \ln\left(\frac{N_{FT}}{b} + 1\right) \tag{22}$$

Where,

a and b are regression variables; D_{FT} is the percent of damage caused by FT cycles; N_{FT} is number of FT cycles.

Table 21 Damage models for repair and control mixes

Mix ID	S-N curve	R^2
Mix S	$D_{FT} = 19.99 \ln\left(\frac{N_{FT}}{89.91} + 1\right)$	0.93
Mix F	$D_{FT} = 3.967 \ln\left(\frac{N_{FT}}{5.516} + 1\right)$	0.97
Mix M	$D_{FT} = 0.6708 \ln\left(\frac{N_{FT}}{0.06955} + 1\right)$	0.86
Mix P	$D_{FT} = 1.023 \ln(N_{FT} + 1)$	0.83

Note: N_{FT} represents the number of cycles of FT exposure and thus has a range of $N_{FT} \geq 0$

In section 3.5.4, a linear relationship was found between destructive test results (modulus of rupture) and non-destructive test results (dynamic elastic modulus). More importantly, for concrete without repair (intact beams), the linear relationship between destructive and NDT results remains unchanged before and after FT exposure. As a result, as demonstrated in Chapter 3.5.4, the relationship is formulated as shown in Eq. 23 and Eq. 24.

$$(E_c)_{FT=0} = (\tfrac{w_c}{2300})^{1.5} \times (5500(f_r')_{FT=0} + 6900) \tag{23}$$

$$(E_c)_{FT=n} = (\tfrac{w_c}{2300})^{1.5} \times (5500(f_r')_{FT=n} + 6900) \tag{24}$$

Where,

f_r' is the modulus of rupture value, and E_c is static modulus of elasticity, w_c is the density of the parent specimen (when the repair portion is not substantial), which is computed by dividing mass by volume. To correlate static elastic modulus of elasticity (E_c) with dynamic elastic modulus of elasticity (E_{dyn}), Zhou et al. [167] proposed the empirical equations based on input parameters including volume content of aggregate and maximum size of coarse aggregates, as shown in Eqs. 25-27.

$$E_c = eE_{dyn} + k \tag{25}$$

$$e = 0.048V_{agg} + 0.005M_{agg} + 0.8755 \tag{26}$$

$$k = -0.855V_{agg}^3 - 0.023 \tag{27}$$

Where,

e and k are regression coefficients; V_{agg} is the volume content of aggregates in percentage, M_{agg} is the maximum coarse aggregate size in mm.

By using Eqs. 21-27, the dynamic elastic modulus after n FT cycles ($(f_r')_{FT=n}$) can be derived and expressed as a function of modulus of rupture before FT damage ($(f_r')_{FT=0}$) and damage variable (D_{FT}), as shown in Eq. 28. Eq. 28 can be used to estimate the modulus of rupture value after FT damage ($(f_r')_{FT=n}$).

$$(f_r')_{FT=n} = (1 - D_{FT})(f_r')_{FT=0} - \frac{69}{55}D_{FT} \tag{28}$$

6.3 Damage Model of Cyclic Loading

In this study, a loading regime consisting of cycle groups with increasing stress amplitude was used to accelerate the cyclic test process as described in Chapter 4.3.2. To quantify the cumulative fatigue damage caused by variable amplitude loading, one of the most recognized methods is Palmgren-Miner's linear cumulative rule [189]. The damage index is defined as a function of the mid-range stress, alternating stress, ultimate strength, and the number of cycles under a specific stress level. According to this Palmgren-Miner's rule, the damage is believed to accumulate linearly, and failure occurs when damage reaches a critical threshold. Over the years, efforts have been made to improve prediction accuracy by involving more input factors such as loading history [27], [274], stress ratio [28], thermodynamics potential [29], and fatigue inelastic parameters [26]. In the context of this study, the stress ratio during the cyclic loading is considered. The formulas that were used in Palmgren-Miner's rule in this study are summarized in section 4.3.2. Table 22 summarizes the S-N curve of three types of repairs as well as the control mixes based on test data from this research work.

Table 22 S-N curves of repaired and intact beams in this study (from Chapter 4)

Mix ID	S-N curve
Mix S	$S_{norm} = N^{-0.033}$
Mix F	$S_{norm} = N^{-0.039}$
Mix M	$S_{norm} = N^{-0.013}$
Mix P	$S_{norm} = N^{-0.026}$

6.4 Service Life Model of FT-damaged Concrete Under Cyclic Load

To predict the mechanical behavior of concrete after FT damage, Qiu et al. [263] introduced a shape factor to modify the stress-strain curve. The shape factor is a function of the number of FT cycles and stiffness, as shown in Table 20. As a result, in this study, we introduced a damage variable which is a function of dynamic modulus of elasticity (defined in Eq. 21) and use it to modify the S-N curve. Eq. 29 is the modified S-N curve which is used to predict the cyclic service life of concrete after FT exposure. Eq. 29 was derived from Eqs. 28 and 11. The details for performing the calculation have been described in Chapter 4.3.2.

$$S = (f_r')_{FT=n} N^b \tag{29}$$

where N is the number of cycles to failure, S is the stress applied on the specimen, and b is the slope of the straight line, and $(f_r')_{FT=n}$ is the modulus of rupture results after n cycles of FT exposure. By using Eq. 27, the cyclic service life of repaired and control samples after FT exposure is calculated, as summarized in Table 23.

Table 23 Summary of service life prediction curves

Mix ID	S-N curve
Mix S	$S_{norm} = \left(1 - \frac{19.99\ln\left(\frac{N_{FT}}{89.91}+1\right)}{100} - \frac{0.25\ln\left(\frac{N_{FT}}{89.91}+1\right)}{(f_r')_{FT=0}}\right) * N^{-0.033}$
Mix F	$S_{norm} = \left(1 - \frac{3.967\ln\left(\frac{N_{FT}}{5.52}+1\right)}{100} - \frac{0.05\ln\left(\frac{N_{FT}}{5.52}+1\right)}{(f_r')_{FT=0}}\right) * N^{-0.039}$
Mix M	$S_{norm} = \left(1 - \frac{0.671\ln\left(\frac{N_{FT}}{0.06955}+1\right)}{100} - \frac{0.008\ln\left(\frac{N_{FT}}{0.06955}+1\right)}{(f_r')_{FT=0}}\right) N^{-0.013}$
Mix P	$S_{norm} = \left(1 - \frac{1.023\ln(N_{FT}+1)}{100} - \frac{0.012\ln(N_{FT}+1)}{(f_r')_{FT=0}}\right) * N^{-0.026}$

Note: N represents the number of cycles to failure under cyclic loading and thus has a range of $N \geq 1$; S_{norm} represents the normalized stress which ranges from 0 to 1

6.5 Model Validation

The FT-cyclic loading coupling model proposed in the previous section can be used to predict the cyclic fatigue life of structures after FT exposure. The proposed model is validated using the experimental data from the literature [275]. Since the literature used intact beams as the testing objects, the proposed model for Mix S (intact samples) is validated in this section. In the literature [275], prismatic specimens having a dimension of 100 mm x 100 mm x 400 mm were prepared using M50 concrete. The samples had a compressive strength of over 50MPa which is close to the material's strength (59 MPa) in our study. The samples in the cited study had an air content of 2%

which is lower than the 4.9% in our study. As a result, it is expected that FT exposure causes more damage to samples in the cited work than to that in our study.

In the literature [275], the samples were first exposed to FT damage followed by a cyclic loading to determine their service life. The FT test consists of lowing the chamber temperature to $-18℃$ and then raising the temperature to $5℃$ within a time frame of 2-5 hours, which is similar to the test condition stipulated by ASTM C666. After FT exposure, the samples were loaded under a three-point-loading set-up and went through fatigue cycles with a frequency of 15 Hz. The samples were loaded under three different maximum fatigue loads (S_{max}) which accounts for 65%, 75%, and 85% of modulus of rupture value after FT damage. The ratio of the maximum to minimum fatigue load is 0.05. Table 24 summarizes the input parameters to the model proposed in this study.

Table 24 Input parameters to the model (data adopted from [275])

N_{FT} (cycles)	S_{max} (%)	N (number of cycles to failure)					
		Sample 1	Sample 2	Sample 3	Sample 4	Sample 5	Sample 6
50	65	476751	366850	309857	219388	176973	126582
	75	15125	11376	8998	7106	5957	4551
	85	499	382	307	239	221	129
100	65	395761	364675	259315	231356	149630	89975
	75	12472	9591	8236	6195	5169	3061
	85	435	346	271	199	167	136
150	65	389378	296125	251031	179972	125841	74979
	75	13049	8587	5974	5006	4371	3663
	85	411	296	205	187	148	91

Fig. 55 shows the experimental vs. predicted number of fatigue cycles to failure for samples after 50, 100, and 150 cycles of FT exposure. It can be observed that all prediction curves are close to the regression curves. Compared to the regression curves, the prediction curves have flatter slope, which means the prediction slightly overestimates the number of cycles to failure. This could originate from the difference in materials properties between this study and that used in the literature albeit the material strength and aggregate to cement ratio between the two studies are similar.

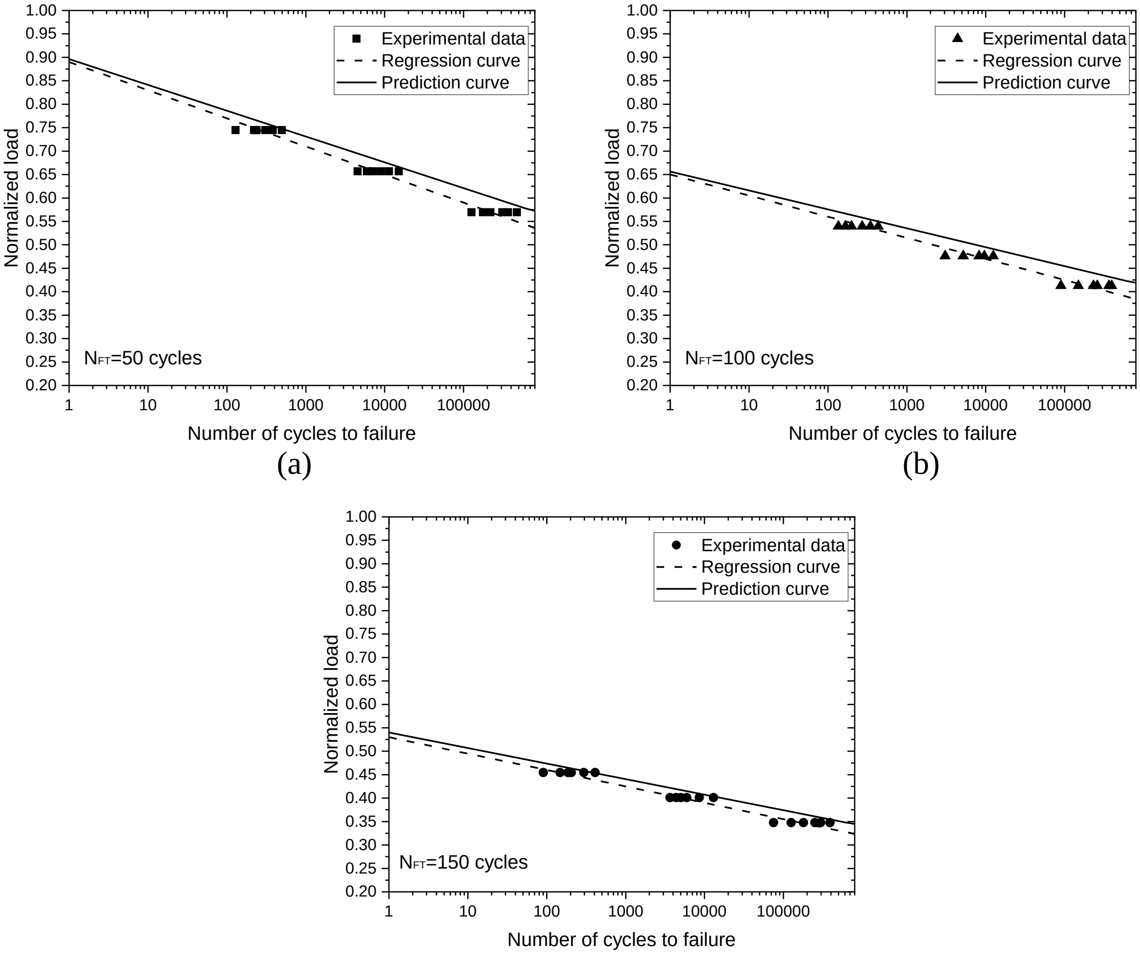

(a) (b)

(c)

Figure 55 Predicted and experimental number of cycles to failure after (a) 50 FT cycles (b) 100 FT cycles (c) 150 FT cycles

To quantify the prediction error in Fig. 55, root means square error (RMSE) for each prediction curve is calculated. The RMSE for samples after 50, 100, and 150 FT cycles is 3.8×10^4, 5.9×10^4, and 2.5×10^4 cycles, respectively. It can be observed that the absolute RMSE value for each prediction curve is large due to the large standard deviation of the cyclic test results itself. This is one of the intrinsic natures of the cyclic test results and has been reported by many researchers [276], [277]. Considering all these limitations, the prediction model can be considered to provide a relatively reasonable prediction of the fatigue life of concrete after FT damage.

Chapter 7 Conclusions and Future Work

The aim of this dissertation is to investigate the individual and combined effect of freeze-thaw, cyclic, and repeated loading performance of samples repaired with different repair materials using both destructive and non-destructive approaches. To achieve this goal, three phases of work were conducted. In Phase I, the effectiveness of the use of surface-treated fibers to improve the crack resistance of the repairs under static loading was studied. In Phase II, the interfacial cracking, modulus of elasticity loss, surface scaling, and bond strength loss of the repaired specimens after FT exposure were studied and analyzed. An empirical model that could be used to predict flexural strength based on NDT measurements was proposed. In Phase III, the hysteretic response, modulus of elasticity loss, and S-N curves of the repaired samples were studied. Additionally, the load-deflection behavior, modulus of elasticity loss, and force-strain behavior of the repair RC under both static and repeated loading conditions were investigated. Theoretical prediction models from the current codes and standards were used to validate the experimental test results.

The key findings from each individual phase are compiled and presented as a whole in this chapter. Considering the limitations of this dissertation work, potential future work is also proposed in this chapter.

7.1 Concluding Remarks and Key Findings

1. The compressive strength of a cementitious composite is affected not only by the amount of SCM but also by the position they occupy in the matrix. By concentrating the SCM on

the parts of the structural element where it is needed the most (boundaries of the reinforcement), an improvement of strength can be achieved by using a fraction of the SCM.

2. Under cyclic, repeated loading, and FT exposure conditions, repair materials with polymers added showed better performance than traditional cementitious repair. After 300 FT cycles, specimens repaired with polymer-modified cementitious mortar showed the lowest mass loss (gained 0.8% mass), a low drop in relative E_{dyn} (5.7%, measured by RFT method), and a relatively small interfacial crack width (maximum 0.0108 mm) amongst all repaired samples. Under cyclic loading, cementitious repair mortar with modified binder (Mix M) also shows the highest number to failure (95,991) and under repeated loading, RC beams repaired in full span with Mix M showed the highest yield and cracking moment resistance. Based on this study, it was found that high strength and bond strength of repair materials could be beneficial to resisting FT and cyclic loading damage.

3. Vibration-based NDT methods are useful tools to detect damage caused by FT, cyclic loading and repeated loading of repaired structures. They include resonant frequency, hammer percussion, and modified chain drag tests methods. The loss in dynamic elastic modulus and resonant frequency measured using NDT methods are aligned with other test observations such as cracking generation, strength loss, surface scaling, residual strain, and displacement.

4. A new bond flexural prediction model was proposed based on NDT measurement. The modulus of elasticity properties determined from the respective resonant frequency test,

hammer percussion, and modified chain drag method has a strong linear correlation with the modulus of rupture values for polymer-modified cementitious mortar (Mix P) and Mix M samples. The coefficient of determination values of regression curves of Mix M and P repaired samples ranged from 0.87 to 0.95.

5. The feasibility of using the Palmgren-Miner rule and Goodman linear model [32] to estimate the fatigue life of repaired structures was confirmed within the context of this study. The formulas proposed by CSA 23.3 can effectively predict the moment resistance of both intact (control) and repaired RC beams.

6. An empirical model that predicted the fatigue service life of FT-damaged concrete structures was proposed in this study. The model was validated using the data provided in previous literature.

7.2 Recommendations for Future Work

1. Future research requires a more comprehensive study on the FT performance of various polymer-modified cementitious mortars of different mix design in repairing concrete structures.
2. A larger standard deviation in E_{dyn} of Mix F repaired samples was observed, as opposed to that of Mix M and Mix P. More number of test samples may be required in the future for Mix F to establish a better relationship between destructive and NDT methods.
3. Future research is required to modify the failure criteria of the to Palmgren-Minder rule to accommodate specimens that may not fail even when the average flexural strength is met.

4. Future research requires using fibers at higher dosages to explicitly study the effectiveness of fiber coating. Additionally, developing and/or modifying existing methods to accurately quantify the improvement in fiber-matrix bond interactions such as using a fiber pullout method can be considered. Conducting 56-day tests to allow for complete interaction between the SCM coated fibers and released lime to take place may also be studied. Future research will also involve marking the fibers and then taking SEM images such that the change in ITZ before and after SCM coating can be identified.
5. More research is needed to study the combined effect of FT and cyclic loading on repaired RC beams.
6. Future research is needed to validate the models proposed for predicting the fatigue service life of repaired samples after FT damage.
7. The main limitation of the current study is the feasibility of the proposed models on predicting the service life of real structures in the field after cyclic and FT damage. It would be also of interest to find out the scale factor that can help apply the current model on the field structures, which will be the future work of this study.

Bibliography

[1] "The 2019 Canada Infrastructure Report Card," p. 56, 2019.

[2] B. Bissonnette, L. Courard, D. W. Fowler, and J.-L. Granju, Eds., *Bonded Cement-Based Material Overlays for the Repair, the Lining or the Strengthening of Slabs or Pavements*. Dordrecht: Springer Netherlands, 2011. doi: 10.1007/978-94-007-1239-3.

[3] M. M. Al-Zahrani, M. Maslehuddin, S. U. Al-Dulaijan, and M. Ibrahim, "Mechanical properties and durability characteristics of polymer- and cement-based repair materials," *Cem. Concr. Compos.*, vol. 25, no. 4, pp. 527–537, May 2003, doi: 10.1016/S0958-9465(02)00092-6.

[4] M. Naderi, "Effects of Cyclic Loading, Freeze-Thaw and Temperature Changes on Shear Bond Strengths of Different Concrete Repair Systems," *J. Adhes.*, vol. 84, no. 9, pp. 743–763, Sep. 2008, doi: 10.1080/00218460802352934.

[5] S. Mindess, J. F. Young, and D. Darwin, *Concrete*, 2nd ed. Upper Saddle River, NJ: Prentice Hall, 2003.

[6] Y. Zheng, Y. Zhou, Y. Zhou, T. Pan, Q. Zhang, and D. Liu, "Cracking behavior of reinforced concrete beams strengthened with CFRP anchorage system under cyclic and monotonic loading," *Eng. Struct.*, vol. 207, p. 110222, Mar. 2020, doi: 10.1016/j.engstruct.2020.110222.

[7] L. Song and Z. Yu, "Fatigue performance of corroded reinforced concrete beams strengthened with CFRP sheets," *Constr. Build. Mater.*, vol. 90, pp. 99–109, Aug. 2015, doi: 10.1016/j.conbuildmat.2015.05.024.

[8] Y. J. Kim and K. A. Harries, "Fatigue behavior of damaged steel beams repaired with CFRP strips," *Eng. Struct.*, vol. 33, no. 5, pp. 1491–1502, May 2011, doi: 10.1016/j.engstruct.2011.01.019.

[9] M. I. Khan and W. Abbass, "Flexural behavior of high-strength concrete beams reinforced with a strain hardening cement-based composite layer," *Constr. Build. Mater.*, vol. 125, pp. 927–935, Oct. 2016, doi: 10.1016/j.conbuildmat.2016.08.132.

[10] O. G. Teixeira, R. H. Geraldo, F. G. da Silva, J. P. Gonçalves, and G. Camarini, "Mortar type influence on mechanical performance of repaired reinforced concrete beams," *Constr. Build. Mater.*, vol. 217, pp. 372–383, Aug. 2019, doi: 10.1016/j.conbuildmat.2019.05.035.

[11] M. Safdar, T. Matsumoto, and K. Kakuma, “Flexural behavior of reinforced concrete beams repaired with ultra-high performance fiber reinforced concrete (UHPFRC),” *Compos. Struct.*, vol. 157, pp. 448–460, Dec. 2016, doi: 10.1016/j.compstruct.2016.09.010.

[12] M. Alexander, A. Bentur, S. Mindess, A. Bentur, and S. Mindess, *Durability of Concrete : Design and Construction*. CRC Press, 2017. doi: 10.1201/9781315118413.

[13] A. Çavdar, “Investigation of freeze–thaw effects on mechanical properties of fiber reinforced cement mortars,” *Compos. Part B Eng.*, vol. 58, pp. 463–472, Mar. 2014, doi: 10.1016/j.compositesb.2013.11.013.

[14] P. J. M. Monteiro, O. Coussy, and D. A. Silva, “Effect of Cryo-Suction and Air Void Transition Layer on Hydraulic Pressure of Freezing Concrete,” *Mater. J.*, vol. 103, no. 2, pp. 136–140, Mar. 2006, doi: 10.14359/15265.

[15] R. A. Helmuth, “Frost action in concrete,” in *Fourth international symposium on the chemistry of cement, Monograph*, 1960, no. 43, pp. 829–833.

[16] J. Mirza, M. S. Mirza, and R. Lapointe, “Laboratory and field performance of polymer-modified cement-based repair mortars in cold climates,” *Constr. Build. Mater.*, vol. 16, no. 6, pp. 365–374, Sep. 2002, doi: 10.1016/S0950-0618(02)00027-2.

[17] Y. Qian, D. Zhang, and T. Ueda, “Interfacial Tensile Bond between Substrate Concrete and Repairing Mortar under Freeze-Thaw Cycles,” *J. Adv. Concr. Technol.*, vol. 14, no. 8, pp. 421–432, 2016, doi: 10.3151/jact.14.421.

[18] S. (Eric) Li, D. G. Geissert, G. C. Frantz, and J. E. Stephens, “Freeze-Thaw Bond Durability of Rapid-Setting Concrete Repair Materials,” *Mater. J.*, vol. 96, no. 2, pp. 242–249, Mar. 1999, doi: 10.14359/451.

[19] A. Garbacz, T. Piotrowski, L. Courard, and L. Kwaśniewski, “On the evaluation of interface quality in concrete repair system by means of impact-echo signal analysis,” *Constr. Build. Mater.*, vol. 134, pp. 311–323, Mar. 2017, doi: 10.1016/j.conbuildmat.2016.12.064.

[20] Ł. Sadowski, J. Hoła, S. Czarnecki, and D. Wang, “Pull-off adhesion prediction of variable thick overlay to the substrate,” *Autom. Constr.*, vol. 85, pp. 10–23, Jan. 2018, doi: 10.1016/j.autcon.2017.10.001.

[21] J. Hoła, Ł. Sadowski, J. Reiner, and S. Stach, “Usefulness of 3D surface roughness parameters for nondestructive evaluation of pull-off adhesion of concrete layers,” *Constr. Build. Mater.*, vol. 84, pp. 111–120, Jun. 2015, doi: 10.1016/j.conbuildmat.2015.03.014.

[22] Ł. Sadowski, S. Czarnecki, and J. Hoła, “Evaluation of the height 3D roughness parameters of concrete substrate and the adhesion to epoxy resin,” *Int. J. Adhes. Adhes.*, vol. 67, pp. 3–13, Jun. 2016, doi: 10.1016/j.ijadhadh.2015.12.019.

[23] J. Hola, L. Sadowski, and K. Schabowicz, “Nondestructive identification of delaminations in concrete floor toppings with acoustic methods,” *Autom. Constr.*, vol. 20, no. 7, pp. 799–807, Nov. 2011, doi: 10.1016/j.autcon.2011.02.002.

[24] A. Garbacz, T. Piotrowski, L. Courard, and L. Kwaśniewski, “On the evaluation of interface quality in concrete repair system by means of impact-echo signal analysis,” *Constr. Build. Mater.*, vol. 134, pp. 311–323, Mar. 2017, doi: 10.1016/j.conbuildmat.2016.12.064.

[25] L. Czarnecki, A. Garbacz, and M. Krystosiak, “On the ultrasonic assessment of adhesion between polymer coating and concrete substrate,” *Cem. Concr. Compos.*, vol. 28, no. 4, pp. 360–369, Apr. 2006, doi: 10.1016/j.cemconcomp.2006.02.017.

[26] I. N. Yadav and K. B. Thapa, “Fatigue damage model of concrete materials,” *Theor. Appl. Fract. Mech.*, vol. 108, p. 102578, Aug. 2020, doi: 10.1016/j.tafmec.2020.102578.

[27] A. Baktheer, J. Hegger, and R. Chudoba, “Enhanced assessment rule for concrete fatigue under compression considering the nonlinear effect of loading sequence,” *Int. J. Fatigue*, vol. 126, pp. 130–142, Sep. 2019, doi: 10.1016/j.ijfatigue.2019.04.027.

[28] K. Keerthana and J. M. Chandra Kishen, “An experimental and analytical study on fatigue damage in concrete under variable amplitude loading,” *Int. J. Fatigue*, vol. 111, pp. 278–288, Jun. 2018, doi: 10.1016/j.ijfatigue.2018.02.014.

[29] A. Alliche, “Damage model for fatigue loading of concrete,” *Int. J. Fatigue*, vol. 26, no. 9, pp. 915–921, Sep. 2004, doi: 10.1016/j.ijfatigue.2004.02.006.

[30] I. El Aghoury and K. Galal, “A fatigue stress-life damage accumulation model for variable amplitude fatigue loading based on virtual target life,” *Eng. Struct.*, vol. 52, pp. 621–628, Jul. 2013, doi: 10.1016/j.engstruct.2013.03.001.

[31] B. Wu, Y. Tang, Z. Li, and K. Tang, “Fatigue damage accumulation modelling of critical components subjected to moving crane loads in reinforced-concrete industrial buildings,” *Eng. Fail. Anal.*, vol. 119, p. 104951, Jan. 2021, doi: 10.1016/j.engfailanal.2020.104951.

[32] A. J. Nieto, J. M. Chicharro, and P. Pintado, “An approximated methodology for fatigue tests and fatigue monitoring of concrete specimens,” *Int. J. Fatigue*, vol. 28, no. 8, pp. 835–842, Aug. 2006, doi: 10.1016/j.ijfatigue.2005.11.004.

[33] C. Signorini, A. Sola, B. Malchiodi, A. Nobili, and A. Gatto, “Failure mechanism of silica coated polypropylene fibres for Fibre Reinforced Concrete (FRC),” *Constr. Build. Mater.*, vol. 236, p. 117549, Mar. 2020, doi: 10.1016/j.conbuildmat.2019.117549.

[34] M. Usman, S. H. Farooq, M. Umair, and A. Hanif, “Axial compressive behavior of confined steel fiber reinforced high strength concrete,” *Constr. Build. Mater.*, vol. 230, p. 117043, Jan. 2020, doi: 10.1016/j.conbuildmat.2019.117043.

[35] R. F. Zollo, “Fiber-reinforced concrete: an overview after 30 years of development,” *Cem. Concr. Compos.*, vol. 19, no. 2, pp. 107–122, Jan. 1997, doi: 10.1016/S0958-9465(96)00046-7.

[36] A. Nobili, L. Lanzoni, and A. M. Tarantino, “Experimental investigation and monitoring of a polypropylene-based fiber reinforced concrete road pavement,” *Constr. Build. Mater.*, vol. 47, pp. 888–895, Oct. 2013, doi: 10.1016/j.conbuildmat.2013.05.077.

[37] L. Lanzoni, A. Nobili, and A. M. Tarantino, “Performance evaluation of a polypropylene-based draw-wired fibre for concrete structures,” *Constr. Build. Mater.*, vol. 28, no. 1, pp. 798–806, Mar. 2012, doi: 10.1016/j.conbuildmat.2011.10.017.

[38] K. L. Scrivener, A. K. Crumbie, and P. Laugesen, “The Interfacial Transition Zone (ITZ) Between Cement Paste and Aggregate in Concrete,” *Interface Sci.*, vol. 12, no. 4, pp. 411–421, Oct. 2004, doi: 10.1023/B:INTS.0000042339.92990.4c.

[39] S. Diamond and J. Huang, “The ITZ in concrete - a different view based on image analysis and SEM observations,” *Cem. Concr. Compos.*, vol. 23, no. 2–3, pp. 179–188, 2001.

[40] P. Mondal, S. P. Shah, and L. D. Marks, “Nanomechanical Properties of Interfacial Transition Zone in Concrete,” in *Nanotechnology in Construction 3*, Z. Bittnar, P. J. M. Bartos, J. Němeček, V. Šmilauer, and J. Zeman, Eds. Berlin, Heidelberg: Springer Berlin Heidelberg, 2009, pp. 315–320. doi: 10.1007/978-3-642-00980-8_42.

[41] “A comparative study on the flexural performance of plasma treated polypropylene fiber reinforced cementitious composites,” *J. Mater. Process. Technol.*, vol. 209, no. 11, pp. 5133–5144, Jun. 2009, doi: 10.1016/j.jmatprotec.2009.02.015.

[42] S. Singh, A. Shukla, and R. Brown, “Pullout behavior of polypropylene fibers from cementitious matrix,” *Cem. Concr. Res.*, vol. 34, no. 10, pp. 1919–1925, Oct. 2004, doi: 10.1016/j.cemconres.2004.02.014.

[43] K.-B. Cheng, J.-Y. Liu, J.-F. Hwang, M.-H. Lee, and C.-C. Hsieh, “Study on the electrical and surface properties of Polyamide 6 woven fabrics using pen-type radio frequency plasma treatment,” *J. Ind. Text.*, vol. 41, no. 3, pp. 185–200, Jan. 2012, doi: 10.1177/1528083711409082.

[44] R. Morent, N. De Geyter, J. Verschuren, K. De Clerck, P. Kiekens, and C. Leys, “Non-thermal plasma treatment of textiles,” *Surf. Coat. Technol.*, vol. 202, no. 14, pp. 3427–3449, Apr. 2008, doi: 10.1016/j.surfcoat.2007.12.027.

[45] J. Trejbal *et al.*, “Deterioration of bonding capacity of plasma-treated polymer fiber reinforcement,” *Cem. Concr. Compos.*, vol. 89, pp. 205–215, May 2018, doi: 10.1016/j.cemconcomp.2018.03.010.

[46] J. P. M. Arias, A. Vazquez, and M. M. Escobar, “Use of sand coating to improve bonding between GFRP bars and concrete,” *J. Compos. Mater.*, vol. 46, no. 18, pp. 2271–2278, Aug. 2012, doi: 10.1177/0021998311431994.

[47] *Sol-Gel Science*. Elsevier, 1990. doi: 10.1016/C2009-0-22386-5.

[48] A. T. Bakera and M. G. Alexander, “Use of metakaolin as supplementary cementitious material in concrete, with focus on durability properties,” *RILEM Tech. Lett.*, vol. 4, pp. 89–102, Nov. 2019, doi: 10.21809/rilemtechlett.2019.94.

[49] E. G. Badogiannis, I. P. Sfikas, D. V. Voukia, K. G. Trezos, and S. G. Tsivilis, “Durability of metakaolin Self-Compacting Concrete,” *Constr. Build. Mater.*, vol. 82, pp. 133–141, May 2015, doi: 10.1016/j.conbuildmat.2015.02.023.

[50] Z. Guo, T. Jiang, J. Zhang, X. Kong, C. Chen, and D. E. Lehman, “Mechanical and durability properties of sustainable self-compacting concrete with recycled concrete aggregate and fly ash, slag and silica fume,” *Constr. Build. Mater.*, vol. 231, p. 117115, Jan. 2020, doi: 10.1016/j.conbuildmat.2019.117115.

[51] R. P. Khatri, V. Sirivivatnanon, and W. Gross, “Effect of different supplementary cementitious materials on mechanical properties of high performance concrete,” *Cem. Concr. Res.*, vol. 25, no. 1, pp. 209–220, Jan. 1995, doi: 10.1016/0008-8846(94)00128-L.

[52] B. Lothenbach, K. Scrivener, and R. D. Hooton, “Supplementary cementitious materials,” *Cem. Concr. Res.*, vol. 41, no. 12, pp. 1244–1256, Dec. 2011, doi: 10.1016/j.cemconres.2010.12.001.

[53] X. Ping and J. J. Beaudoin, “Modification of transition zone microstructure —silica fume coating of aggregate surfaces,” *Cem. Concr. Res.*, vol. 22, no. 4, pp. 597–604, Jul. 1992, doi: 10.1016/0008-8846(92)90010-S.

[54] S. Mindess, “Bonding in Cementitious Composites: How Important is it?,” *MRS Proc.*, vol. 114, p. 3, 1987, doi: 10.1557/PROC-114-3.

[55] H. Cheng-yi and R. F. Feldman, “Hydration reactions in portland cement-silica fume blends,” *Cem. Concr. Res.*, vol. 15, no. 4, pp. 585–592, Jul. 1985, doi: 10.1016/0008-8846(85)90056-0.

[56] Y. S. V. Ganesh, P. Durgaiyya, Ch. Shivanarayana, and D. S. V. Prasad, “Compressive strength of concrete by partial replacement of cement with metakaolin,” Andhra Pradesh, India, 2017, p. 020059. doi: 10.1063/1.4990212.

[57] M. Narmatha and Dr. T. Felixkala, “Meta kaolin –The Best Material for Replacement of Cement in Concrete,” *IOSR J. Mech. Civ. Eng.*, vol. 13, no. 04, pp. 66–71, Apr. 2016, doi: 10.9790/1684-1304016671.

[58] S. H. Chu and A. K. H. Kwan, “Co-addition of metakaolin and silica fume in mortar: effects and advantages,” *Constr. Build. Mater.*, vol. 197, pp. 716–724, Feb. 2019, doi: 10.1016/j.conbuildmat.2018.11.244.

[59] H. Paiva, A. S. Silva, A. Velosa, P. Cachim, and V. M. Ferreira, “Microstructure and hardened state properties on pozzolan-containing concrete,” *Constr. Build. Mater.*, vol. 140, pp. 374–384, Jun. 2017, doi: 10.1016/j.conbuildmat.2017.02.120.

[60] C. S. Poon, S. C. Kou, and L. Lam, “Compressive strength, chloride diffusivity and pore structure of high performance metakaolin and silica fume concrete,” *Constr. Build. Mater.*, vol. 20, no. 10, pp. 858–865, Dec. 2006, doi: 10.1016/j.conbuildmat.2005.07.001.

[61] R. Gupta, "US Patent for Surface Treatment for Concrete Reinforcement Patent (patent # 9,908,813 Issued March 6, 2018) - Justia Patents Search" Accessed: Jan. 26, 2020. [Online]. Available: https://patents.justia.com/patent/9908813

[62] B. Wang, R. Gupta, P. Dias, and T. Bergen, "Coefficient of permeability of cement-based repair materials," p. 8, 2018.

[63] M. M. Al-Zahrani, M. Maslehuddin, S. U. Al-Dulaijan, and M. Ibrahim, "Mechanical properties and durability characteristics of polymer- and cement-based repair materials," *Cem. Concr. Compos.*, vol. 25, no. 4–5, pp. 527–537, May 2003, doi: 10.1016/S0958-9465(02)00092-6.

[64] I. A. B. Hamoud Ahmad Farhan Dehwah Mohammed Maslehuddin, Ghazi Jamil Al-Sulaimani, and Mohammed Hussain Baluch, "Durability Performance of Repaired Reinforced Concrete Beams," *ACI Mater. J.*, vol. 91, no. 2, Mar. 1994, doi: 10.14359/4569.

[65] Fibermesh- Concrete Solutions by Propex, "Fibermesh150-12mmDatasheet.pdf." [Online]. Available: http://www.rindler-gmbh.at/data-rindler/uploads/hotlinks_appfilelink/Fibermesh150-12mmDatasheet.pdf

[66] Burgess Pigment, "CALCINED ALUMINUM SILICATE." [Online]. Available: https://www.burgesspigment.com/tds/burgess-optipozz/?pdf=true

[67] Kryton International Inc., "TDS-Con-Fume.pdf." [Online]. Available: https://www.kryton.com/technical-info/technical-data-sheets/TDS-Con-Fume.pdf

[68] 3M, "Safety Data Sheet: 3M(TM) Super 77(TM) Multipurpose Adhesive (Aerosol)." [Online]. Available: https://multimedia.3m.com/mws/mediawebserver?mwsId=SSSSSuUn_zu8l00x482xN8mvNv70k17zHvu9lxtD7SSSSSS--

[69] C01 Committee, "Test Method for Compressive Strength of Hydraulic Cement Mortars (Using 2-in. or [50-mm] Cube Specimens)," ASTM International. doi: 10.1520/C0109_C0109M-16A.

[70] D01 Committee, "Test Method for Tensile Strength of Chemical-Resistant Mortar, Grouts, and Monolithic Surfacings," ASTM International. doi: 10.1520/C0307-18.

[71] S. Wild, J. M. Khatib, and A. Jones, “Relative strength, pozzolanic activity and cement hydration in superplasticised metakaolin concrete,” *Cem. Concr. Res.*, vol. 26, no. 10, pp. 1537–1544, Oct. 1996, doi: 10.1016/0008-8846(96)00148-2.

[72] P. Dinakar, P. K. Sahoo, and G. Sriram, “Effect of Metakaolin Content on the Properties of High Strength Concrete,” *Int. J. Concr. Struct. Mater.*, vol. 7, no. 3, pp. 215–223, Sep. 2013, doi: 10.1007/s40069-013-0045-0.

[73] S. Wild and J. M. Khatib, “Portlandite consumption in metakaolin cement pastes and mortars,” *Cem. Concr. Res.*, vol. 27, no. 1, pp. 137–146, Jan. 1997, doi: 10.1016/S0008-8846(96)00187-1.

[74] J. M. Khatib, O. Baalbaki, and A. A. ElKordi, “Metakaolin,” in *Waste and Supplementary Cementitious Materials in Concrete*, Elsevier, 2018, pp. 493–511. doi: 10.1016/B978-0-08-102156-9.00015-8.

[75] A. Gameiro *et al.*, “Physical and chemical assessment of lime–metakaolin mortars: Influence of binder:aggregate ratio,” *Cem. Concr. Compos.*, vol. 45, pp. 264–271, Jan. 2014, doi: 10.1016/j.cemconcomp.2013.06.010.

[76] D. Zou *et al.*, “Feasibility of assessing segregation in internally cured mortar based on the variation of properties,” *Constr. Build. Mater.*, vol. 147, pp. 750–757, Aug. 2017, doi: 10.1016/j.conbuildmat.2017.04.196.

[77] X. Qian and Z. Li, “The relationships between stress and strain for high-performance concrete with metakaolin,” *Cem. Concr. Res.*, vol. 31, no. 11, pp. 1607–1611, Nov. 2001, doi: 10.1016/S0008-8846(01)00612-3.

[78] T. A. Hajali Ahmed and Dr. O. M. Ahmed Daoud, “Influence of Polypropylene Fibres on Concrete Properties,” *IOSR J. Mech. Civ. Eng.*, vol. 13, no. 05, pp. 09–20, May 2016, doi: 10.9790/1684-1305060920.

[79] Y. A. Ibrahim, N. R. Maroof, and A. R. Abdulrahman, “Influence of Polypropylene Fibre on Strength and Workability Properties of Cement Mortar,” in *2019 International Engineering Conference (IEC)*, Erbil, Iraq, Jun. 2019, pp. 221–226. doi: 10.1109/IEC47844.2019.8950521.

[80] A. M. Menshaz, M. A. M. Johari, and Z. A. Ahmad, “Characterization of metakaolin treated at different calcination temperatures,” Penang, Malaysia, 2017, p. 020028. doi: 10.1063/1.5005659.

[81] T. Guo, Y. Xie, and X. Weng, “Evaluation of the bond strength of a novel concrete for rapid patch repair of pavements,” *Constr. Build. Mater.*, vol. 186, pp. 790–800, Oct. 2018, doi: 10.1016/j.conbuildmat.2018.08.007.

[82] K. Gadri and A. Guettala, “Evaluation of bond strength between sand concrete as new repair material and ordinary concrete substrate (The surface roughness effect),” *Constr. Build. Mater.*, vol. 157, pp. 1133–1144, Dec. 2017, doi: 10.1016/j.conbuildmat.2017.09.183.

[83] J. Qian, C. You, Q. Wang, H. Wang, and X. Jia, “A method for assessing bond performance of cement-based repair materials,” *Constr. Build. Mater.*, vol. 68, pp. 307–313, Oct. 2014, doi: 10.1016/j.conbuildmat.2014.06.048.

[84] D. R. Morgan, “Compatibility of concrete repair materials and systems,” *Constr. Build. Mater.*, vol. 10, no. 1, pp. 57–67, Feb. 1996, doi: 10.1016/0950-0618(95)00060-7.

[85] D. Cusson and N. Mailvaganam, “Durability of Repair Materials,” *Concr. Int.*, vol. 18, no. 3, pp. 34–38, Mar. 1996.

[86] N. R. C. C. Government of Canada, “CBD-241. Polymer Modified Concrete - NRC-IRC.” http://web.mit.edu/parmstr/Public/NRCan/CanBldgDigests/cbd241_e.html (accessed Apr. 13, 2019).

[87] H. Yu, H. Ma, and K. Yan, “An equation for determining freeze-thaw fatigue damage in concrete and a model for predicting the service life,” *Constr. Build. Mater.*, vol. 137, pp. 104–116, Apr. 2017, doi: 10.1016/j.conbuildmat.2017.01.042.

[88] B. Li, J. Mao, T. Nawa, and T. Han, “Mesoscopic damage model of concrete subjected to freeze-thaw cycles using mercury intrusion porosimetry and differential scanning calorimetry (MIP-DSC),” *Constr. Build. Mater.*, vol. 147, pp. 79–90, Aug. 2017, doi: 10.1016/j.conbuildmat.2017.04.136.

[89] F. Gong and K. Maekawa, “Multi-scale simulation of freeze-thaw damage to RC column and its restoring force characteristics,” *Eng. Struct.*, vol. 156, pp. 522–536, Feb. 2018, doi: 10.1016/j.engstruct.2017.11.066.

[90] K. Ebrahimi, M. J. Daiezadeh, M. Zakertabrizi, F. Zahmatkesh, and A. Habibnejad Korayem, “A review of the impact of micro- and nanoparticles on freeze-thaw durability of hardened concrete: Mechanism perspective,” *Constr. Build. Mater.*, vol. 186, pp. 1105–1113, Oct. 2018, doi: 10.1016/j.conbuildmat.2018.08.029.

[91] L. Liu *et al.*, “Analysis of damage development in cement paste due to ice nucleation at different temperatures,” *Cem. Concr. Compos.*, vol. 53, pp. 1–9, Oct. 2014, doi: 10.1016/j.cemconcomp.2014.06.007.

[92] T. C. Powers, “A Working Hypothesis for Further Studies of Frost Resistance of Concrete,” *J. Proc.*, vol. 41, no. 1, pp. 245–272, Jan. 1945, doi: 10.14359/8684.

[93] P. D. P. Kumar Mehta and P. D. Paulo J. M. Monteiro, *Concrete: Microstructure, Properties, and Materials, Fourth Edition*. McGraw-Hill Education: New York, Chicago, San Francisco, Athens, London, Madrid, Mexico City, Milan, New Delhi, Singapore, Sydney, Toronto, 2014. Accessed: Jan. 10, 2020. [Online]. Available: /content/book/9780071797870

[94] T. C. Powers and R. A. Helmuth, “Theory of Volume Changes in Hardened Portland-cement Paste During Freezing,” *Highw. Res. Board Proc.*, vol. 32, 1953, Accessed: Aug. 17, 2020. [Online]. Available: https://trid.trb.org/view/102368

[95] O. Coussy and P. J. M. Monteiro, “Poroelastic model for concrete exposed to freezing temperatures,” *Cem. Concr. Res.*, vol. 38, no. 1, pp. 40–48, Jan. 2008, doi: 10.1016/j.cemconres.2007.06.006.

[96] Q. Zeng, T. Fen-Chong, P. Dangla, and K. Li, “A study of freezing behavior of cementitious materials by poromechanical approach,” *Int. J. Solids Struct.*, vol. 48, no. 22, pp. 3267–3273, Nov. 2011, doi: 10.1016/j.ijsolstr.2011.07.018.

[97] N. P. Mayercsik, M. Vandamme, and K. E. Kurtis, “Assessing the efficiency of entrained air voids for freeze-thaw durability through modeling,” *Cem. Concr. Res.*, vol. 88, pp. 43–59, Oct. 2016, doi: 10.1016/j.cemconres.2016.06.004.

[98] O. Coussy, “A general theory of thermoporoelastoplasticity for saturated porous materials,” *Transp. Porous Media*, vol. 4, no. 3, pp. 281–293, Jun. 1989, doi: 10.1007/BF00138040.

[99] O. Coussy, *Poromechanics*. John Wiley & Sons, 2004.

[100] Y. Dong, C. Su, P. Qiao, and L. Sun, “A thermal-hydraulic-mechanical coupling model for freezing process simulation of cementitious materials with entrained air voids,” *Constr. Build. Mater.*, vol. 243, p. 118253, May 2020, doi: 10.1016/j.conbuildmat.2020.118253.

[101] W. Zhou, C. Zhao, X. Liu, X. Chang, and C. Feng, “Mesoscopic simulation of thermo-mechanical behaviors in concrete under frost action,” *Constr. Build. Mater.*, vol. 157, pp. 117–131, Dec. 2017, doi: 10.1016/j.conbuildmat.2017.09.009.

[102] S. H. Smith, C. Qiao, P. Suraneni, K. E. Kurtis, and W. J. Weiss, “Service-life of concrete in freeze-thaw environments: Critical degree of saturation and calcium oxychloride formation,” *Cem. Concr. Res.*, vol. 122, pp. 93–106, Aug. 2019, doi: 10.1016/j.cemconres.2019.04.014.

[103] J. J. Assaad, F. Hamzeh, and B. Hamad, “Qualitative assessment of interfacial bonding in 3D printing concrete exposed to frost attack,” *Case Stud. Constr. Mater.*, vol. 13, p. e00357, Dec. 2020, doi: 10.1016/j.cscm.2020.e00357.

[104] M. Wang *et al.*, “Research on the mechanism of polymer latex modified cement,” *Constr. Build. Mater.*, vol. 111, pp. 710–718, May 2016, doi: 10.1016/j.conbuildmat.2016.02.117.

[105] L. K. Aggarwal, P. C. Thapliyal, and S. R. Karade, “Properties of polymer-modified mortars using epoxy and acrylic emulsions,” *Constr. Build. Mater.*, vol. 21, no. 2, pp. 379–383, Feb. 2007, doi: 10.1016/j.conbuildmat.2005.08.007.

[106] M. Ramli and A. Akhavan Tabassi, “Effects of polymer modification on the permeability of cement mortars under different curing conditions: A correlational study that includes pore distributions, water absorption and compressive strength,” *Constr. Build. Mater.*, vol. 28, no. 1, pp. 561–570, Mar. 2012, doi: 10.1016/j.conbuildmat.2011.09.004.

[107] A. A. P. Mansur, D. B. Santos, and H. S. Mansur, “A microstructural approach to adherence mechanism of poly(vinyl alcohol) modified cement systems to ceramic tiles,” *Cem. Concr. Res.*, vol. 37, no. 2, pp. 270–282, Feb. 2007, doi: 10.1016/j.cemconres.2006.11.011.

[108] Z. Yang, X. Shi, A. T. Creighton, and M. M. Peterson, “Effect of styrene–butadiene rubber latex on the chloride permeability and microstructure of Portland cement mortar,” *Constr. Build. Mater.*, vol. 23, no. 6, pp. 2283–2290, Jun. 2009, doi: 10.1016/j.conbuildmat.2008.11.011.

[109] A. Momayez, M. R. Ehsani, A. A. Ramezanianpour, and H. Rajaie, “Comparison of methods for evaluating bond strength between concrete substrate and repair materials,” *Cem. Concr. Res.*, vol. 35, no. 4, pp. 748–757, Apr. 2005, doi: 10.1016/j.cemconres.2004.05.027.

[110] ASTM International, “C1583/C1583M-13 Standard Test Method for Tensile Strength of Concrete Surfaces and the Bond Strength or Tensile Strength of Concrete Repair and Overlay Materials by Direct Tension (Pull-off Method).,” ASTM International, 2013. Accessed: May 11, 2019. [Online]. Available: https://doi.org/10.1520/C1583_C1583M-13

[111] C. Zanotti and N. Randl, “Are concrete-concrete bond tests comparable?,” *Cem. Concr. Compos.*, vol. 99, pp. 80–88, May 2019, doi: 10.1016/j.cemconcomp.2019.02.012.

[112] S. H. Abo Sabah, M. H. Hassan, N. Muhamad Bunnori, and M. A. Megat Johari, “Bond strength of the interface between normal concrete substrate and GUSMRC repair material overlay,” *Constr. Build. Mater.*, vol. 216, pp. 261–271, Aug. 2019, doi: 10.1016/j.conbuildmat.2019.04.270.

[113] ASTM International, “C882/C882M-13a Standard Test Method for Bond Strength of Epoxy-Resin Systems Used With Concrete By Slant Shear.,” ASTM International, 2013. Accessed: May 11, 2019. [Online]. Available: https://doi.org/10.1520/C0882_C0882M-13A

[114] R. Saldanha, E. Júlio, D. Dias-da-Costa, and P. Santos, “A modified slant shear test designed to enforce adhesive failure,” *Constr. Build. Mater.*, vol. 41, pp. 673–680, Apr. 2013, doi: 10.1016/j.conbuildmat.2012.12.053.

[115] ASTM International, “C1383-15 Standard Test Method for Measuring the P-Wave Speed and the Thickness of Concrete Plates Using the Impact-Echo Method.,” ASTM International, 2015. [Online]. Available: https://doi.org/10.1520/C1383-15

[116] J.-M. Lin and M. Sansalone, “Impact-Echo Studies of Interfacial Bond Quality in Concrete: Part l-Effects of Unbonded Fraction of Area,” *Mater. J.*, vol. 93, no. 3, pp. 223–232, May 1996, doi: 10.14359/9806.

[117] J.-M. Lin, M. Sansalone, and R. Poston, “Impact-Echo Studies of Interfacial Bond Quality in Concrete: Part II - Effects of Bond Tensile Strength,” *Mater. J.*, vol. 93, no. 4, pp. 318–326, Jul. 1996, doi: 10.14359/9817.

[118] Ł. Sadowski, “Non-destructive identification of pull-off adhesion between concrete layers,” *Autom. Constr.*, vol. 57, pp. 146–155, Sep. 2015, doi: 10.1016/j.autcon.2015.06.004.

[119] ASTM International, “C1740-16 Standard Practice for Evaluating the Condition of Concrete Plates Using the Impulse-Response Method,” ASTM International, 2016. [Online]. Available: https://doi.org/10.1520/C1740-16

[120] J. Hola, L. Sadowski, and K. Schabowicz, “Non-Destructive Evaluation of the Concrete Floor Quality Using Impulse Response S’Mash And Impact-Echo Methods,” p. 8, 2008.

[121] Ł. Sadowski, “Methodology of the assessment of the interlayer bond in concrete composites using NDT methods,” *J. Adhes. Sci. Technol.*, vol. 32, no. 2, pp. 139–157, Jan. 2018, doi: 10.1080/01694243.2017.1343426.

[122] A. G. Davis and B. H. Hertlein, “Nondestructive testing of concrete chimneys and other structures,” in *Nondestructive Evaluation of Aging Structures and Dams*, May 1995, vol. 2457, pp. 129–136. doi: 10.1117/12.209386.

[123] S. Sajid and L. Chouinard, “Impulse response test for condition assessment of concrete: A review,” *Constr. Build. Mater.*, vol. 211, pp. 317–328, Jun. 2019, doi: 10.1016/j.conbuildmat.2019.03.174.

[124] S. Blaney and R. Gupta, “Sounding of subsurface concrete defects using frequency response of flexural vibration,” *Cem. Concr. Compos.*, vol. 92, pp. 155–164, Sep. 2018, doi: 10.1016/j.cemconcomp.2018.06.006.

[125] A. C. I. Committee 211, “Standard Practice for Selecting Proportions for Normal, Heavyweight, and Mass Concrete:(ACI 211.1-91),” 1991.

[126] ASTM International, “C136/C136M-19 Standard Test Method for Sieve Analysis of Fine and Coarse Aggregates,” 2019. [Online]. Available: https://doi.org/10.1520/C0136_C0136M-19

[127] ASTM International, “C494/C494M-19 Standard Specification for Chemical Admixtures for Concrete,” 2019. [Online]. Available: https://doi.org/10.1520/C0494_C0494M-19

[128] ASTM International, “C260/C260M-10a(2016) Standard Specification for Air-Entraining Admixtures for Concrete,” 2016. [Online]. Available: https://doi.org/10.1520/C0260_C0260M-10AR16

[129] R. Bajaj, B. Wang, and R. Gupta, “Characterization of Enhanced ITZ in Engineered Polypropylene Fibers for Bond Improvement,” *J. Compos. Sci.*, vol. 4, no. 2, Art. no. 2, Jun. 2020, doi: 10.3390/jcs4020053.

[130] ASTM International, “C143/C143M-15a Standard Test Method for Slump of Hydraulic-Cement Concrete. Retrieved from,” ASTM International, 2015. Accessed: Jun. 15, 2019. [Online]. Available: https://doi.org/10.1520/C0143_C0143M-15A

[131] ASTM International, “C231/C231M-17a Standard Test Method for Air Content of Freshly Mixed Concrete by the Pressure Method.,” ASTM International, 2017. Accessed: Jun. 15, 2019. [Online]. Available: https://doi.org/10.1520/C0231_C0231M-17A

[132] ASTM International, “C39/C39M-18 Standard Test Method for Compressive Strength of Cylindrical Concrete Specimens,” ASTM International, 2018. Accessed: Jun. 15, 2019. [Online]. Available: https://doi.org/10.1520/C0039_C0039M-18

[133] B. Wang, R. Gupta, P. Dias, and T. Bergen, “Coefficient of permeability of cement-based repair materials,” presented at the 1st International Conference on New Horizons in Civil Engineering, Victoria, Canada, Apr. 2018.

[134] B. Wang and R. Gupta, “Correlation of Electrical Conductivity, Compressive Strength, and Permeability of Repair Materials,” *Mater. J.*, vol. 117, no. 2, pp. 53–63, Mar. 2020, doi: 10.14359/51722396.

[135] K. F. von Fay, *Guide to Concrete Repair*. U.S. Department of the Interior, Bureau of Reclamation, Technical Service Center, 2015.

[136] P. Winkler, “Selecting and Specifying Concrete Surface Preparation for Sealers, Coatings, Polymer Overlays, and Concrete Repair,” p. 3.

[137] ASTM International, “C666/C666M-15 Standard Test Method for Resistance of Concrete to Rapid Freezing and Thawing.,” ASTM International, 2015. Accessed: Jun. 09, 2019. [Online]. Available: https://doi.org/10.1520/C0666_C0666M-15

[138] Zhu Jinying and Popovics John S., “Imaging Concrete Structures Using Air-Coupled Impact-Echo,” *J. Eng. Mech.*, vol. 133, no. 6, pp. 628–640, Jun. 2007, doi: 10.1061/(ASCE)0733-9399(2007)133:6(628).

[139] ASTM International, “D4580-03 Standard Practice for Measuring Delaminations in Concrete Bridge Decks by Sounding.,” ASTM International, 2003. Accessed: Jun. 09, 2019. [Online]. Available: https://doi.org/10.1520/D4580-03

[140] ASTM International, “C215-14 Standard Test Method for Fundamental Transverse, Longitudinal, and Torsional Resonant Frequencies of Concrete Specimens.,” ASTM International, 2014. Accessed: Jun. 09, 2019. [Online]. Available: https://doi.org/10.1520/C0215-14

[141] ASTM International, “C1609/C1609M-19 Standard Test Method for Flexural Performance of Fiber-Reinforced Concrete (Using Beam With Third-Point Loading).,” ASTM International, 2019. Accessed: Jun. 09, 2019. [Online]. Available: https://doi.org/10.1520/C1609_C1609M-19

[142] J. L. Devore, *Probability and statistics for engineering and the sciences*, 3rd ed. Pacific Grove, Calif: Brooks/Cole Pub. Co, 1991.

[143] ASTM International, “C672/C672M-12 Standard Test Method for Scaling Resistance of Concrete Surfaces Exposed to Deicing Chemicals.,” ASTM International, 2012. doi: 10.1520/C0672_C0672M-12.

[144] P. Zhang, D. Li, Y. Qiao, S. Zhang, C. Sun, and T. Zhao, “Effect of Air Entrainment on the Mechanical Properties, Chloride Migration, and Microstructure of Ordinary Concrete and Fly Ash Concrete,” *J. Mater. Civ. Eng.*, vol. 30, no. 10, p. 04018265, Oct. 2018, doi: 10.1061/(ASCE)MT.1943-5533.0002456.

[145] J. H. Hu, Y. Kuang, T. Zhou, and F. Zhao, “Influence of Air Entraining Agent on Strength and Microstructure Properties of Cemented Paste Backfill,” *IEEE Access*, vol. 7, pp. 140899–140907, 2019, doi: 10.1109/ACCESS.2019.2942360.

[146] Z. Zhou and P. Qiao, “Durability of ultra-high performance concrete in tension under cold weather conditions,” *Cem. Concr. Compos.*, vol. 94, pp. 94–106, Nov. 2018, doi: 10.1016/j.cemconcomp.2018.08.019.

[147] W. W. Jr, S. P. Timoshenko, and D. H. Young, *Vibration Problems in Engineering*. John Wiley & Sons, 1990.

[148] H. Sun, J. Zhu, and S. Ham, “Acoustic evaluation of concrete delaminations using ball-chain impact excitation,” *J. Acoust. Soc. Am.*, vol. 141, no. 5, pp. EL477–EL481, May 2017, doi: 10.1121/1.4983343.

[149] O. Karahan and C. D. Atiş, “The durability properties of polypropylene fiber reinforced fly ash concrete,” *Mater. Des.*, vol. 32, no. 2, pp. 1044–1049, Feb. 2011, doi: 10.1016/j.matdes.2010.07.011.

[150] A. E. Richardson, K. A. Coventry, and S. Wilkinson, “Freeze/thaw durability of concrete with synthetic fibre additions,” *Cold Reg. Sci. Technol.*, vol. 83–84, pp. 49–56, Dec. 2012, doi: 10.1016/j.coldregions.2012.06.006.

[151] C. Wang and F. Chen, “Durability of Polypropylene Fiber Concrete Exposed to Freeze-Thaw Cycles with Deicing Salts,” presented at the 2019 International Conference on Electronical, Mechanical and Materials Engineering (ICE2ME 2019), Mar. 2019. doi: 10.2991/ice2me-19.2019.46.

[152] A. Richardson, “Polypropylene fibres in concrete with regard to durability,” *Struct. Surv.*, vol. 21, no. 2, pp. 87–94, Jan. 2003, doi: 10.1108/02630800310479089.

[153] M. L. Allan and L. E. Kukacka, “Strength and durability of polypropylene fibre reinforced grouts,” *Cem. Concr. Res.*, vol. 25, no. 3, pp. 511–521, Apr. 1995, doi: 10.1016/0008-8846(95)00040-J.

[154] C. Jiang, K. Fan, F. Wu, and D. Chen, “Experimental study on the mechanical properties and microstructure of chopped basalt fibre reinforced concrete,” *Mater. Des.*, vol. 58, pp. 187–193, Jun. 2014, doi: 10.1016/j.matdes.2014.01.056.

[155] Huadong Wu and M. Siegel, “Correlation of accelerometer and microphone data in the ‘coin tap test,’” *IEEE Trans. Instrum. Meas.*, vol. 49, no. 3, pp. 493–497, Jun. 2000, doi: 10.1109/19.850382.

[156] W. Sun, Y. M. Zhang, H. D. Yan, and R. Mu, “Damage and damage resistance of high strength concrete under the action of load and freeze-thaw cycles,” *Cem. Concr. Res.*, vol. 29, no. 9, pp. 1519–1523, Sep. 1999, doi: 10.1016/S0008-8846(99)00097-6.

[157] A. Torres, A. Ramos-Cañón, L. Prada Sarmiento, and M. Botía-Díaz, “Mechanical behavior of concrete cold joints,” *Rev. Ing. Construccion*, vol. 31, pp. 151–162, Dec. 2016.

[158] S. G. Shah and J. M. Chandra Kishen, “Fracture behavior of concrete–concrete interface using acoustic emission technique,” *Eng. Fract. Mech.*, vol. 77, no. 6, pp. 908–924, Apr. 2010, doi: 10.1016/j.engfracmech.2010.01.018.

[159] S. G. Shah and J. M. Chandra Kishen, “Fracture Properties of Concrete–Concrete Interfaces Using Digital Image Correlation,” *Exp. Mech.*, vol. 51, no. 3, pp. 303–313, Mar. 2011, doi: 10.1007/s11340-010-9358-y.

[160] A. Akhavan, S.-M.-H. Shafaatian, and F. Rajabipour, “Quantifying the effects of crack width, tortuosity, and roughness on water permeability of cracked mortars,” *Cem. Concr. Res.*, vol. 42, no. 2, pp. 313–320, Feb. 2012, doi: 10.1016/j.cemconres.2011.10.002.

[161] M. A. Issa, A. M. Hammad, and A. Chudnovsky, “Correlation between crack tortuosity and fracture toughness in cementitious material,” *Int. J. Fract.*, vol. 60, no. 2, pp. 97–105, Mar. 1993, doi: 10.1007/BF00012438.

[162] B. Kabiri Far and C. Zanotti, “Concrete–Concrete Bond in Mode-I: A study on the Synergistic Effect of Surface Roughness and Fiber Reinforcement,” *Appl. Sci.*, vol. 9, no. 12, p. 2556, Jun. 2019, doi: 10.3390/app9122556.

[163] *AS 3600-2009, Concrete structures, Standards Australia 2009*.

[164] ACI Committee 318 and American Concrete Institute (ACI), *Building code requirements for structural concrete (ACI 318-14): an ACI standard and commentary on building code requerements for structural concrete (ACI 318R-14) : an ACI report*. Farmington Hills, Michigan: American Concrete Institute, ACI, 2014.

[165] *CSA Technical Committee. Reinforced Concrete Design. A23.3-04. Design of concrete structures, Rexdale, Ontario. Canadian Standards Association; 2004*.

[166] “CAN/CSA-A23.3-04 (R2010).” https://www.scc.ca/en/standardsdb/standards/20358 (accessed May 13, 2020).

[167] Y. Zhou, J. Gao, Z. Sun, and W. Qu, “A fundamental study on compressive strength, static and dynamic elastic moduli of young concrete,” *Constr. Build. Mater.*, vol. 98, pp. 137–145, Nov. 2015, doi: 10.1016/j.conbuildmat.2015.08.110.

[168] R. Bassim and M. Issa, “Dynamic- and Static-Elastic Moduli and Strength Properties of Early-Age Portland Cement Concrete Pavement Mixtures,” *J. Mater. Civ. Eng.*, vol. 32, no. 5, p. 04020066, May 2020, doi: 10.1061/(ASCE)MT.1943-5533.0003089.

[169] K. Z. Hanjari, P. Utgenannt, and K. Lundgren, “Experimental study of the material and bond properties of frost-damaged concrete,” *Cem. Concr. Res.*, vol. 41, no. 3, pp. 244–254, Mar. 2011, doi: 10.1016/j.cemconres.2010.11.007.

[170] K. Wang, D. C. Jansen, S. P. Shah, and A. F. Karr, “Permeability study of cracked concrete,” *Cem. Concr. Res.*, vol. 27, no. 3, pp. 381–393, Mar. 1997, doi: 10.1016/S0008-8846(97)00031-8.

[171] M. M. Al-Zahrani, M. Maslehuddin, S. U. Al-Dulaijan, and M. Ibrahim, “Mechanical properties and durability characteristics of polymer- and cement-based repair materials,” *Cem.*

Concr. Compos., vol. 25, no. 4, pp. 527–537, May 2003, doi: 10.1016/S0958-9465(02)00092-6.

[172] A. M. Vaysburd and P. H. Emmons, “How to make today’s repairs durable for tomorrow — corrosion protection in concrete repair,” *Constr. Build. Mater.*, vol. 14, no. 4, pp. 189–197, Jun. 2000, doi: 10.1016/S0950-0618(00)00022-2.

[173] J. J. Assaad, “Development and use of polymer-modified cement for adhesive and repair applications,” *Constr. Build. Mater.*, vol. 163, pp. 139–148, Feb. 2018, doi: 10.1016/j.conbuildmat.2017.12.103.

[174] K. Ye and J. Ji, “Current, wave, wind and interaction induced dynamic response of a 5 MW spar-type offshore direct-drive wind turbine,” *Eng. Struct.*, vol. 178, pp. 395–409, Jan. 2019, doi: 10.1016/j.engstruct.2018.10.023.

[175] M. K. Lee and B. I. G. Barr, “An overview of the fatigue behaviour of plain and fibre reinforced concrete,” *Cem. Concr. Compos.*, vol. 26, no. 4, pp. 299–305, May 2004, doi: 10.1016/S0958-9465(02)00139-7.

[176] S. Mindess, J. F. Young, and D. Darwin, *Concrete*, 2nd ed. Upper Saddle River, NJ: Prentice Hall, 2003.

[177] M. Saito and S. Lmai, “Direct Tensile Fatigue of Concrete by the Use of Friction Grips,” *J. Proc.*, vol. 80, no. 5, pp. 431–438, Sep. 1983, doi: 10.14359/10867.

[178] M. Kurumatani, Y. Soma, and K. Terada, “Simulations of cohesive fracture behavior of reinforced concrete by a fracture-mechanics-based damage model,” *Eng. Fract. Mech.*, vol. 206, pp. 392–407, Feb. 2019, doi: 10.1016/j.engfracmech.2018.12.006.

[179] A. Hillerborg, M. Modéer, and P.-E. Petersson, “Analysis of crack formation and crack growth in concrete by means of fracture mechanics and finite elements,” *Cem. Concr. Res.*, vol. 6, no. 6, pp. 773–781, Nov. 1976, doi: 10.1016/0008-8846(76)90007-7.

[180] K. Keerthana and J. M. C. Kishen, “Micromechanics of fracture and failure in concrete under monotonic and fatigue loadings,” *Mech. Mater.*, vol. 148, p. 103490, Sep. 2020, doi: 10.1016/j.mechmat.2020.103490.

[181] J. Mergheim, E. Kuhl, and P. Steinmann, “A finite element method for the computational modelling of cohesive cracks,” *Int. J. Numer. Methods Eng.*, vol. 63, no. 2, pp. 276–289, 2005, doi: 10.1002/nme.1286.

[182] J. F. Unger, S. Eckardt, and C. Könke, “Modelling of cohesive crack growth in concrete structures with the extended finite element method,” *Comput. Methods Appl. Mech. Eng.*, vol. 196, no. 41, pp. 4087–4100, Sep. 2007, doi: 10.1016/j.cma.2007.03.023.

[183] B. Zhang and K. Wu, “Residual fatigue strength and stiffness of ordinary concrete under bending,” *Cem. Concr. Res.*, vol. 27, no. 1, pp. 115–126, Jan. 1997, doi: 10.1016/S0008-8846(96)00183-4.

[184] X. Chen, J. Bu, X. Fan, J. Lu, and L. Xu, “Effect of loading frequency and stress level on low cycle fatigue behavior of plain concrete in direct tension,” *Constr. Build. Mater.*, vol. 133, pp. 367–375, Feb. 2017, doi: 10.1016/j.conbuildmat.2016.12.085.

[185] K. M. Simon and J. M. Chandra Kishen, “A multiscale approach for modeling fatigue crack growth in concrete,” *Int. J. Fatigue*, vol. 98, pp. 1–13, May 2017, doi: 10.1016/j.ijfatigue.2017.01.007.

[186] J. Fan, D. Jiang, J. Chen, W. Liu, W. Tiedeu Ngaha, and J. Chen, “Fatigue performance of ordinary concrete under discontinuous cyclic loading,” *Constr. Build. Mater.*, vol. 166, pp. 974–981, Mar. 2018, doi: 10.1016/j.conbuildmat.2018.01.115.

[187] R. C. McClung and H. Sehitoglu, “On the finite element analysis of fatigue crack closure—1. Basic modeling issues,” *Eng. Fract. Mech.*, vol. 33, no. 2, pp. 237–252, Jan. 1989, doi: 10.1016/0013-7944(89)90027-1.

[188] J.-Q. Xiao, D.-X. Ding, F.-L. Jiang, and G. Xu, “Fatigue damage variable and evolution of rock subjected to cyclic loading,” *Int. J. Rock Mech. Min. Sci.*, vol. 47, no. 3, pp. 461–468, Apr. 2010, doi: 10.1016/j.ijrmms.2009.11.003.

[189] M. A. Miner, “Cumulative damage in fatigue,” *J Appl Mech*, vol. 12, no. 3, pp. A159–A164, 1945.

[190] S. G. Shah, S. Ray, and J. M. Chandra Kishen, “Fatigue crack propagation at concrete–concrete bi-material interfaces,” *Int. J. Fatigue*, vol. 63, pp. 118–126, Jun. 2014, doi: 10.1016/j.ijfatigue.2014.01.015.

[191] S. G. Shah and J. M. C. Kishen, “Nonlinear fracture properties of concrete–concrete interfaces,” *Mech. Mater.*, vol. 42, no. 10, pp. 916–931, Oct. 2010, doi: 10.1016/j.mechmat.2010.08.002.

[192] K. C. G. Ong, P. Paramasivam, and M. Subramanian, “Cyclic Behavior of Steel-Fiber Mortar Overlaid Concrete Beams,” *J. Mater. Civ. Eng.*, vol. 9, no. 1, pp. 21–28, Feb. 1997, doi: 10.1061/(ASCE)0899-1561(1997)9:1(21).

[193] A. Ramachandra Murthy, B. L. Karihaloo, P. Vindhya Rani, and D. Shanmuga Priya, “Fatigue behaviour of damaged RC beams strengthened with ultra high performance fibre reinforced concrete,” *Int. J. Fatigue*, vol. 116, pp. 659–668, Nov. 2018, doi: 10.1016/j.ijfatigue.2018.06.046.

[194] P. Ganesh and A. Ramachandra Murthy, “Fatigue performance of damaged RC beams rehabilitated with GGBS based ultra high performance concrete,” *Int. J. Fatigue*, vol. 138, p. 105707, Sep. 2020, doi: 10.1016/j.ijfatigue.2020.105707.

[195] B. Wang and R. Gupta, “Analyzing bond-deterioration during freeze-thaw exposure in cement-based repairs using non-destructive methods,” *Cem. Concr. Compos.*, vol. 115, p. 103830, Jan. 2021, doi: 10.1016/j.cemconcomp.2020.103830.

[196] “ACI PRC-215-92: Considerations for Design of Concrete Structures Subjected to Fatigue Loading (Reapproved 1997).” https://www.concrete.org/store/productdetail.aspx?ItemID=21592&Format=DOWNLOAD&Language=English&Units=US_AND_METRIC (accessed Apr. 06, 2022).

[197] ASTM International, “C496/C496M-17 Standard Test Method for Splitting Tensile Strength of Cylindrical Concrete Specimens,” 2017. [Online]. Available: https://doi.org/10.1520/C0496_C0496M-17

[198] D. Figueira, C. Sousa, R. Calçada, and A. S. Neves, “Push-Off Tests in the Study of Cyclic Behavior of Interfaces between Concretes Cast at Different Times,” *J. Struct. Eng.*, vol. 142, no. 1, p. 04015101, Jan. 2016, doi: 10.1061/(ASCE)ST.1943-541X.0001364.

[199] S. Feng, H. Xiao, and J. Geng, “Bond strength between concrete substrate and repair mortar: Effect of fibre stiffness and substrate surface roughness,” *Cem. Concr. Compos.*, vol. 114, p. 103746, Nov. 2020, doi: 10.1016/j.cemconcomp.2020.103746.

[200] Y. Zhang, P. Zhu, Z. Liao, and L. Wang, “Interfacial bond properties between normal strength concrete substrate and ultra-high performance concrete as a repair material,” *Constr. Build. Mater.*, vol. 235, p. 117431, Feb. 2020, doi: 10.1016/j.conbuildmat.2019.117431.

[201] S. Feng, H. Xiao, and H. Li, “Comparative studies of the effect of ultrahigh-performance concrete and normal concrete as repair materials on interfacial bond properties and microstructure,” *Eng. Struct.*, vol. 222, p. 111122, Nov. 2020, doi: 10.1016/j.engstruct.2020.111122.

[202] G. Peng, D. Niu, X. Hu, B. Pan, and S. Zhong, “Experimental study of the interfacial bond strength between cementitious grout and normal concrete substrate,” *Constr. Build. Mater.*, vol. 273, p. 122057, Mar. 2021, doi: 10.1016/j.conbuildmat.2020.122057.

[203] S. Feng, H. Xiao, R. Zhang, and C. Yang, “Bond performance between substrate concrete and repair mortar: Effect of carbon fibre and expansive agent,” *Constr. Build. Mater.*, vol. 250, p. 118830, Jul. 2020, doi: 10.1016/j.conbuildmat.2020.118830.

[204] K. Rashid *et al.*, “Experimental investigation of the bond strength between new to old concrete using different adhesive layers,” *Constr. Build. Mater.*, vol. 249, p. 118798, Jul. 2020, doi: 10.1016/j.conbuildmat.2020.118798.

[205] C. Zanotti, N. Banthia, and G. Plizzari, “A study of some factors affecting bond in cementitious fiber reinforced repairs,” *Cem. Concr. Res.*, vol. 63, pp. 117–126, Sep. 2014, doi: 10.1016/j.cemconres.2014.05.008.

[206] E. N. B. S. Júlio, F. A. B. Branco, and V. D. Silva, “Concrete-to-concrete bond strength. Influence of the roughness of the substrate surface,” *Constr. Build. Mater.*, vol. 18, no. 9, pp. 675–681, Nov. 2004, doi: 10.1016/j.conbuildmat.2004.04.023.

[207] S. Austin, P. Robins, and Y. Pan, “Shear bond testing of concrete repairs,” *Cem. Concr. Res.*, vol. 29, no. 7, pp. 1067–1076, Jul. 1999, doi: 10.1016/S0008-8846(99)00088-5.

[208] P.-W. Chen, X. Fu, and D. D. L. Chung, “Improving the bonding between old and new concrete by adding carbon fibers to the new concrete,” *Cem. Concr. Res.*, vol. 25, no. 3, pp. 491–496, Apr. 1995, doi: 10.1016/0008-8846(95)00037-D.

[209] A. Valikhani, A. J. Jahromi, I. M. Mantawy, and A. Azizinamini, “Experimental evaluation of concrete-to-UHPC bond strength with correlation to surface roughness for repair application,” *Constr. Build. Mater.*, vol. 238, p. 117753, Mar. 2020, doi: 10.1016/j.conbuildmat.2019.117753.

[210] M. Arezoumandi, C. Wirkman, and J. S. Volz, “Performance of Fiber-reinforced Self-consolidating Concrete for Repair of Bridge Substructures,” *Structures*, vol. 15, pp. 320–328, Aug. 2018, doi: 10.1016/j.istruc.2018.07.015.

[211] C. Zanotti, P. H. R. Borges, A. Bhutta, and N. Banthia, “Bond strength between concrete substrate and metakaolin geopolymer repair mortar: Effect of curing regime and PVA fiber reinforcement,” *Cem. Concr. Compos.*, vol. 80, pp. 307–316, Jul. 2017, doi: 10.1016/j.cemconcomp.2016.12.014.

[212] L. Göbel, C. Bos, R. Schwaiger, A. Flohr, and A. Osburg, “Micromechanics-based investigation of the elastic properties of polymer-modified cementitious materials using nanoindentation and semi-analytical modeling,” *Cem. Concr. Compos.*, vol. 88, pp. 100–114, Apr. 2018, doi: 10.1016/j.cemconcomp.2018.01.010.

[213] M. Fadadu, N. Vadher, V. Trivedi, M. Mungule, and K. K. R. Iyer, “A comparative study on stress-strain response and associated hysteresis for conventional and PET macro-reinforced concrete,” *Constr. Build. Mater.*, vol. 264, p. 120534, Dec. 2020, doi: 10.1016/j.conbuildmat.2020.120534.

[214] S.-K. Park, “Flexural behavior of reinforced concrete beams with cementitious repair materials,” *Mater. Struct.*, vol. 38, no. 277, pp. 329–334, Feb. 2005, doi: 10.1617/14051.

[215] X. Hui-cai, L. Geng-ying, and X. Guang-jing, “Microstructure model of the interfacial zone between fresh and old concrete,” *J. Wuhan Univ. Technol.-Mater Sci Ed*, vol. 17, no. 4, pp. 64–68, Dec. 2002, doi: 10.1007/BF02838421.

[216] S. Goel, S. P. Singh, and P. Singh, “Flexural fatigue strength and failure probability of Self Compacting Fibre Reinforced Concrete beams,” *Eng. Struct.*, vol. 40, pp. 131–140, Jul. 2012, doi: 10.1016/j.engstruct.2012.02.035.

[217] S. P. Singh and S. K. Kaushik, “Flexural Fatigue Analysis of Steel Fiber-Reinforced Concrete,” *Mater. J.*, vol. 98, no. 4, pp. 306–312, Jul. 2001, doi: 10.14359/10399.

[218] K.-S. Yeon, Y.-S. Choi, K.-K. Kim, and J. H. Yeon, “Flexural fatigue life analysis of unsaturated polyester-methyl methacrylate polymer concrete,” *Constr. Build. Mater.*, vol. 140, pp. 336–343, Jun. 2017, doi: 10.1016/j.conbuildmat.2017.02.116.

[219] S. Goel and S. P. Singh, “Fatigue performance of plain and steel fibre reinforced self compacting concrete using S–N relationship,” *Eng. Struct.*, vol. 74, pp. 65–73, Sep. 2014, doi: 10.1016/j.engstruct.2014.05.010.

[220] B. Zhang, D. V. Phillips, and K. Wu, “Further research on fatigue properties of plain concrete,” *Mag. Concr. Res.*, vol. 49, no. 180, pp. 241–252, Sep. 1997, doi: 10.1680/macr.1997.49.180.241.

[221] C. D. Johnston and R. W. Zemp, “Flexural Fatigue Performance of Steel Fiber Reinforced Concrete--Influence of Fiber Content, Aspect Ratio, and Type,” *Mater. J.*, vol. 88, no. 4, pp. 374–383, Jul. 1991, doi: 10.14359/1875.

[222] G. Batson, C. Ball, L. Bailey, E. Landers, and J. Hooks, “Flexural Fatigue Strength of Steel Fiber Reinforced Concrete Beams,” *J. Proc.*, vol. 69, no. 11, pp. 673–677, Nov. 1972, doi: 10.14359/11275.

[223] S. Arora and S. P. Singh, “Analysis of flexural fatigue failure of concrete made with 100% Coarse Recycled Concrete Aggregates,” *Constr. Build. Mater.*, vol. 102, pp. 782–791, Jan. 2016, doi: 10.1016/j.conbuildmat.2015.10.098.

[224] B. S. Saini and S. P. Singh, “Flexural fatigue strength prediction of self compacting concrete made with recycled concrete aggregates and blended cements,” *Constr. Build. Mater.*, vol. 264, p. 120233, Dec. 2020, doi: 10.1016/j.conbuildmat.2020.120233.

[225] M. Chemrouk, “The Deteriorations of Reinforced Concrete and the Option of High Performances Reinforced Concrete,” *Procedia Eng.*, vol. 125, pp. 713–724, Jan. 2015, doi: 10.1016/j.proeng.2015.11.112.

[226] S.-W. Kim and H.-D. Yun, “Crack-damage mitigation and flexural behavior of flexure-dominant reinforced concrete beams repaired with strain-hardening cement-based composite,” *Compos. Part B Eng.*, vol. 42, no. 4, pp. 645–656, Jun. 2011, doi: 10.1016/j.compositesb.2011.02.022.

[227] M. Hussein, M. Kunieda, and H. Nakamura, “Strength and ductility of RC beams strengthened with steel-reinforced strain hardening cementitious composites,” *Cem. Concr. Compos.*, vol. 34, no. 9, pp. 1061–1066, Oct. 2012, doi: 10.1016/j.cemconcomp.2012.06.004.

[228] C. Pellegrino, F. da Porto, and C. Modena, “Rehabilitation of reinforced concrete axially loaded elements with polymer-modified cementicious mortar,” *Constr. Build. Mater.*, vol. 23, no. 10, pp. 3129–3137, Oct. 2009, doi: 10.1016/j.conbuildmat.2009.06.025.

[229] R. H. Geraldo, O. G. Teixeira, S. R. C. Matos, F. G. S. Silva, J. P. Gonçalves, and G. Camarini, “Study of alkali-activated mortar used as conventional repair in reinforced concrete,” *Constr. Build. Mater.*, vol. 165, pp. 914–919, Mar. 2018, doi: 10.1016/j.conbuildmat.2018.01.063.

[230] L. Hou, J. Wang, T. Huang, C. Shen, F. Aslani, and D. Chen, “Flexural behaviour of corroded reinforced concrete beams repaired with ultra-high toughness cementitious composite,” *Constr. Build. Mater.*, vol. 211, pp. 1127–1137, Jun. 2019, doi: 10.1016/j.conbuildmat.2019.03.214.

[231] A. Ramachandra Murthy, B. L. Karihaloo, P. Vindhya Rani, and D. Shanmuga Priya, “Fatigue behaviour of damaged RC beams strengthened with ultra high performance fibre reinforced concrete,” *Int. J. Fatigue*, vol. 116, pp. 659–668, Nov. 2018, doi: 10.1016/j.ijfatigue.2018.06.046.

[232] F. Yu *et al.*, “Flexural experiment and capacity investigation of CFRP repaired RC beams under heavy pre-damaged level,” *Constr. Build. Mater.*, vol. 230, p. 117030, Jan. 2020, doi: 10.1016/j.conbuildmat.2019.117030.

[233] M. Hamrat *et al.*, “Experimental and numerical investigation on the deflection behavior of pre-cracked and repaired reinforced concrete beams with fiber-reinforced polymer,” *Constr. Build. Mater.*, vol. 249, p. 118745, Jul. 2020, doi: 10.1016/j.conbuildmat.2020.118745.

[234] N. K. Banjara and K. Ramanjaneyulu, “Investigations on behaviour of flexural deficient and CFRP strengthened reinforced concrete beams under static and fatigue loading,” *Constr. Build. Mater.*, vol. 201, pp. 746–762, Mar. 2019, doi: 10.1016/j.conbuildmat.2019.01.010.

[235] F. Moodi, A. Kashi, A. A. Ramezanianpour, and M. Pourebrahimi, “Investigation on mechanical and durability properties of polymer and latex-modified concretes,” *Constr. Build. Mater.*, vol. 191, pp. 145–154, Dec. 2018, doi: 10.1016/j.conbuildmat.2018.09.198.

[236] A. Sadrmomtazi and R. K. Khoshkbijari, “Determination and Prediction of Bonding Strength of Polymer Modified Concrete (PMC) as the Repair Overlay on the Conventional

Concrete Substrate," *KSCE J. Civ. Eng.*, vol. 23, no. 3, pp. 1141–1149, Mar. 2019, doi: 10.1007/s12205-019-0113-3.

[237] X. Guo, Y. Wang, P. Huang, and S. Shu, "Fatigue behavior of RC beams strengthened with FRP considering the influence of FRP-concrete interface," *Int. J. Fatigue*, vol. 143, p. 105977, Feb. 2021, doi: 10.1016/j.ijfatigue.2020.105977.

[238] N. K. Banjara and K. Ramanjaneyulu, "Investigations on behaviour of flexural deficient and CFRP strengthened reinforced concrete beams under static and fatigue loading," *Constr. Build. Mater.*, vol. 201, pp. 746–762, Mar. 2019, doi: 10.1016/j.conbuildmat.2019.01.010.

[239] X. Li, J. Wang, Y. Bao, and G. Chen, "Cyclic behavior of damaged reinforced concrete columns repaired with high-performance fiber-reinforced cementitious composite," *Eng. Struct.*, vol. 136, pp. 26–35, Apr. 2017, doi: 10.1016/j.engstruct.2017.01.015.

[240] W. Fan and P. Qiao, "Vibration-based Damage Identification Methods: A Review and Comparative Study," *Struct. Health Monit.*, vol. 10, no. 1, pp. 83–111, Jan. 2011, doi: 10.1177/1475921710365419.

[241] M. Shariq, J. Prasad, and A. Masood, "Studies in ultrasonic pulse velocity of concrete containing GGBFS," *Constr. Build. Mater.*, vol. 40, pp. 944–950, Mar. 2013, doi: 10.1016/j.conbuildmat.2012.11.070.

[242] R. Hou and Y. Xia, "Review on the new development of vibration-based damage identification for civil engineering structures: 2010–2019," *J. Sound Vib.*, vol. 491, p. 115741, Jan. 2021, doi: 10.1016/j.jsv.2020.115741.

[243] R. Capozucca, "A reflection on the application of vibration tests for the assessment of cracking in PRC/RC beams," *Eng. Struct.*, vol. 48, pp. 508–518, Mar. 2013, doi: 10.1016/j.engstruct.2012.09.022.

[244] R. Capozucca, "Vibration analysis of damaged RC beams strengthened with GFRP," *Compos. Struct.*, vol. 200, pp. 624–634, Sep. 2018, doi: 10.1016/j.compstruct.2018.05.112.

[245] B. Wang and R. Gupta, "Performance of Repaired Concrete under Cyclic Flexural Loading," *Materials*, vol. 14, no. 6, Art. no. 6, Jan. 2021, doi: 10.3390/ma14061363.

[246] ASTM International, "ASTM C31 / C31M-21a Standard Practice for Making and Curing Concrete Test Specimens in the Field," West Conshohocken, PA, 2021. [Online]. Available: http://www.astm.org/cgi-bin/resolver.cgi?C31C31M-21a

[247] Y. Jiao, Y. Zhang, W. Shan, Q. Han, Y. Zhao, and S. Liu, “Damage fracture characterization of reinforced concrete beam subjected to four-point bending with parametric analysis of static, dynamic, and acoustic properties,” *Struct. Health Monit.*, vol. 19, no. 4, pp. 1202–1218, Jul. 2020, doi: 10.1177/1475921719881756.

[248] Z. Li, H. Zhu, C. Du, D. Gao, J. Yuan, and C. Wen, “Experimental study on cracking behavior of steel fiber-reinforced concrete beams with BFRP bars under repeated loading,” *Compos. Struct.*, vol. 267, p. 113878, Jul. 2021, doi: 10.1016/j.compstruct.2021.113878.

[249] ASTM International, “C597-16 Standard Test Method for Pulse Velocity Through Concrete. Retrieved from,” ASTM International, 2016. Accessed: May 21, 2019. [Online]. Available: https://doi.org/10.1520/C0597-16

[250] R. Capozucca and E. Magagnini, “RC beam models damaged and strengthened with GFRP strips under bending loading and free vibration,” *Compos. Struct.*, vol. 253, p. 112730, Dec. 2020, doi: 10.1016/j.compstruct.2020.112730.

[251] G. Lacidogna, G. Piana, and A. Carpinteri, “Damage monitoring of three-point bending concrete specimens by acoustic emission and resonant frequency analysis,” *Eng. Fract. Mech.*, vol. 210, pp. 203–211, Apr. 2019, doi: 10.1016/j.engfracmech.2018.06.034.

[252] Y. Zhang, X. Li, Y. Zhu, and X. Shao, “Experimental study on flexural behavior of damaged reinforced concrete (RC) beam strengthened by toughness-improved ultra-high performance concrete (UHPC) layer,” *Compos. Part B Eng.*, vol. 186, p. 107834, Apr. 2020, doi: 10.1016/j.compositesb.2020.107834.

[253] “Canadian Standards Association (CSA), CSA A23.3-04: Design of Concrete Structures, Rexdale, Ontario; 2003.”

[254] A. Duan, Z. Li, W. Zhang, and W. Jin, “Flexural behaviour of reinforced concrete beams under freeze–thaw cycles and sustained load,” *Struct. Infrastruct. Eng.*, vol. 13, no. 10, pp. 1350–1358, Oct. 2017, doi: 10.1080/15732479.2016.1268172.

[255] F. Zhu, Z. Ma, and T. Zhao, “Influence of Freeze-Thaw Damage on the Steel Corrosion and Bond-Slip Behavior in the Reinforced Concrete,” *Adv. Mater. Sci. Eng.*, vol. 2016, p. e9710678, Aug. 2016, doi: 10.1155/2016/9710678.

[256] P. Pei, S. Zheng, Y. Zhang, and L. Dong, “Overview on the bonding of reinforced concrete under pristine, corrosive and freeze-thaw conditions,” *J. Adhes. Sci. Technol.*, vol. 33, no. 7, pp. 761–789, Apr. 2019, doi: 10.1080/01694243.2018.1559439.

[257] N. Li, G. Long, Q. Fu, X. Wang, K. Ma, and Y. Xie, “Effects of freeze and cyclic flexural load on mechanical evolution of filling layer self-compacting concrete,” *Constr. Build. Mater.*, vol. 200, pp. 198–208, Mar. 2019, doi: 10.1016/j.conbuildmat.2018.11.177.

[258] W. Li, W. Sun, and J. Jiang, “Damage of concrete experiencing flexural fatigue load and closed freeze/thaw cycles simultaneously,” *Constr. Build. Mater.*, vol. 25, no. 5, pp. 2604–2610, May 2011, doi: 10.1016/j.conbuildmat.2010.12.007.

[259] W. Li, Z. Jiang, Z. Yang, J. Jiang, W. Sun, and Z. Deng, “Interactive Effect of Mechanical Fatigue Load and the Fatigue Effect of Freeze-Thaw on Combined Damage of Concrete,” *J. Mater. Civ. Eng.*, vol. 27, no. 8, p. 04014230, Aug. 2015, doi: 10.1061/(ASCE)MT.1943-5533.0001176.

[260] Y. Qiao, W. Sun, J. Jiang, and D. Pan, “Coupling Mechanism of Saturated Concrete Subjected to Simultaneous Fatigue Loading and Freeze-thaw Cycles,” *J. Wuhan Univ. Technol.-Mater Sci Ed*, vol. 33, no. 5, pp. 1121–1128, Oct. 2018, doi: 10.1007/s11595-018-1944-3.

[261] Y. Yuan *et al.*, “Frost resistance of fiber-reinforced blended slag and Class F fly ash-based geopolymer concrete under the coupling effect of freeze-thaw cycling and axial compressive loading,” *Constr. Build. Mater.*, vol. 250, p. 118831, Jul. 2020, doi: 10.1016/j.conbuildmat.2020.118831.

[262] B. Lei, W. Li, Z. Tang, V. W. Y. Tam, and Z. Sun, “Durability of recycled aggregate concrete under coupling mechanical loading and freeze-thaw cycle in salt-solution,” *Constr. Build. Mater.*, vol. 163, pp. 840–849, Feb. 2018, doi: 10.1016/j.conbuildmat.2017.12.194.

[263] W.-L. Qiu, F. Teng, and S.-S. Pan, “Damage constitutive model of concrete under repeated load after seawater freeze-thaw cycles,” *Constr. Build. Mater.*, vol. 236, p. 117560, Mar. 2020, doi: 10.1016/j.conbuildmat.2019.117560.

[264] Z. Fan, H. Xu, J. Xiao, and Y. Tan, “Effects of freeze-thaw cycles on fatigue performance of asphalt mixture and development of fatigue-freeze-thaw (FFT) uniform equation,” *Constr. Build. Mater.*, vol. 242, p. 118043, May 2020, doi: 10.1016/j.conbuildmat.2020.118043.

[265] J. Ranz, S. Aparicio, H. Romero, M. J. Casati, M. Molero, and M. González, “Monitoring of Freeze-Thaw Cycles in Concrete Using Embedded Sensors and Ultrasonic Imaging,” *Sensors*, vol. 14, no. 2, Art. no. 2, Feb. 2014, doi: 10.3390/s140202280.

[266] S. Jin, G. Zheng, and J. Yu, “A micro freeze-thaw damage model of concrete with fractal dimension,” *Constr. Build. Mater.*, vol. 257, p. 119434, Oct. 2020, doi: 10.1016/j.conbuildmat.2020.119434.

[267] Y. Dong, C. Su, P. Qiao, and L. Sun, “Microstructural damage evolution and its effect on fracture behavior of concrete subjected to freeze-thaw cycles,” *Int. J. Damage Mech.*, vol. 27, no. 8, pp. 1272–1288, Aug. 2018, doi: 10.1177/1056789518787025.

[268] B. Li, J. Mao, W. Shen, H. Liu, X. Liu, and G. Xu, “Mesoscopic cracking model of cement-based materials subjected to freeze-thaw cycles,” *Constr. Build. Mater.*, vol. 211, pp. 1050–1064, Jun. 2019, doi: 10.1016/j.conbuildmat.2019.03.266.

[269] T. Ueda, M. Hasan, K. Nagai, Y. Sato, and Licheng Wang, “Mesoscale Simulation of Influence of Frost Damage on Mechanical Properties of Concrete,” *J. Mater. Civ. Eng.*, vol. 21, no. 6, pp. 244–252, Jun. 2009, doi: 10.1061/(ASCE)0899-1561(2009)21:6(244).

[270] Y. Fu, L. Cai, and W. Yonggen, “Freeze–thaw cycle test and damage mechanics models of alkali-activated slag concrete,” *Constr. Build. Mater.*, vol. 25, no. 7, pp. 3144–3148, Jul. 2011, doi: 10.1016/j.conbuildmat.2010.12.006.

[271] W. Dong, X. Shen, H. Xue, J. He, and Y. Liu, “Research on the freeze-thaw cyclic test and damage model of Aeolian sand lightweight aggregate concrete,” *Constr. Build. Mater.*, vol. 123, pp. 792–799, Oct. 2016, doi: 10.1016/j.conbuildmat.2016.07.052.

[272] B. Wang, J. Pan, R. Fang, and Q. Wang, “Damage model of concrete subjected to coupling chemical attacks and freeze-thaw cycles in saline soil area,” *Constr. Build. Mater.*, vol. 242, p. 118205, May 2020, doi: 10.1016/j.conbuildmat.2020.118205.

[273] J. Tian *et al.*, “Investigation of damage behaviors of ECC-to-concrete interface and damage prediction model under salt freeze-thaw cycles,” *Constr. Build. Mater.*, vol. 226, pp. 238–249, Nov. 2019, doi: 10.1016/j.conbuildmat.2019.07.237.

[274] Z. Wang, W. Qin, L. Li, Y. Yang, H. Lv, and L. Zhang, “Experimental research on variable-amplitude fatigue behavior of cracked mortar after epoxy grouting,” *Constr. Build. Mater.*, vol. 304, p. 124600, Oct. 2021, doi: 10.1016/j.conbuildmat.2021.124600.

[275] Z. OU and L. SUN, “Flexural fatigue-life reliability of frost-damaged concrete,” *J. Zhejiang Univ. Eng. Sci.*, vol. 51, no. 6, pp. 1074–1081, 2017.

[276] K. Kirane and Z. P. Bažant, “Size effect in Paris law and fatigue lifetimes for quasibrittle materials: Modified theory, experiments and micro-modeling,” *Int. J. Fatigue*, vol. 83, pp. 209–220, Feb. 2016, doi: 10.1016/j.ijfatigue.2015.10.015.

[277] Y. Wang and J. Li, “Experimental study on stochastic responses of reinforced concrete beams under fatigue loading,” *Int. J. Fatigue*, vol. 151, p. 106347, Oct. 2021, doi: 10.1016/j.ijfatigue.2021.106347.

Appendix A

Table A1. Polypropylene fiber properties.

Mechanical Property	Unit	Value
Length of the fiber	mm	12
Diameter of the fiber	micron	30
Specific Gravity	-	0.9
Elastic Modulus	GPa	7
Tensile Strength	MPa	300-450
Water Absorption	%	0
Melting Point	℃	162
Thermal Conductivity	W/mK	N/A
Density	kg/m3	900

Table A2. Chemical Composition of Mix M.

Chemical Component	Quantity
Crystalline Silica	15-25%
Portland cement	5-10%
Aluminum oxide	1-5%
Iron oxide	0-3%
Calcium oxide	0.3-3%

Table A3. Chemical Composition of Mix P.

Chemical Component	Quantity
Silica sand	25-50%
Portland cement	5-10%
Flue dust (zinc refining)	0.1-0.25%
Lithium carbonate	0.1-0.25%

Table A4. Physical Properties of Metakaolin.

Property	Description/Value
Visual Color	Cream White
Particle Structure Amorphous	5 to 6
325 Mesh Residue %	0.09
Average Particle Size (Sedigraph)	1.4 µ
Free Moisture %	Max 0.5
Specific Gravity	2.2
pH (20% Solids)	4.0

Table A5. Physical Properties of Silica Fume

Property	Description/Value
Appearance	Light Grey Powder
Specific Gravity	2.2
Bulk Density	600 -650 kg/m³
Fineness, (45 µm retained)	1-3 wt % retained
Soundness, (autoclave)	0.01 – 0.05 % Expansion
Tendency to entrap air	No
7-day Pozzolanic Strength Activity Index	120 – 127 % of control
BET Fineness (specific surface)	18 -21 m²/g

Table A6. Chemical composition of the adhesive.

Name	Percentage by weight (indicative)
Acetone	20-30
Propane	20-30
Cyclohexane	10-20
Petroleum distillates	10-20
Hexane	<0.5

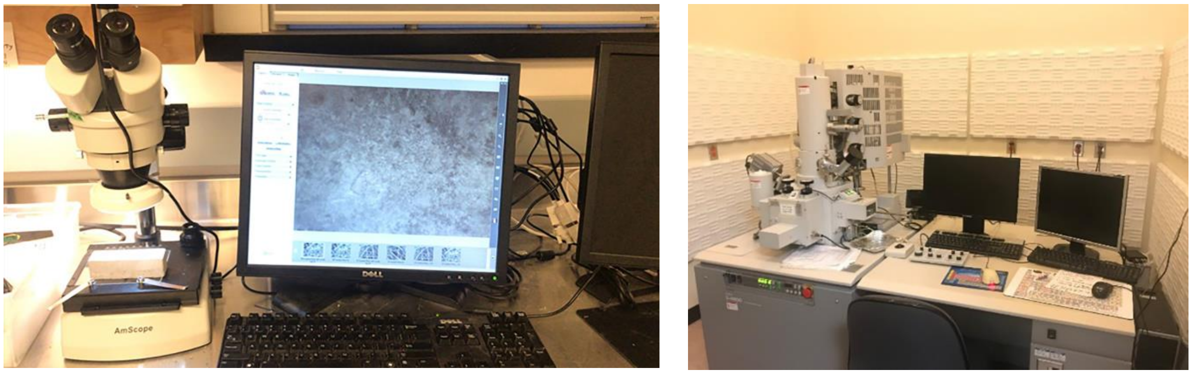

(a) (b)

Figure A1. a) Amscope © Trinocular stereo zoom microscope setup; b) Hitachi S-4800 FESEM.